Theoretical Study on Oxygen and Borohydride Reaction on Metal Surfaces

(金属表面上での酸素分子及びテトラヒドロホウ酸イオンの反応に関する理論的研究)

2012

MARY CLARE SISON ESCAÑO
メアリ クレア スイソン エスカニョ

Division of Precision Science & Technology and Applied Physics
Graduate School of Engineering
Osaka University
大阪大学大学院工学研究科
精密科学・応用物理学専攻

Theoretical Study on Oxygen and Borohydride Reaction on Metal Surfaces

(金属表面上での酸素分子及びテトラヒドロホウ酸イオンの反応に関する理論的研究)

2012

MARY CLARE SISON ESCAÑO
メアリ クレア スイソン エスカニョ

Division of Precision Science & Technology and Applied Physics
Graduate School of Engineering
Osaka University
大阪大学大学院工学研究科
精密科学・応用物理学専攻

Abstract

The reactivity of simple molecules on metal surfaces has been studied in the light of the need to contribute to the understanding of two major chemical reactions of outstanding practical importance: oxidation and dehydrogenation. Both the oxidation and dehydrogenation are key reactions in energy conversion systems such as fuel cell. For instance, the oxidation of metal surface is often an initial step in oxidation reduction reaction (ORR). Dehydrogenation of chemical hydrides, on the other hand, has increasingly attracted researchers in field of hydrogen generation or in its potential as anodic fuel. An atomistic modeling of the interaction of the simple molecules, such as oxygen and borohydride, with metals, focusing on the fundamental energetic, geometric and electronic properties, is conducted to advance current understanding of chemical reactivities. Mainly, density functional theory (DFT) calculations are conducted to study the:

(1) magnetic effects on oxygen (O_2) reaction on Pt; and
(2) changes in borohydride structures with respect to metal catalyst (Pt vs Os), H_2O co-adsorption, and electric field.

In relation to (1), the dissociative adsorption of oxygen on Pt crystalline surface is activated and that the dissociated oxygen atoms (O_{ad}) are strongly bound on the surface. Reduced binding energy of O_{ad} on surface has been attained on some Pt monolayer bimetallic structures (MBS), however, weakly bound oxygen atom on surface also indicates high dissociation barrier, which is often undesirable. Fundamentally, such change in the stability of O_{ad} on Pt arises from the shift in Pt-d band due to strain effects or hetero-metal bonding. This thesis integrates the theoretical works done, employing DFT calculations, to explore the changes in reaction energy profile of oxygen on Pt due to magnetic effects. Using Pt/M {where M = Fe(001) and Co(001)}, a magnetic moment is induced on Pt (now aptly called ferromagnetic Pt/M). The spin-down components of d-states are shifted towards the Fermi level (E_F). The oxygen reaction on the ferromagnetic Pt/M is compared with the reference system, Pt(100)-(1x1) (denoted as paramagnetic Pt or pure Pt). A decrease in both the oxygen dissociative adsorption barrier and the dissociated oxygen atoms binding energy, with respect to that of the reference surface is attained.

This phenomenon is termed as O_2 "activation". Interestingly, an emergence of non-activated dissociative adsorption on Pt/Fe is noted. We found that the O-O scission on Pt/M is promoted due to π^* -d_{zz} hybridization changing the occupation of the π^* - states of O_2 on Pt/M as compared with pure Pt. An easier dissociation of O_2 on Pt/Fe and Pt/Co as compared to Pt has been observed in half-cell experiments. Using a combination of DFT calculations and Monte-Carlo simulations, the transition temperature of the ferromagnetic Pt/M is found to be higher than room temperature, indicating that its reactivity can be retained at a wide temperature range.

On the other hand, for (2), a general consensus that hydrogen evolution is prevalent on Pt has been established and has been attributed to the high activity of the catalyst towards hydrolysis of borohydride. So far, there has been no idea on why such reaction occurs until an experiment suggests large surface coverage of hydrogen on the surface (H_{ad}) after a sequence of electrochemical-chemical steps: (1) $BH_4^- \rightarrow BH_{4ad} + e^-$ and (2) $BH_{4ad} \rightarrow BH_{ad} + 3H_{ad}$. We performed DFT calculations to verify and explain, in terms of Pt surface electronic property, the chemical step (2). We found that borohydride adsorption is dissociative on Pt. Such dissociative adsorption is observed on 5d transition metals, except on Os (molecular). The difference in the B-H bond breaking process on Os and Pt is drawn. We found that B-H breaking is activated on Os and non-activated on Pt. This difference arises from the nature of the d_{yz} and d_{zz} states at the E_F. The significant elongation B-H bond on Os implies vulnerability of the molecular structure towards B-H breaking upon interaction with external factors such as H_2O co-adsorption and electric field. We then determined the changes in the BH_{4ad} structures, in terms of changes in B-H bond lengths, upon H_2O_{ad} co-adsorption and applied electric field. We noted that BH_{4ad} structures change with H_2O_{ad} co-adsorption due to electrostatic interactions. In the presence of homogenous electric field, the binding energy of the BH_{4ad} shifts due to first and second order Stark effect. This (de)stabilization, in turn, minimally changes the B-H bond lengths. However, with H_2O_{ad} co-adsorption, the applied negative electric field can stabilize H_2O monomer while deviating the H from planar configuration, reducing the electrostatic interaction between the co-adsorbed species and the promotion of B-H breaking due to H_2O co-adsorption is significantly reduced.

List of Figures

List of Tables

Contents

Chapter 1
Introduction

The need to understand the interaction of simple molecules (oxygen and borohydride) with metal surfaces for certain industrial applications such as energy conversion motivates the conduct of fundamental studies on oxidation and dehydrogenation reactions on Pt, Pt-3d bimetallic systems and other pure 5d transition metals. Both the oxidation and dehydrogenation are key reactions in energy conversion systems such as fuel cell. For instance, the oxidation of metal surface is central to ORR in the cathode of polymer electrolyte fuel cell (PEFC). Dehydrogenation of chemical hydrides, on the other hand, has increasingly attracted researchers in field of hydrogen generation for PEFC or in the use of chemical hydride as an anodic fuel in the anode of alkaline fuel cell (e.g. direct borohydride fuel cell-DBFC). The background of this study is detailed below:

1.1 Oxidation reaction

The oxidation of metal surfaces is a phenomenon that plays a central role in heterogeneous catalysis. Key initial elementary steps in the O_2-metal interaction are dissociative adsorption and molecular adsorption. As an oxidation catalyst, platinum (Pt) is widely used in chemical, electrochemical and automotive industries, which leads to being one of the best studied systems in surface science. Thus far, the dissociative adsorption of O_2 on Pt crystalline surfaces is activated and the binding energy of the separated oxygen atoms (O_{ad}) is quite strong [1-6]. Reduction of the binding energy of O_{ad} proved to be useful, from technological point of view, especially in the case where the O_{ad} is an intermediate specie, where subsequent reactions with other surface species should proceed (such as protonation of O_{ad} into OH_{ad} in ORR). A weaker bound O_{ad} has been attained in various Pt monolayer bimetallic structures (MBS) [7-12]. The origin of destabilization of O_{ad} is attributed to (very briefly) the shift of Pt d-band towards lower energies. The basis of such line of thought is discussed further in Chapter 2. A lower d-band characteristic of metal surface usually indicates lower binding energy of adsorbates. It has been shown that the reduction in the dissociative adsorption energy of oxygen results in an

increase in oxygen dissociation barrier [13]. And so, the dissociation barrier is predicted to be higher in Pt-3d MBS than in pure Pt [7,8]. While the geometry and electronic properties of the adsorbed oxygen species (O_{2ad} and O_{ad}) on electronically modified Pt MBS have been extensively investigated, the influence of the magnetic state of the Pt surface on its reactivity has not been explored. There have been reports on the easier oxygen dissociation on Pt catalysts on Co and Fe substrates based on half-cell experiments [14,15]. Moreover, studies on magnetic structure of oxygen molecular assemblies and oxide phases on non-magnetic surfaces reveal interesting ferromagnetic or antiferromagnetic interactions depending on the coverage [16-18]. These recent experimental and theoretical investigations signify the need for a fundamental description of the adsorption properties of oxygen on a spin-polarized Pt. This thesis integrates the fundamental surface science studies based on density functional theory (DFT) calculations on the energetics of oxygen reaction on Pt taking into account the magnetic state of the metal surface (pure Pt → spin-polarized Pt). The ferromagnetic behavior of Pt on M is studied using a combination of DFT and sampling method (i.e. Monte Carlo). In open literature, this study has been the first attempt to bring the surface magnetism field in surface reaction or vice versa. Although spin-catalysis has been drawn as a concept from many years back, the change in the reactivity due to spin-polarization of Pt surface has not been taken into account. Spin-catalysis phenomena has only so far encompassed catalysts with 3d-transition metal center such as Fe-porphyrin and similar complexes [19,20].

1.2 Dehydrogenation reaction

The bond breaking involving hydrogen is an important step in dehydrogenation reactions. Recently, chemical hydrides have received research attention due to their high hydrogen content [21,22]. Borohydrides are one such group of compounds (i.e. ~10.6 wt% in $NaBH_4$ form) [22,23]. Significant number of research has been devoted to investigate their applicability for hydrogen generation. Also, because of its high theoretical energy density, the direct electricity generation from borohydride ion has been extensively investigated [23-25]. When used as a hydrogen source, borohydride undergoes hydrolysis reaction: (1) $BH_4^- + 4H_2O = B(OH)_4^- + 4H_2$, where the hydrogen is then supplied to a fuel cell. As an anodic fuel for DBFC, borohydride is oxidized

thru the following reaction: (2) $BH_4^- + 8OH^- = BO_2^- + 6H_2O + 8e^-$ (E°=-1.24V_{SHE}). In the latter method of power generation, the main issue is the co-occurrence of (1) and (2) reactions on the anode. Reaction (1) leads to atomic hydrogen on the anode resulting to a "mixed" potential of reactions (2) and (3) $H_2 + 2OH^- = 2H_2O + 2e^-$ (E°=-0.828V) or to H_2 evolution, which reduces the coulombic efficiency. Achieving borohydride oxidation at more negative potentials with no hydrogen evolution is an outstanding challenge since catalyst known for high activity for borohydride oxidation (e.g. Pt, Ni, Ir, Pd) are also highly active for hydrogen evolution. On the other hand, in the former method, the hydrogen generation through hydrolysis reaction (1) is an exothermic process and occurs even without a catalyst (pH < 9). To prevent H_2 formation upon standing, the borohydride solution is typically maintained as a strongly alkaline solution. Thus, H_2 is produced only when these solutions comes in contact with a catalyst. A number of noble and non-noble transition metals/alloys have been identified to be catalytically active towards hydrolysis reaction: Ru, Pt, Pt-Ru, Pt-Pd, Raney Ni and Co [26-31]. One of the main targets of this method of power generation employing borohydride is a rapid (but carefully controlled) H_2 generation at ambient temperatures (and even down to 0°C) without mechanical compression, addition of water, acidity or heat. In some reports, the H_2 yield can be manipulated using applied voltage [32,33]. Given the above scenarios, whether the borohydride act as energy carrier or as a storage medium, the hydrolysis reaction (1) on a catalyst under relevant electrode potentials is an integral process which should be well understood. The fundamental understanding of the reactions occurring on the catalyst surface itself is often inaccessible to electrochemical studies. It is known that central to the hydrolysis process is dehydrogenation of borohydride on metal catalyst. This stimulates the present investigation on the B-H bond breaking process as a result of borohydride interaction with the catalyst, water and applied voltage. There has been a general consensus that hydrogen evolution is observed on Pt, Ir and Pd [34-37] while the tendency of Os to catalyze hydrogen generation is speculated to be dependent on factors such as the solvent, catalyst structure, applied potential etc. [38]. It has also been considered that Os is a strong potential for a more controlled hydrolysis reactions, aside from the fact that it is five times cheaper than Pt [38]. These studies focus the present work on comparative study on the borohydride adsorption on Os and Pt to determine the intrinsic role of the electronic

property of the metal surfaces to B-H breaking process. Furthermore, the dependence the borohydride adsorption on factors such as water co-adsorption and external electric field is explored. These fundamental surface science studies conducted based on density functional theory calculations forms the second part of the thesis.

The thesis is presented in the following, in Chapter 2 and 3, the (1) oxidation reaction on Pt and Pt/M systems and (2) dehydrogenation of borohydride on 5d-transition metals (focusing on Pt and Os), respectively are discussed. Chapter 4 gives the conclusion and outlook. The theoretical background and some derivations of the DFT are discussed in the Appendix section. Here, the concepts and methods that are relevant to the systems and the computational modeling employed in this work are given. Reference to this section is made in the text whenever applicable.

Chapter 2
Oxidation of Ferromagnetic Pt/M

2.1 Ferromagnetic Pt/M

2.1.1 Computational method

We start by discussing the target system where the oxidation takes place. The ferromagnetic Pt/M is a monolayer of Pt on a magnetic substrate, M (where M=Fe, Co). This model is similar to the Pt MBS structures studied in relation to some catalytic reactions introduced previously in Chapter 1. Similar structures have also been synthesized and computationally modeled {e.g. Pt/Fe and Pt/Co MBS, multilayers and other layered structures (LS)} due to interesting two-dimensional ferromagnetic behavior, induced magnetic moments, magnetic anisotropies and potential for magnetic recording media [7-8, 39-44]. The general picture that arises from these studies is that Pt grows epitaxially and in layer-by-layer fashion on M. Also a ferromagnetic coupling between Pt and M with a significant induced magnetic moment on Pt is observed.

The atomic and electronic structures of Pt/M are obtained using first principles calculation based on DFT [45-47]. The theoretical background of this method and the implementation code are discussed in the Appendix. The M substrates are modeled by a five-layer bcc(001) slab in a (1x1) super cell. The Pt atoms are pseudomorphically laid (i.e. Pt atoms on four-fold hollow sites) on the M substrate, forming the Pt monolayer. Each slab is separated by ~12.0Å of vacuum. The pure Pt is modeled by a four-layer fcc Pt(100)-(1x1) slab, which exhibits the same surface structure as that of the ferromagnetic Pt/M surface. The following are the details of the calculation methods and parameters used for all systems (Pt/M and pure Pt). The electron-ion interaction is treated using Projector Augmented Wave (PAW) method [48,49]. As discussed in the Appendix, this is appropriate for systems such as Fe, Co. The Kohn-Sham (KS) equations are solved in a periodic system by expanding the wave function in plane wave basis set, with a 400eV energy cutoff. The exchange–correlation correction is based on generalized gradient approximation (GGA) using the Perdew, Burke and Ernzerhof (PBE) functional [50,51]. Brillouin-zone

integrations are performed on a grid of (4x4x1) Monkhorst-Pack k points with a smearing of Methfessel-Paxton method [52]. The optimized Pt/M surface is obtained by relaxing the Pt layer and that of the two top-most layers of the substrates. For the pure Pt, the two top-most layers are relaxed. The optimization is conducted using the conjugate-gradient method [53] and terminated until the Hellman-Feynman force on each atom is <0.01 eV/Å. The use of these parameters gives lattice parameters that are in good agreement with experiments as discussed below.

2.1.2 Atomic and electronic structures

The calculated equilibrium lattice constants for Pt, Fe and Co are 3.980Å, 2.834Å and 2.810 Å, respectively, which are in agreement with experiments {3.960, 2.860, 2.820}[54-56]. The 2^{nd}-3^{rd} column of Table 1 give the atomic structure data for the Pt/M and pure Pt slab. The corresponding schematic diagrams representing the atomic as well as the magnetic structure of the three systems, Pt, Pt/Co and Pt/Fe, are shown in Figure 1(a)-(c). In Table 1, we note that there is a small lattice mismatch between the Pt layer and the M substrate, hence, Pt is considered unstrained, consistent with experimental observations on layer-by-layer epitaxial growth of Pt on M as discussed above. The optimized Pt layer distance from the M substrate (d) is 1.62-1.63Å. For the pure Pt, the first interlayer distance, 1.93Å, gives a very minimal inward surface relaxation of ~3%, consistent with experiment (2%) [57] and other theoretical result (3%) [58]. We see that the Pt-M distance is contracted with respect to the pure Pt by ~0.30Å. This is consistent with the stronger Pt-M binding based on 1 Pt atom vacancy formation energy (E_{des}) in the order of ~0.29eV as shown in the 4^{th} column of Table 1.

Table 1: Pt and Pt/M (M:Fe,Co) geometry, binding energies and magnetic moments. E_{des} is the 1 Pt atom vacancy formation energy.

System	Lattice Mismatch {%}	Pt-M interlayer distance (d) {Å}	Pt-M binding (E_{des}) {eV}	d-band center (eV)	Pt magnetic moment {μ_B}
Pt	--	1.93	6.59	-1.80	0.00
Pt/Co	0.36	1.62	6.70	-2.20	0.43
Pt/Fe	0.49	1.63	6.77	-2.42	0.62

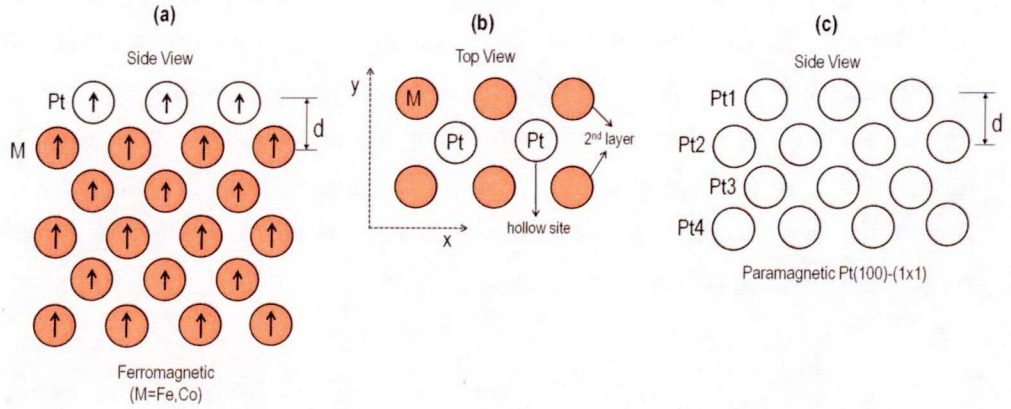

Figure 1: Schematic diagram of the Pt/M and pure Pt structures: (a) side view of Pt/M systems showing Pt monolayer and M (Fe and Co) substrates and (b) top view of Pt/M system showing the stable site of Pt atom and (c) side view of the reference system, unreconstructed Pt(001) viewed along [010] direction. White and shaded circles represent Pt and M atoms, respectively. Up arrows give the magnetic moment direction in Pt/M. Schematic diagrams show repeat of unit cell in x direction.

The Pt-M binding energy (E_{des}) is defined as one Pt atom vacancy formation energy, calculated using the following expression:

(2.1) $E_{des} = E_{Pt} + E_{slab*} - E_{slab}$

where E_{Pt} and E_{slab*} are the energies of the isolated Pt atom and slab with 1 Pt atom vacancy, respectively. Due this stronger Pt-M binding, a greater over-lap of d-states leads to lower d-band for the Pt layer as compared to the pure Pt, in the context of the rectangular band model [59,60]. Because of such strong hetero-metal interaction, the originally peaked d-states of the component systems broaden. And in the hybridized states, the d band-width is wider. A broad d-band should shift towards lower energies due to charge conservation. Below is a schematic diagram (Figure 2) illustrating this concept.

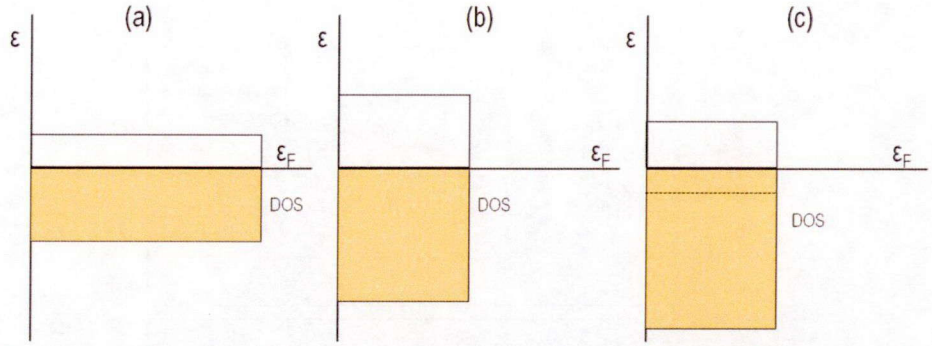

Figure 2: Diagram illustrating the rectangular band model as applied in hetero-metal interactions (bimetallic or alloys). Left-most panel (a) shows the narrow band; middle panel (b) shows the increase in d-band width and right-most panel (c) gives the shifted d-band towards lower energies to conserve the d-band filling {(a) vs (c)}.

Another interesting property of the Pt/M is its ferromagnetic property. As shown in Figure 1, a magnetic moment is induced on Pt layer in direction parallel to that of M. The values of the induced magnetic moments are: $0.62\mu_B$ and $0.43\mu_B$ on Fe and Co substrates, respectively. As discussed before, the induced magnetization of Pt has been experimentally observed in Pt/Fe MBS and in Pt/Co LS [41,44]. These are based on room temperature x-ray magnetic circular dichroism (XMCD) measurements. So we shall skip this for a while until we get to the finite temperature magnetic properties. The origin of magnetic property of an unfilled 5d-shell, which is nonmagnetic in pure metal, is usually understood in terms of strong mixing of 5d-states with M 3d-states, giving a spin-splitting of electronic states near the Fermi level (E_F). We also observed the same phenomenon for Pt/M as shown in Figure 3. Here, we show the DOS projected onto the Pt surface atom and M underlying atom for Pt/M. The LDOS of pure Pt is shown as dashed lines. We note that the spin-polarization of the Pt layer is due to the hybridization with Fe/Co-3d – states. The orbital-resolved LDOS for Pt and Pt/M are shown in Figure 4. We note that the spin-splitting changes the character of the d-orbitals. For instance, the spin-down d_{zz} state, which is filled in pure Pt {Figure 4(a)} is shifted towards the E_F in Pt/M {shown by the arrows in (b) and (c)}. The spin-up filled d_{xz} state in Pt/Fe is closer to E_F than in pure Pt. Unoccuppied d_{yz} state above the E_F disappears in Pt/Fe, while a spin down peak at E_F is noted for Pt/Co.

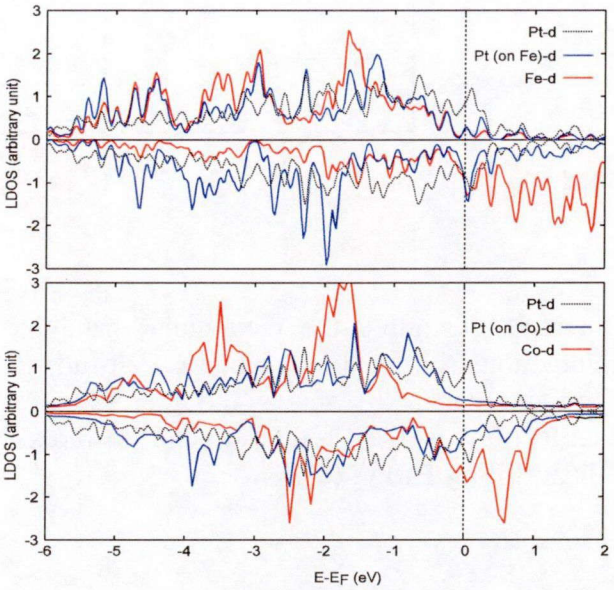

Figure 3. DOS projected on the surface Pt atoms on (top panel) Pt/Co and (bottom panel) Pt/Fe. The non-spin-polarized d-states of pure Pt is shown as dashed lines. Energy is given relative to E_F.

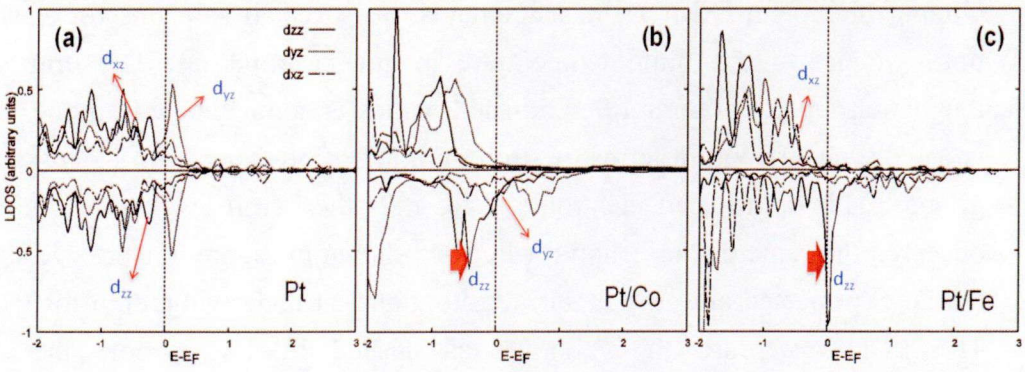

Figure 4: Orbital-resolved LDOS of (a) pure Pt, (b) Pt on Co and (c) Pt on Fe. The spin-polarization of d_{zz}, d_{yz} and d_{xz} states are shown. Energy is given relative to E_F.

A nice spin-down d_{zz} peak at E_F (Pt/Fe) and near E_F (Pt/Co) strongly originate from the Pt d_{zz} – M d_{xy} interactions as shown in Figure 5 and Figure 6. Such hybridization is made possible by the hollow site stable adsorption of Pt atom on M (recall Figure 1(b)).

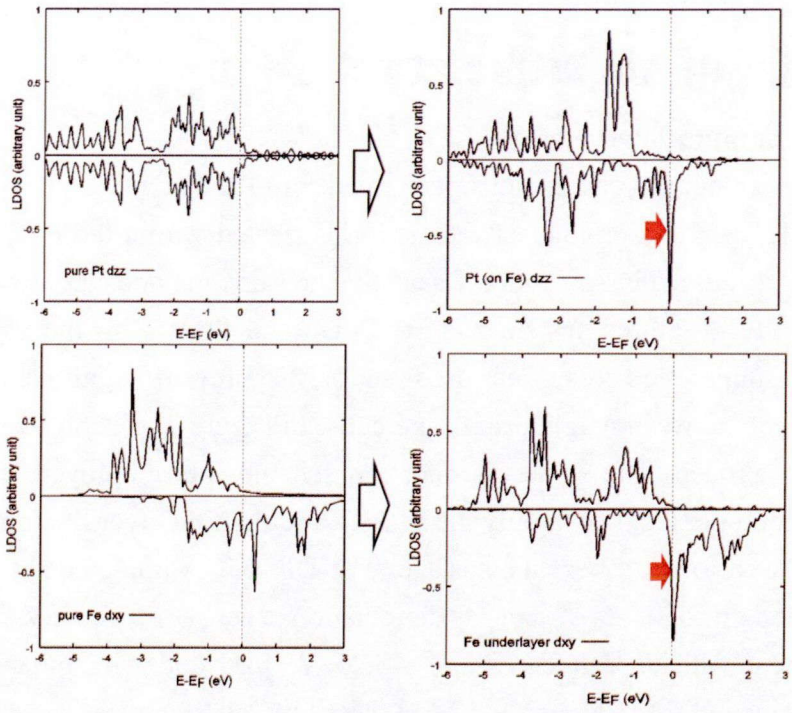

Figure 5: (Top-left) Pure Pt d_{zz}, (top-right) Pt on (Fe) after hybridization with (bottom-right) underlayer Fe-d_{xy}. Characteristic of pure Fe-d_{xy} is shown in bottom-left.

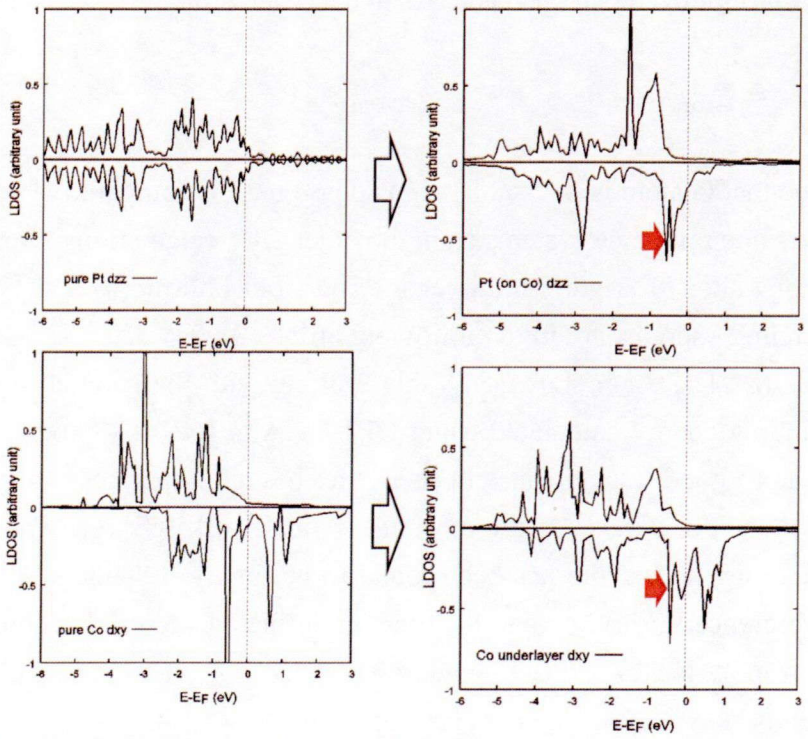

Figure 6: (Top-left) Pure Pt d_{zz}, (top-right) Pt on (Co) after hybridization with (bottom-right) underlayer Co-d_{xy}. Characteristic of pure Co-d_{xy} is shown in bottom-left.

2.2 O_2 dissociative adsorption

2.2.1 Computational method

The first principles calculations performed for O_2/Pt/M and O_2/Pt is also based on DFT. The electron-nuclear interaction is treated within the PAW method as well, as discussed in Appendix. Basically, the same methods are used for the O_2 reaction on the three systems: Pt/Fe, Pt/Co and Pt as with the bare slabs. A bigger supper cell (2x3) is used so as to prevent significant adsorbate interaction between neighboring supercells. In Figure 7, we show the pathways of O_2 approach. The same optimization schemes are employed, however, to lower computational cost, only the oxygen and the first layer Pt atomic position are allowed to relax near the surface. The DFT-GGA implementation yields a bond length of 1.24Å and a dissociation energy of 5.67eV, in general agreement with experiment (1.21Å; 5.25eV) [61] and with other DFT-GGA calculations (1.24Å; 5.64eV) [62,63]. The binding energy of oxygen atom on pure Pt in a 0.25ML coverage (coverage here is defined in terms of number of surface atoms). We used the same coverage as in Ref. 62 and compare the most stable site and binding energies. The binding energy is referenced to the total energy of optimized bare slab and isolated oxygen atom:

(2.2) $E_b = E_{total} - (E_{slab} + E_{isolated\ O\ atom})$

It is true that O atom is not stable in gas phase but for comparative purposes we use the same reference systems as in the other DFT calculations. We found that the bridge site (*b*) is preferred over the four-fold hollow (*h*) and top (*t*) sites. The binding energies are in the following order: -3.90eV (*b*) > -3.65eV (*h*) and -3.27eV (*t*). These are shown in Table 2 along with the geometric properties. The binding energy calculated using DFT-GGA in [62] is -3.80eV. Therefore, there is a good agreement between the binding energies of oxygen on Pt(100)-(1x1) and those of the other theoretical work [62]. Generally, for any coverage, the bridge site has been found to be the most stable site [62,64,65]. The preference for bridge over the more coordinated site has been explained in terms of more localized Pt-O bonding on bridge. The O atom on hollow site is prone to destabilization due to pair-wise repulsion.

Table 2: Chemisorption data for O on Pt(100)-(1x1) on three different high symmetry sites, bride (*b*), hollow (*h*) and top (*t*).

Data	bridge	hollow	top
E_b (eV)	-3.90	-3.65	-3.27
O-Pt vertical distance, z (Å)	1.29	1.15	1.83
O-Pt bond length (Å)	1.97	2.28	1.83

2.2.2 Energetics of O_2 dissociative adsorption

2.2.2.1 O_2 on Pt/Fe

The favorable pathways for O_2 reaction on Pt/M and Pt is discussed in this section.

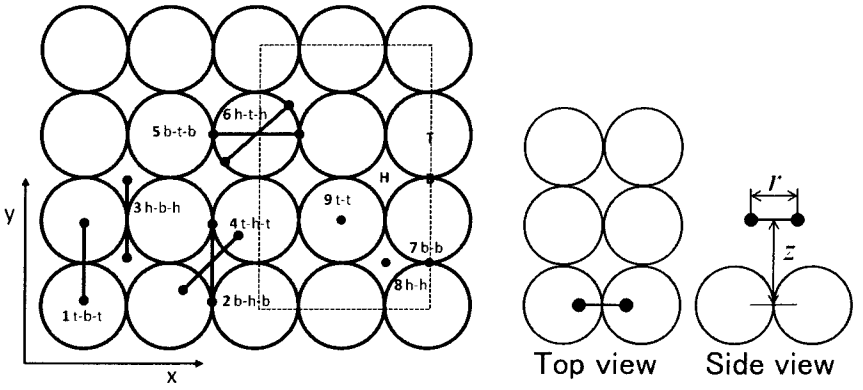

Figure 7: Configurations for O_2 dissociative adsorption (also called pathways) on Pt and Pt/M systems. Potential energy (PE) for the O_2 reaction on the surfaces is calculated at different increments in *r* and *z* as shown on the left. The supercell used is shown in dashed line.

The different configurations of O_2 are described in terms of the orientation of O-O axis and the position of the center of mass (c.m.) of the molecule (whether it is over bridge, hollow or top site). For instance, *t-b-t* refers to the configuration where the O_2 c.m. is over the bridge site and the O-O axis spans towards the top sites. Other pathways include O-O axis perpendicular to the surface (*b-b*, *h-h*, and *t-t* pathways). A total of 9 configurations are considered to sufficiently accommodate the degrees of freedom of the molecule. Each pathway is explored by calculating the total energy of O_2/Pt/M systems as a function of the height of the molecule from the surface (*z*) and the O-O bond

length (r). For comparison, the same is done with O_2/Pt. All energies are potential energies (PE) with respect to the separate slab and O_2:

(2.3) $E_b = E_{total} - (E_{slab} + E_{gas\ phase\ oxygen\ molecule})$

The r and z step-size are 0.1Å and 0.2Å, respectively. The r step size is chosen to be sufficiently small to ensure smooth variation of PE. We start with Pt/M (M=Fe). In Figure 8, we show the variation in potential energy along the reaction pathways described above. Perpendicularly oriented O_2 is very weakly bound and still resembles that of the gas phase O_2, indicative of a very low Pt surface reactivity with O_2 arriving vertical and so trajectories *7-9* were not included in the figure. Bond scission is found to be unfavorable in these configurations. Here, the analysis of PES focuses on O_2 arriving with O-O axis parallel to the surface. In all the configurations, the molecule enters at around z=3.60 Å from the surface with a 1.24Å bond length. This z distance is sufficiently far as verified by the zero PE at this point.

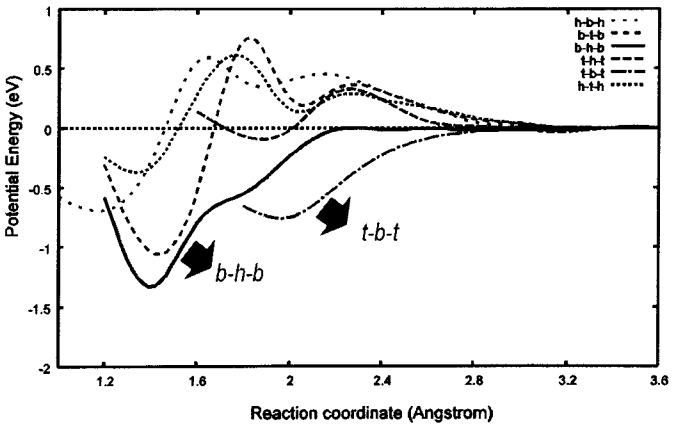

Figure 8: Variation of potential energy (PE) as O_2 approaches the Pt/Fe surface. The PE is determined with respect to separate O_2 and Pt/Fe slab. The potential energies per configuration are calculated as a function of the height of the molecule (z) and the O-O bond length (r).

Based on the PE curves, O_2 traverses both *t-b-t* and *b-h-b* paths without obvious barriers. The adsorption of oxygen in *t-b-t* is molecular and that on *b-h-b* is dissociative. Because of the shape of *b-h-b* PE curve (practically barrierless), it is likely that stable observables on the surface may not involve molecular O_2. Thus O_2 dissociates spontaneously on Pt/Fe along the *b-h-b*. The

direct *b-h-b* pathway is therefore a very favorable pathway and an important configuration to focus on for magnetic effects of surface in the reaction. We shall as well focus the discussions on this pathway for the rest of the other systems, Pt and Pt/Co (although other reaction pathways are also calculated for completeness sake and for comparison with experiments when available).

The atomic structure of dissociated O_2 at *b-h-b* on Pt/Fe is shown in Figure 9. The *r* and *z* distances at the final state (FS) are 2.80Å and 1.40Å, respectively. The binding energy of the separated atoms ($2O_{ad}$) is -1.33eV. These data are shown in Table 3. The geometry of the transition state (TS) will be discussed later when it is compared with the other two systems for the analysis of substrate effects (2.2.3).

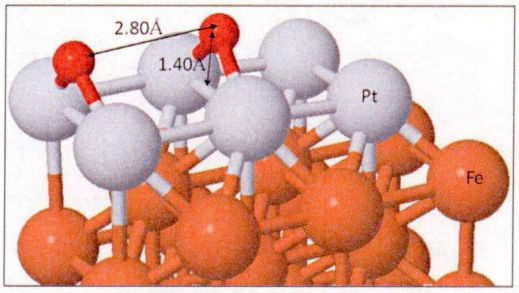

Figure 9: Geometry of dissociated oxygen following *b-h-b* configuration. The *r* and *z* distance are shown.

Table 3: Dissociative adsorption data of O_2 on Pt/Fe along the *b-h-b*.

Data	*b-h-b*
E_b (eV) at FS ($2O_{ad}$)	-1.33
E_b (eV) at TS	0.00
O-Pt vertical distance, z (Å) at FS	1.40
O-O bond length (Å) at FS	2.80

2.2.2.2 O_2 on Pt

The dissociative adsorption of O_2 on low-index pure Pt surfaces {(111) being extensively investigated} is activated whether in a direct or via molecular precursor pathways [1-6]. For Pt(111) and Pt(110), generally, O_2 follows the

latter. In Figure 10, we show the favorable pathways for O_2 dissociative adsorption on Pt(100)-(1x1), which is the reference system in this work. A small barrier exists in *b-h-b* pathway (0.16eV) while none is noted in *t-b-t*. In the same way, *b-h-b* and *t-b-t* are dissociative and molecularly adsorption pathways, respectively.

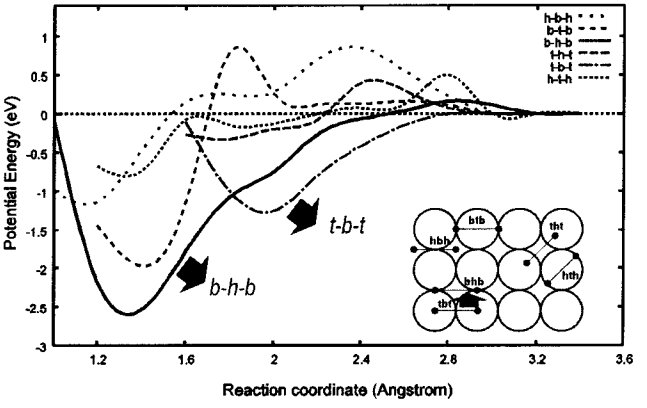

Figure 10: Variation of potential energy (PE) as O_2 approaches the pure Pt surface. The PE is determined with respect to separate O_2 and Pt slab. The potential energies per configuration are calculated as a function of the height of the molecule (z) and the O-O bond length (r).

The binding energies of $2O_{ad}$ in *b-h-b* is -2.54eV and of O_{2ad} in *t-b-t* is -1.29eV. The geometries are similar with that of Pt/Fe but the r is more stretched and z is contracted, indicating more stable adsorbates. The r and z distances are: 2.82Å, 1.28Å, respectively. For *t-b-t*, the r and z distances are 1.36Å and 1.84Å, respectively. Table 4 summarizes these data. We further note a crossing point between *t-b-t* and *b-h-b* which suggests a dissociation pathway from molecularly adsorbed O_2 (surface dissociation). Thus we check the activation barrier by PE scan over the O_2 translation across the surface (shown in the inset figure). In this path, the activation barrier is 0.20eV. O_2 on pure Pt may then most likely traverse the direct path. The activation barrier for direct *b-h-b* pathway is still lower than the surface dissociation pathway. Moreover, we note that due to the low barrier along *b-h-b*, Pt(100)-(1x1) seem to dissociate the molecule easier than on other facet, for instance Pt(111) [1,66]. We will not

tackle the reason for the differences between these crystalline facets, although this is also one of the interesting areas to explore theoretically.

Table 4: Dissociative adsorption data of O_2 on pure Pt along the *b-h-b* and *t-b-t* pathways.

Data	*b-h-b*	*t-b-t*
E_b (eV) at FS	-2.54	-1.29
E_b (eV) at TS	0.16	0.00
O-Pt layer distance, z (Å) at FS	1.28	1.84
O-O bond length (Å) at FS	2.82	1.36

These PE curves at *b-h-b* and *t-b-t* give the same general picture of O_2 dissociative adsorption as that revealed by the initial sticking probability profile, $s_0(E_i)$ of O_2 on Pt(100)-(1x1) at 300K as shown in Figure 11 [2]. The profile shows a steep fall of s_0 with increasing E_i, which indicates that a molecularly chemisorbed or physisorbed O_2 could be a precursor to dissociation. The subsequent rise of the s_0 with increasing E_i is due to opening up of another channel to adsorption, an activated direct dissociation channel.

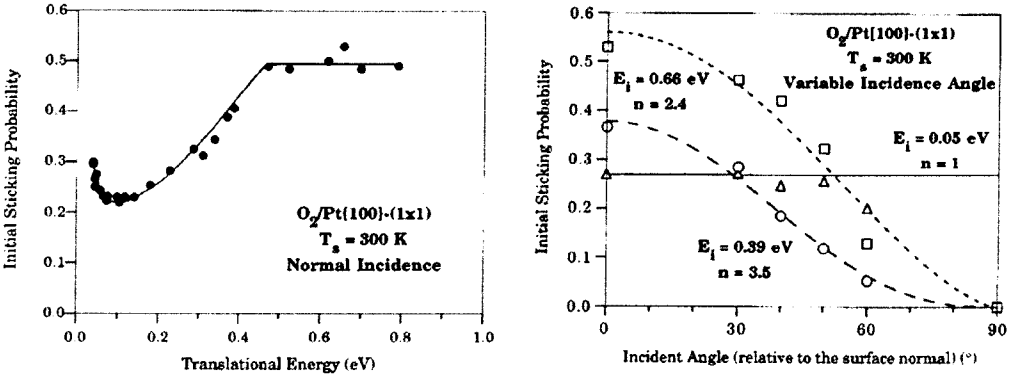

Figure 11: (Left) Initial sticking probability as a function of normal translational energy for normal incidence at a surface temperature of 300K. (Right) The angular variation of the initial sticking probability for beams of incident energy 0.05, 0.39, and 0.66 eV. [2]

This energetic and pathways are further confirmed by the dependence of s_0 on incident angle which reveals that at higher energies parallel momentum has a

strong inhibiting effect on the adsorption. This is believed to be due to variation of barrier heights across the unit cell with high barriers shadowing low barriers at large angle of incidence. By detailed balancing arguments based on Figure 11 (right panel), adsorption is activated in the high energy range (where direct dissociative adsorption channel is accessed) and non-activated in the low energy range (where the molecular precursor channel is accessed). And these are what the calculations in this work have also revealed (recall *b-h-b* and *t-b-t* in Figure 10). Such profiles are also typical for other crystalline surface such as Pt(111).

2.2.2.3 O_2 on Pt/Co

Similar PE curves are noted for Pt/Co (Figure 12), however, the *b-h-b* has lower barrier (0.11eV) as compared to Pt, but higher as compared to Pt/Fe. The separated atoms are bound to the surface at -1.44eV. This is much weaker than in Pt and just a little greater than in Pt/Fe. The dissociated atoms are 2.80Å apart. Table 5 summarizes these values. It appears that the trend that arises from the energetics of the reaction of O_2 along b-h-b pathway is that the Pt/Co lies in between the Pt and Pt/Fe. We will discuss the origin of this trend in the next section. For *t-b-t* pathway, r and z distances are 1.37Å, and 1.90Å, respectively. The binding energy is -0.93eV. We will compare this *t-b-t* site appropriately later with Pt in section 2.2.4.

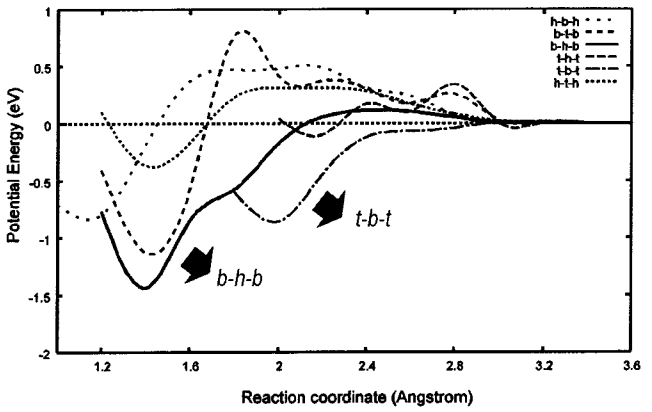

Figure 12: Variation of potential energy (PE) as O_2 approaches the Pt/Co. The PE is determined with respect to separate O_2 and Pt/Co slab. The potential energies per configuration are calculated as a function of the height of the molecule (z) and the O-O bond length (r).

Table 5: Dissociative adsorption data of O_2 on Pt/Co along the *b-h-b* and *t-b-t* pathways.

Data	*b-h-b*	*t-b-t*
E_b (eV) at FS	-1.44	-0.93
E_b (eV) at TS	0.11	0.00
O-Pt layer distance, z (Å) at FS	1.38	1.90
O-O bond length (Å) at FS	2.80	1.37

2.2.3 Analysis of the substrate effects

In determining the change in the O_2 reaction due to the substrate, we take into account O_2 dissociative adsorption via the direct path. As pointed out previously, this pathway is the *b-h-b*. In Figure 13, we show the PE curves for *b-h-b* configuration of the three systems.

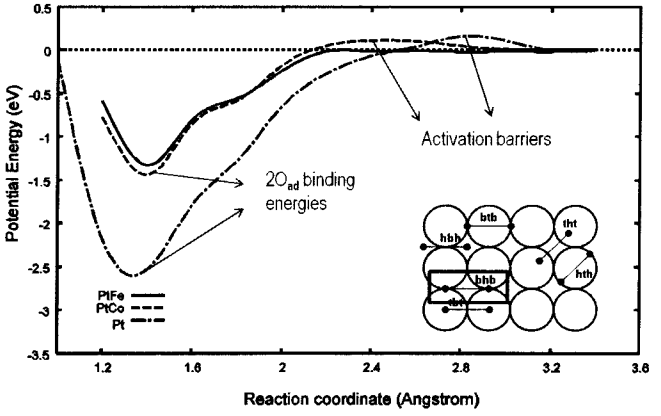

Figure 13. Variation of potential energy (PE) as O_2 approaches the Pt and Pt/M surfaces. The PE is determined with respect to separate O_2 and slab. The potential energies per configuration are calculated as a function of the height of the molecule (*z*) and the O-O bond length (*r*).

Two important regions in this PE plot direct us to some trends to analyze. The first is the potential minimum, identified as 2Oad binding energies (designated as FS before) and the other is the activation barrier or the binding energies at TS. The trend in the activation barriers for the systems is as follows: Pt (0.16eV) > Pt/Co (0.11eV) > Pt/Fe (0.00eV). And the binding energies of $2O_{ad}$

is: Pt (-2.54eV) > Pt/Co (-1.44eV) > Pt/Fe (-1.33eV). We first discuss the comparison between FSs. The strength of the binding of the dissociated O atoms on the surfaces can be correlated with the position of the d-band of Pt. The adsorption is much weaker in Pt/M owing to the lower d-band of Pt layer on M due to strong hetero-metal bonding and shorter Pt-M interlayer distance as discussed in 2.1.2. Generally, such lower d-band can lead to coupling with adsorbates 2p –states leading to repulsive interactions due to low anti-bonding state as a result of the splitting of hybridized states. For the TS, the activation barrier on Pt/M should be much higher than on Pt based on the differences in the $2O_{ad}$ binding energies (in the order of 1eV). However this is not the case. We have noted that barriers are a bit lower on Pt/M. The trends on the binding energies and the d-band center of the Pt on the three systems (pure Pt, Pt/Co and Pt/Fe) are plotted in Figure 14.

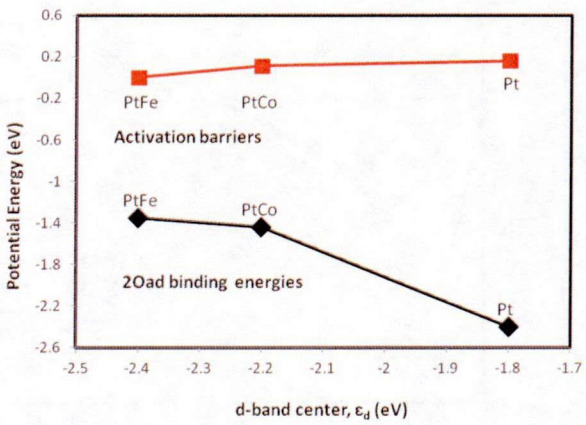

Figure 14: Trend of the $2O_{ad}$ binding energies with the d-band of Pt (black data series) and of the activation barriers with the d-band of Pt (red data series).

Previously, we have noted that despite the over-all downshift of the d-band, the spin-down component of certain d-orbitals, for instance, the d_{zz}, are significantly shifted towards the E_F due to spin-polarization of Pt layer in Pt/M. This d_{zz} is formerly filled in pure Pt (Figure 4). We can then check how such d_{zz} states of Pt/M hybridize with the O-2p states. In Figure 15, we show the orbital-resolved LDOS plots for O_2/Pt/M and O_2/Pt at TS.

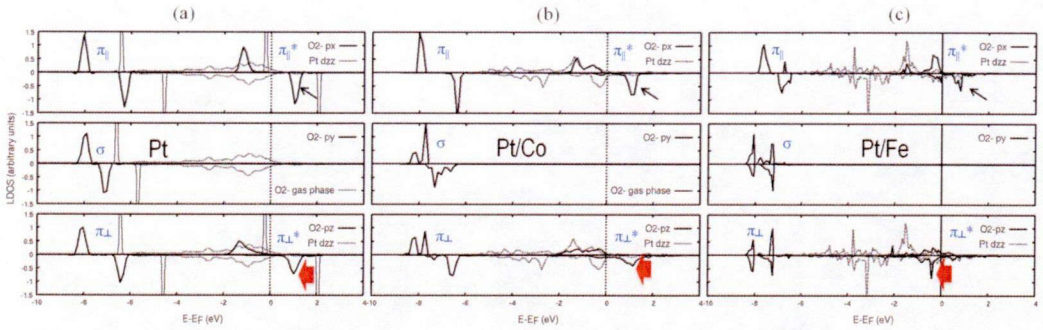

Figure 15: LDOS of (a) O_2/Pt (b) O_2/Pt/Co and (c) O_2/Pt/Fe . (b) and (c) show π*- Pt d-states hybridizations. The increased occupancy of spin-down $\pi^*_\perp$ in Pt/M systems is depicted by the bold arrows. Thin arrows show the change in the broadening of $\pi^*_\parallel$-states.

We note that the anti-bonding state of O_2 parallel to the surface ($\pi^*_\parallel$) is broadened and shifted towards lower energies for all systems {top panels of Figure 15(a)-(c)}. However, the broadening is more pronounced on Pt/M, especially in Pt/Fe {see the line arrow at Figure 15(c)}. For the perpendicular O_2-antibonding orbital, $\pi^*_\perp$, the interaction leads to occupancy of the spin-down component (bold red arrows). We note that the unoccupied spin-down $\pi^*_\perp$ of the gas phase O_2 remains unoccupied on pure Pt, partially filled in Pt/Co and completely filled on Pt/Fe. A better picture of this interaction is shown in Figure 16. The geometry at the TS is r=1.3Å and z=2.40Å (Pt/M) and z=2.80Å (Pt). It is well-known that the occupation of anti-bonding states correlates with the extent of O-O bond elongation. This occupation is destabilizing in O_2. Furthermore, the spatial orientation of d_{zz} (protruding perpendicularly out of the surface) poses an important feature over which the interaction (over-lap) with the molecule's p-states at high vertical distance from the surface can be enhanced.

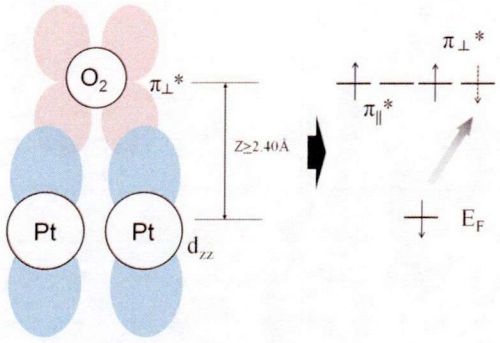

Figure 16: Schematic diagram of $\pi^*_\perp$-d_{zz} interaction in Pt/M systems. This interaction occurs at O_2 z (>2.40Å) distance from the surface and is responsible for the occupancy of the spin down $\pi^*_\perp$.

2.2.4 Molecular O_2 on Pt/Co and Pt

The purpose of this section is to compare the molecular O_2 configuration on Pt/Co and Pt (cases where O_2 dissociation barrier exists). The general picture of the O_2 adsorption in *t-b-t* is that the oxygen is more bound to the pure Pt surface (in the order of 0.33eV) than in Pt/Co. This trend is the same as that observed on *b-h-b*. Same argument on the entire low-d band of Pt/Co can be applied. The atomic structure is shown in Figure 17. Next, the O-O bond is elongated from 1.24Å (gas phase) to 1.36Å on pure Pt and to 1.37 Å on Pt/Co. Figure 18 shows the hybridization of the d-states with the O_2-antibonding states ($\pi^*_\parallel$ and $\pi^*_\perp$). The broadening of $\pi^*_\perp$-states are more pronounced on Pt than that of Pt/Co. The adsorption involves significant interaction with other d-orbitals such as d_{xz}. For $\pi^*_\parallel$, we can see interesting features (bold arrows). In Pt/Co, spin-down $\pi^*_\parallel$ is partially filled and exhibits good hybridization with d_{zz} (see the arrow at the bottom panel) and on d_{xz}. In pure Pt, $\pi^*_\parallel$ hybridize with d_{xz} very well though an unoccupied peak is recognizable. Hence, the effect of the d_{zz} state on Pt/Co interaction with O_2 is still evident but do not govern the final state adsorption energetics as other d-states come into play.

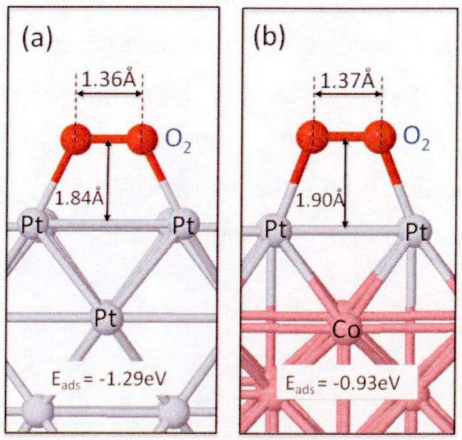

Figure 17: O_2 at *t-b-t* on (a) Pt and (b) Pt/Co. The geometry and the binding energies are given.

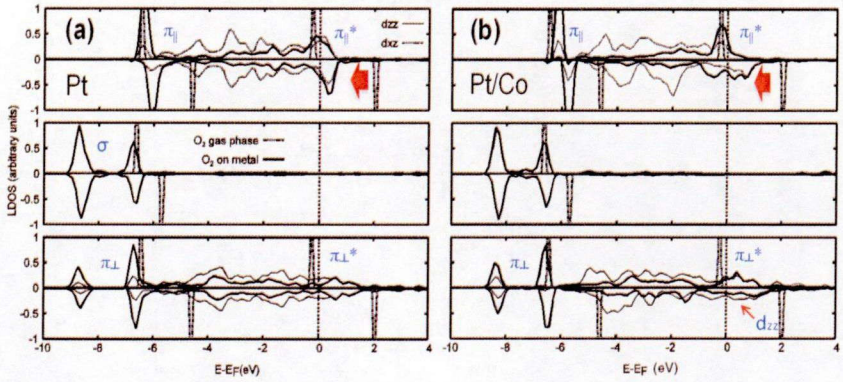

Figure 18: LDOS of O_2 on (a) Pt, (b) Pt/Co ,showing the bonding (π) and anti-bonding (π^*) states. Hybridization with Pt d_{zz} and d_{xz} states is also shown.

2.2.5 Has easier O_2 dissociation on Pt/M been observed?

So far, there have been no UHV experiments to confirm the findings above. However, an easier dissociation on Pt_{skin}/Fe and Pt_{skin}/Co have been observed by Watanabe group based on half-cell experiments [14]. Such favorable reaction produces large coverage of O_{ad} on the catalyst surface based on their X-ray photoemission spectroscopy (XPS) (Figure 19). Furthermore, it was found that there is a positive core-level shift of Pt 4f in the systems indicating upshift of Fermi level (or d-band shift to lower energies). Hence, an

explanation of the facile (or easier) dissociation was sought by this group. The computational modeling done above is far from describing a solid/liquid interface, hence the over-all reaction occurring in these systems can not be captured. But if we take into account the interaction between the metal surfaces and the molecule in question, then the above findings can corroborate qualitatively, specifically on the order of the reactivity (i.e. energy cost to dissociatively adsorbed O_2): Pt < Pt/Co < Pt/Fe.

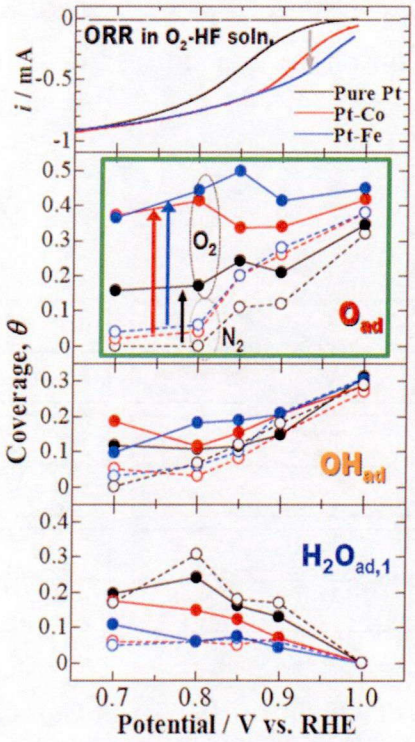

Figure 19: Negative linear sweep voltamograms on Pt, Pt/Co and Pt/Fe electrodes and coverages of O_{ad}, OH_{ad} and (d) H_2O_{ad} on the electrodes. [14]

2.3 Transition temperature of Pt/M

Because of the role of the magnetic state of Pt/M in changing the dissociative adsorption properties of oxygen, the study on the finite-temperature magnetic properties of the surface is imperative. This allows one, for instance, to determine temperature range where the adsorption properties are

distinguishable between the pure and the polarized Pt. These also imply a possible (and accessible) control of the surface reactivity via the temperature. In this section, we discuss the transition temperature of Pt on M. Here, we determine the spin orientational fluctuation of the two systems, Pt/Co and Pt/Fe (composed of a Pt layer and 6-layers of M) as a function of temperature using a combination of constrained DFT and sampling method {Monte Carlo (MC) simulation}. The effective Pt-M and M-M inter-atomic exchange parameters are obtained by fitting the first-principles total energy of the chosen non-collinear magnetic configurations obtained by DFT calculations to the effective Heisenberg model:

$$(2.4) \quad \mathcal{H}_{eff} = -\sum_{\mu\nu} J_{\mu\nu}\, \hat{\boldsymbol{e}}_{\mu} \cdot \hat{\boldsymbol{e}}_{\nu},$$

where the $\hat{\mathbf{e}}_{\mu}$ ($\hat{\mathbf{e}}_{\nu}$) gives the direction of the local moments on the μ^{th} (ν^{th}) atomic site and the $J_{\mu\nu}$ is the exchange parameter between the μ^{th} and ν^{th} nearest neighboring sites. These exchange parameters are then used in MC simulation to determine finite-temperature magnetic properties such as (1) room temperature magnetic moment and (2) transition temperature.

2.3.1 Constrained DFT

First, we begin with a brief introduction to constrained DFT which forms the basis of the estimation of the exchange parameters using non-collinear magnetic structures [67]. As discussed in Appendix, von Barth and Hedin extended the Kohn-Sham theory to spin polarized systems [68], by replacing the scalar density by a hermitian 2x2 matrix, $\underline{\rho}(\mathbf{r})$ (we simply use $\underline{\rho}(\mathbf{r})$ instead of $\rho_{\alpha\beta}(\boldsymbol{r})$ and $\mathbf{m}$ instead of $\boldsymbol{\zeta}$ in equation (47) for simplicity and to directly relate it to magnetization). We can then rewrite the equation (47) as:

$$(2.5) \quad \underline{\rho}(\boldsymbol{r}) = \frac{1}{2}(\rho(\mathbf{r})\underline{\mathrm{I}} + \underline{\boldsymbol{\sigma}} \cdot \underline{\mathbf{m}}(\mathbf{r}))$$

Using the Pauli spin matrices, $\underline{\boldsymbol{\sigma}}$ the density matrix can be decomposed in a scalar and vectorial part, corresponding to charge and magnetization density. Equation (2.5) further becomes:

$$(2.6)\quad \rho(\boldsymbol{r}) = \frac{1}{2}\begin{pmatrix} \rho(\boldsymbol{r}) + m_z(\boldsymbol{r}) & m_x(\boldsymbol{r}) - im_y(\boldsymbol{r}) \\ m_x(\boldsymbol{r}) + im_y(\boldsymbol{r}) & \rho(\boldsymbol{r}) - m_z(\boldsymbol{r}) \end{pmatrix}$$

Likewise, the potential matrices can be written in terms of a scalar potential and magnetic field $\boldsymbol{B}(\boldsymbol{r})$:

$$(2.7)\quad \underline{v}(\boldsymbol{r}) = v(\boldsymbol{r})\underline{I} + \mu_B \underline{\boldsymbol{\sigma}} \cdot \boldsymbol{B}(\boldsymbol{r}) \text{ and}$$

$$(2.8)\quad \underline{v}_{xc}(\boldsymbol{r}) = v_{xc}(\boldsymbol{r})\underline{I} + \mu_B \underline{\boldsymbol{\sigma}} \cdot \boldsymbol{B}_{xc}(\boldsymbol{r})$$

where $\mu_B = e\hbar/2mc$ is the Bohr magneton. Therefore, within this formalism, general non-collinear structures can be described in the DFT framework. When (2.7) and (2.8) is integrated in the KS equation:

$$(2.9)\quad \left[\left(-\frac{\hbar^2}{2m}\nabla^2 + \sum_\alpha \int \frac{\rho_{\alpha\alpha}(r')}{|r-r'|} dr'\right)\underline{I} + \underline{v}(r) + \frac{\delta E_{XC}}{\delta \underline{\rho}(r)}\right]\begin{pmatrix} \phi_i^+(\boldsymbol{r}) \\ \phi_i^-(\boldsymbol{r}) \end{pmatrix} = \varepsilon_i \begin{pmatrix} \phi_i^+(\boldsymbol{r}) \\ \phi_i^-(\boldsymbol{r}) \end{pmatrix}$$

For the collinear case, the potential matrices in (3.7 and 3.8) are diagonal (i.e. magnetic and exchange fields point in z direction), then 3.9 decouples into:

$$(2.10)\quad \left(-\frac{\hbar^2}{2m}\nabla^2 + v_{Coul}(\boldsymbol{r}) + \underline{v}(\boldsymbol{r}) + B_z(\boldsymbol{r}) + v_{xc}^+(\boldsymbol{r})\right)\phi_i^+(\boldsymbol{r}) = \varepsilon_i \phi_i^+(\boldsymbol{r})$$

$$\left(-\frac{\hbar^2}{2m}\nabla^2 + v_{Coul}(\boldsymbol{r}) + \underline{v}(\boldsymbol{r}) - B_z(\boldsymbol{r}) + v_{xc}^-(\boldsymbol{r})\right)\phi_i^-(\boldsymbol{r}) = \varepsilon_i \phi_i^-(\boldsymbol{r})$$

where $v_{Coul}(\boldsymbol{r})$ is now the classical Coulomb potential and $v_{xc}^+(\boldsymbol{r})$ the exchange-correlation potential that arises from the functional derivative of the exchange-correlation energy with respect to spin-up (+) and spin-down(-) part of the diagonal matrix. Systems that can be described by the decoupled equations are all kinds of magnetic materials that assume a collinear magnetic order (ferromagnetic, antiferromagnetic and ferromagnetic states). Like the density is a property that can – at least in principle – be obtained exactly in DFT, the spin density is a property that is well-defined in spin-polarized DFT:

(2.11) $\boldsymbol{m}(\boldsymbol{r}) = -\mu_B \sum_{\alpha\beta} \psi^+_{\alpha\beta}(\boldsymbol{r})\boldsymbol{\sigma}_{\alpha\beta}\psi_\beta(\boldsymbol{r})$

Hence, the spin moment, M as described before is the integral of the magnetization density:

(2.12) $M_{spin} = \int \boldsymbol{m}(\boldsymbol{r})d\boldsymbol{r} = \int(\rho^+(\boldsymbol{r}) - \rho^-(\boldsymbol{r}))d\boldsymbol{r}$

To determine the magnetic groundstate, one can determine the magnetic interactions between the atoms by a DFT calculation which are then mapped onto a model (the simplest case is the classical Heisenberg model) or like in molecular dynamics, spin dynamics explores magnetic degrees of freedom to determine the ground state configuration. What is important in this method is the discretization concept of the (vector) magnetization density {vector-spin DFT}. In spin dynamics, the evolution of discrete spins {vectors attached to certain (atomic) positions} are monitored. Therefore, we can define 3.11 within some sphere centered at the nucleus , the magnetization density:

(2.13) $\boldsymbol{m}(\boldsymbol{r}) = M_\nu \hat{\boldsymbol{e}}_\nu$

where M_ν is the magnetization and $\hat{\boldsymbol{e}}_\nu$ is the direction. The total energy of a magnetic system as a function of its magnetic structure can be described as a functional $E[\{\hat{\boldsymbol{e}}_\nu\}]$. So in the collinear states, $\hat{\boldsymbol{e}}_\nu$ is identical for all atoms, hence, these states are special solutions where $E[\{\hat{\boldsymbol{e}}_\nu\}]$ has a local or global maximum or minimum. In analogy to molecular dynamics, i.e. the problem of minimizing the energy as a function of atomic positions, the spin dynamics is introduced, where the magnetic orientations, $\hat{\boldsymbol{e}}_\nu$, take the role of the variables. An equation of motion is developed based on Antropov et. al. [69,70] and the time-dependent equation analogous to (2.10) – where $\underline{\upsilon}$(r)is diagonal, is:

(2.14) $i\frac{d\Phi}{dt} = [H_d - \underline{\boldsymbol{\sigma}} \cdot \boldsymbol{B}(r,t)\Phi]$ where $\Phi = \begin{pmatrix}\phi^+\\ \phi^-\end{pmatrix}$

Where H_d is the Hamiltonian that contains now only the diagonal parts. The evolution can now be separated into fast (value of magnetization) and slow (direction of magnetization) degrees of freedom. At a given time t, the time-independent version of (3.14) can be solved for a given magnetization

characterized by $\{\hat{\boldsymbol{e}}_\nu\}$. The evolution of magnetization density can be described by:

$$(2.15)\quad \frac{dm(r,t)}{dt} = 2\boldsymbol{m}\, x\, \boldsymbol{B} + \frac{i}{2}\nabla(\Phi^*\boldsymbol{\sigma}\cdot\nabla\Phi - c.c.)$$

Which can be derived by multiplying (2.14) with $\Phi^*\underline{\boldsymbol{\sigma}}$ and adding the complex conjugate equation, then comparing to (3.11) and using the relation: $\underline{\boldsymbol{\sigma}}(\underline{\boldsymbol{\sigma}}\cdot\mathbf{B}) = \mathbf{B} - \mathrm{i}\boldsymbol{\sigma}\,\mathrm{x}\,\mathbf{B}$. The second term described the longitudinal changes of the magnetization, which we think can be neglected if we are only concerned with the direction of the magnetization. So omitting this term, (3.15) describes the precession of the magnetization direction at an atom under the influence of magnetic field generated by the atom itself and other atoms of the crystal. We can then simplify (3.15) by the following:

$$(2.16)\quad \frac{d\hat{\boldsymbol{e}}_\nu}{dt} = -\frac{2}{\mu_B}\hat{\boldsymbol{e}}_\nu\, x\, \boldsymbol{I}_\nu \quad \text{where } \boldsymbol{I}_\nu = \mu_B\boldsymbol{B}$$

But how is the **B** determined given a magnetization direction? The constrained DFT developed by Dederichs et. al. [67] provides the necessary generalization to deal with arbitrary magnetic configurations (configurations where the orientations of the local moments are constrained to non-equilibrium directions). Here, a generalized energy functional, $E[\underline{\rho}(\boldsymbol{r}),\{\hat{\boldsymbol{e}}_\nu\}]$ is defined where the average magnetization in an atom $\langle\boldsymbol{m}\rangle_\nu$ points in the direction, $\hat{\boldsymbol{e}}_\nu$. This condition $\hat{\boldsymbol{e}}_\nu\,\mathrm{x}\,\langle\boldsymbol{m}\rangle_\nu = 0$, is introduced by a Langrange multiplier, $\boldsymbol{\lambda}$, so that the energy is:

$$(2.17)\quad E\left[\underline{\rho}(\boldsymbol{r}),\{\hat{\boldsymbol{e}}_\nu\}\right] = E\left[\underline{\rho}(\boldsymbol{r})\right] + \textstyle\sum_\nu \boldsymbol{\lambda}^\nu\cdot(\hat{\boldsymbol{e}}_\nu\,\mathrm{x}\,\langle\boldsymbol{m}\rangle_\nu)$$

$$= E\left[\underline{\rho}(\boldsymbol{r})\right] + \mu_B\textstyle\sum_\nu \boldsymbol{B}_c^\nu\cdot\langle\boldsymbol{m}\rangle_\nu$$

Therefore, the Lagrange multiplier is recast in a form of magnetic field, $\boldsymbol{B}_c^\nu$, which is now the constraining field in the atom ν that keeps the local (integrated) magnetic moment (the magnetization density integrated over a sphere cutoff):

(2.18) $\langle \boldsymbol{m}(\boldsymbol{r}) \rangle_v = \boldsymbol{M^v} = \int_{MT^v} \boldsymbol{m}(\boldsymbol{r}) d^3\boldsymbol{r}$

According to Hellman-Feynman theorem, the change in energy due to change in magnetization direction $d\hat{\boldsymbol{e}}_v$ is given by

(2.19) $dE = -\mu_B M^v \cdot (B_c^v \, x \, d\hat{\boldsymbol{e}}_v)$

Therefore, the constrained field can be interpreted as a torque acting on a magnetic moment in the spirit of spin dynamics described above. What is more interesting is that if the ab-initio total energies can be mapped on a model Hamiltonian, like the Heisenberg model (2.4), the exchange interaction of the system can be deduced and information on both the ground state as well as the excited states can be determined.

2.3.2 Estimated exchange parameters

We used two atomic layers to extract the Pt-M and M-M exchange parameters as shown in Figure 20(a)-(b). The use of two layers can capture the Pt-M and M-M exchange interaction needed for the MC simulation at the same time the computational cost can be lowered. The set of non-collinear magnetic structures are derived by rotation of the first layer atomic moments with respect to the global axis (z) {dashed line in Figure 20(a)-(b)} and by constraining the direction of the local magnetic moments in this non-equilibrium direction via a constraining field (constrained density functional theory) described above. The shaded area represents the unit cell used in the total energy calculation (the large vacuum, ~12.0Å, is not shown).

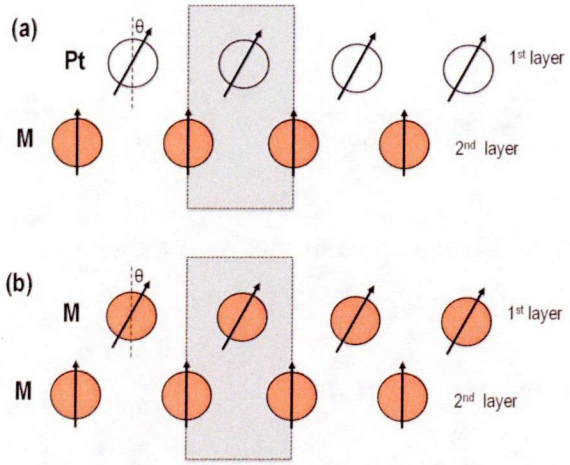

Figure 20: Rotation of the local moments of (a) Pt with respect M in ferromagnetic state (FM) and (b) M with respect to M in FM state. The shaded area represents the unit cell used in the total energy calculation. A vacuum of more than 12.0Å is used (not shown in the schematic diagram).

We see that by rotating the local moment of one atom in a two-atom bcc unit cell of a bilayer, the relative orientation with respect to four nearest neighbors is changed. The energy difference (ΔE) between these new non-collinear magnetic states with the ferromagnetic state is plotted against the angle of rotation (θ) {Figure 21(a)-(b) for Pt/Fe and Figure 22(a)-(b) for Pt/Co}.

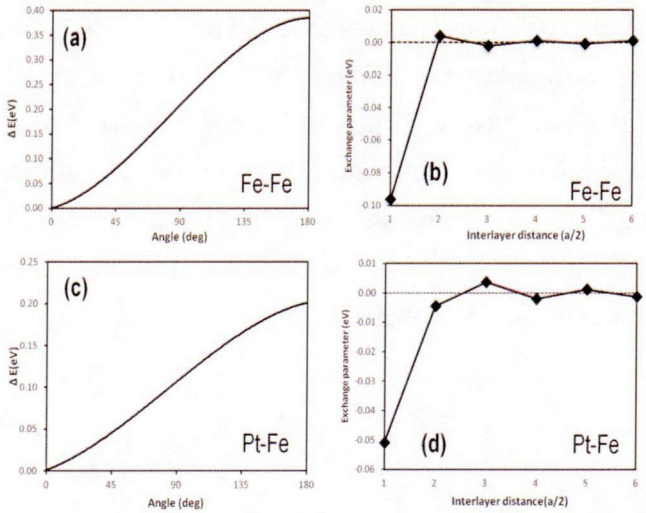

Figure 21: ΔE cosine-type dependence on the rotation angle (θ) for (a) Fe-Fe and (b) Pt-Fe. The oscillatory behavior of the inter-atomic exchange parameter: (c) Fe-Fe and (d) Pt-Fe, as a function of interlayer distance ($a/2$), where a is the lattice parameter of Fe.

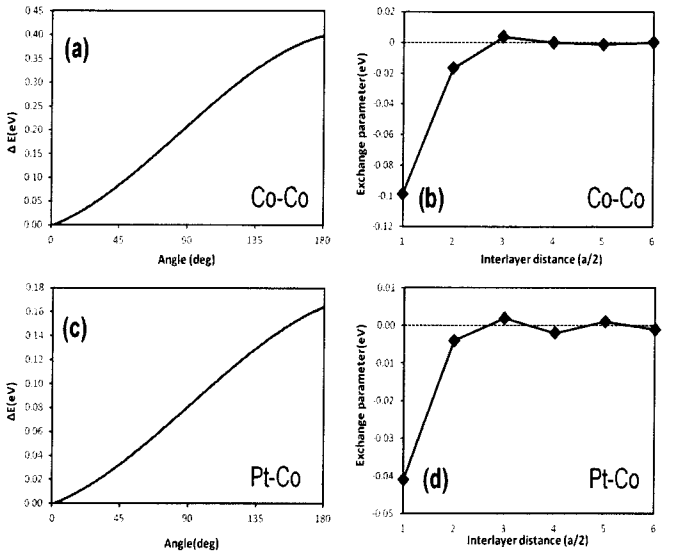

Figure 22: ΔE cosine-type dependence on the rotation angle (θ) for (a) Co-Co and (b) Pt-Co. The oscillatory behavior of the inter-atomic exchange parameter: (c) Co-Co and (d) Pt-Co, as a function of interlayer distance (*a*/2), where *a* is the lattice parameter of Co.

A cosine-type dependence can be easily observed and when mapped onto the Heisenberg model (2.4), the Pt-M and M-M exchange parameters can be extracted. These are shown in Figure 21(c)-(d) for Pt/Fe and Figure 22(c)-(d) for Pt/Co. We further explore the change in these parameters when the distance between the layers is increased. We note that the Pt-Fe {Figure 21(c)} and the Pt-Co {Figure 22(c)} exchange parameters exhibit an oscillatory behavior with respect to distance, and this property extends up to 3*a*, where *a* is the lattice parameter of M. The same oscillatory behavior is observed (although weaker) for M-M exchange parameters.

2.3.3 Metropolis Algorithm

A brief discussion about the algorithm used for the MC simulation is given in this section. MC is used for simulating classical many-particle system by introducing artificial dynamics based on 'random' numbers. Such artificial dynamics allows one to determine static properties of classical and quantum many-particle systems. MC method integrates a smooth function, f, using discrete and equally spaced values , x_i chosen randomly. The function is evaluated at each $x_i \rightarrow f(x_i)$ and summation run to N discretization (or possible configurations) with weight, w_i always equal to 1. How far does

such method deviate from the standard integration varies based on sampling the N. Statistical errors arise if the function is sampled too homogenously leading to significant contribution to the integral coming only from a small region where few MC points are sampled. Therefore, one has to invoke *importance sampling* – points are concentrated in the region where f happens to be large. More precisely, we let $\rho(x)$ be a function which has more or less the shape of f in the sense that f/ρ is approximately constant. We further require that $\rho(x)$ is normalized. When calculating the averages of the canonical or (NVT) ensemble (where V and T are volume and temperature, respectively), the configurations are weighted according to the Boltzmann factor:

(2.20) $\rho(X) \propto \exp[-\beta E(X)],\ \beta = 1/(k_B T)$

This suggests that MC integration is applied over a phase space which can be generated from Metropolis algorithm based on Markov chain [71-74]. Here, new phase space configurations are generated with a probability distribution depending on the previous configuration. The Markov chain of system configurations are such that they have a distribution proportional to (2.20), and this distribution should be independent on the position on the chain and independent of the initial configuration. The Metropolis MC method consists of Markov chains of configurations with a required invariant distribution, which is in our case the Boltzman distribution $\exp[-\beta\mathcal{H}]$. Then, a transition probability, $T(X \longrightarrow X')$ leads to a given stationary distribution $\rho(X)$:

(2.21) $T(X \longrightarrow X')\rho(X) = T(X' \longrightarrow X)\rho(X')$

which is sometimes called the detailed balance solution. In general, the transition probability can be written as:

(2.22) $T(X \longrightarrow X') = \omega_{XX'}A_{XX'}$

where the ω satisfies $0 \leq \omega_{XX'} \leq 1$ and $\sum_{X'} \omega_{XX'} = 1$. And $A_{XX'}$ must lie between 0 and 1 for each pair XX'. Substituting (2.21) to (2.20), gives the detailed balance equation for A:

(2.23) $\frac{A_{XX'}}{A_{X'X}} = \frac{\rho(X')}{\rho(X)}$

To construct the algorithm for T, we use $\omega_{XX'}$ as a trial step probability and $A_{XX'}$ as the acceptance probability. This means the algorithm proceeds into two parts. In the first one, given a state X, we propose a new state X' with a probability given by $\omega_{XX'}$. In the second part, we compare the weights of the old and the new one, $\rho(X)$ and $\rho(X')$. $A_{XX'}$ is chosen equal to 1 if $\rho(X') > \rho(X)$, and it is chosen equal to $\rho(X')/\rho(X)$ if $\rho(X') < \rho(X)$. Thus, we accept the new state X' with a probability $A_{XX'}$, and we reject it with a probability 1-$A_{XX'}$. If the new state, X' is accepted, it replaces X; if the new state X' is not accepted, the system remains in state X. The question now arises how we can accept a state with a probability $A_{XX'} \leq 1$ and reject it with a probability 1-$A_{XX'}$. This is done by generating random number, r uniformly between 0 and 1. If $r < A_{XX'}$, the state is accepted , otherwise it is rejected. If this procedure is carried out many times with the same probability $A_{XX'}$, the state will be accepted a fraction $A_{XX'}$ of the total number of trials. The theory of Markov chain guarantees that we arrive at the invariant distribution ρ for long times. The total number of statistically independent configurations is given by the total number of steps divided by the correlation 'time', measured in Monte Carlo steps. Note that the number of steps is the total number of trials. As we have generated a sequence of configurations X with a statistical distribution $\exp[-\beta\mathcal{H}]$, the ensemble average of a physical quantity A is given by the 'time average' (of course, the time here is not the physical time):

(2.24) $\bar{A} = \frac{1}{n-n_0}\sum_{\nu>n_0}^{n} A_\nu$

where n_0 is the number of steps used for equilibration.

2.3.4 Monte Carlo simulation

The MC simulation is conducted using the standard Metropolis algorithm discussed above. The system size is (L x L x n) - 20 x 20 x 6, where n is the number of atomic planes and L x L gives the atomic sites in a plane. Therefore:

(2.25) $\omega_{XX'} = 1/LxLxn$ if X and X' differ by one spin

$\omega_{XX'} = 0$ otherwise

The realization of the first stage of the Markov step is done by generating a trial configuration via selecting a spin at random. The present configuration is then that which the selected spin is being flipped. The energy of the present $E(X')$ and the old $E(X)$ are obtained using Heisenberg model (2.4). Then the energy difference is calculated:

(2.26) $\Delta E(X \longrightarrow X') = E(X') - E(X)$

Only the nearest neighbor interactions are included. If the energy increases from the old to the new configuration:

(2.27) $\Delta E(X \longrightarrow X') > 0$, the trial state is accepted with a probability:

(2.28) $\rho(X) = \exp[-\beta \Delta E(X \longrightarrow X')]$

If the energy decreases, the trial state is always accepted as the new state. The equilibration steps, n_0 is 500. The average number of steps between two updates of the same spin is equal to *L x L x n*. Therefore the 'time' expressed appropriately as Monte Carlo steps per spin (MCS), 1 MCS is equal to *L x L x n* = 2800 trials. The total MCS conducted is 1000. A two-dimensional periodic boundary conditions and free boundary condition perpendicular to the plane are adopted.

The initial value used for the magnetic moments for Pt, Co and Fe are those that are obtained from DFT calculations in the previous discussion. The decrease of the magnetization with temperature as obtain from the MC simulation is shown in Figure 23 for Pt/Fe and Figure 24 for Pt/Co. The solid line represents the magnetization curve for the Pt layer and the lighter line represent that of 6 atomic layers of M. In Figure 23, we note that Fe(001) exhibits a transition temperature of ~586K. The experimental values of the transition temperature of 3-5 Fe overlayers on different non-magnetic substrates {Au(001), Pd(001)} range from 500-600K [75,76]. So far, this has

been in good agreement with our results. The calculated room temperature magnetic moment of Pt is $0.53\mu_B$, in excellent agreement with the XMCD result for Pt/Fe bimetallic system ($0.50\mu_B$) [41,77]. The transition temperature of the Pt layer is 403K based on the magnetic susceptibility peak as shown in the inset figure. In Figure 24, Co(001) exhibits a transition temperature of 578K, almost the same as in Fe overlayers. However, the Pt-Co exchange parameter is lower resulting to a lower transition temperature of 354K. The magnetic susceptibility plot is also shown in the inset figure. The magnetic moment of Pt in Pt/Co at room temperature is $0.22\mu_B$, which is in agreement with XMCD of Pt in Pt/Co(001) LS ($0.20\mu_B$) [44,78]. Therefore, the magnetic properties of the Pt in Pt/M have already been observed experimentally at room temperature (RT), however, this work shows the magnetic phase transition of the system, which has not been explored before. Table 6 summarizes the values given above.

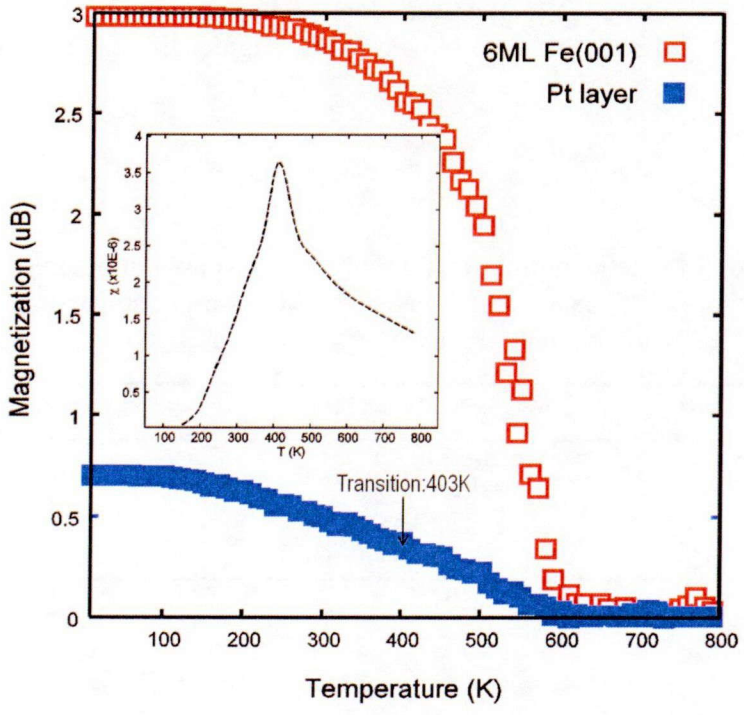

Figure 23: Temperature dependence of the magnetization of Pt on Fe. The inset figure shows the temperature dependence of magnetic susceptibility of Pt layer. Solid blue line for Pt layer and red lighter line for 6 ML Fe(001).

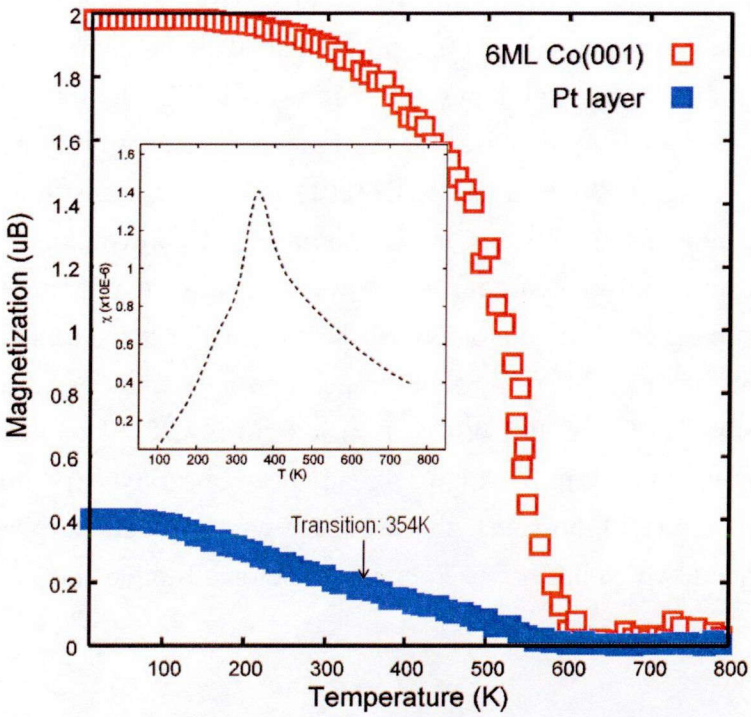

Figure 24: Temperature dependence of the magnetization of Pt on Co. The inset figure shows the temperature dependence of magnetic susceptibility of the Pt layer. Solid blue line for Pt layer and red lighter line for 6 ML Co(001).

Table 6: Magnetic moment of Pt on M at room temperature and transition temperature of Pt layer and 6 layers of M. Comparison with experiments are made when available and are given in parenthesis.

System	Magnetic moment (μ_B)	Transition Temperature (K)
Pt (on Fe)	0.53 (0.50[a])	403
Pt (on Co)	0.22(0.20[b])	354
Fe (6 ML)	2.76(2.58[c])	586 (500-600[e])
Co (6ML)	1.89(1.80[d])	578

[a] Ref. 41
[b] Ref. 44
[c] Ref. 77
[d] Ref. 78
[e] Ref 69,76

Chapter 3
Dehydrogenation of BH_{4ad}

3.1 BH_{4ad} on Pt vs Os

As discussed in Chapter 1, there is a general consensus that hydrogen evolution is prevalent on Pt and is attributed to the high activity of the catalyst towards hydrolysis of borohydride [34-37]. So far, there has been no idea on why such reaction occurs until recently, a large surface coverage of H_{ad} have been proposed based on a fundamental electrochemical study employing a combination of cyclic voltammetry and electrochemical quartz micro-balance [79]. The latter method allows one to determine the mass change on the surface. Based on the large increase in surface area coverage (via the increase of mass), a saturation of certain surface species is assigned to the first oxidation wave (a1) (Figure 25). It is further suggested that this peak can be described by a electrochemical-chemical sequence of steps: (1) $BH_4^- \rightarrow BH_{4ad} + e^-$ and (2) $BH_{4ad} \rightarrow BH_{ad} + 3H_{ad}$.

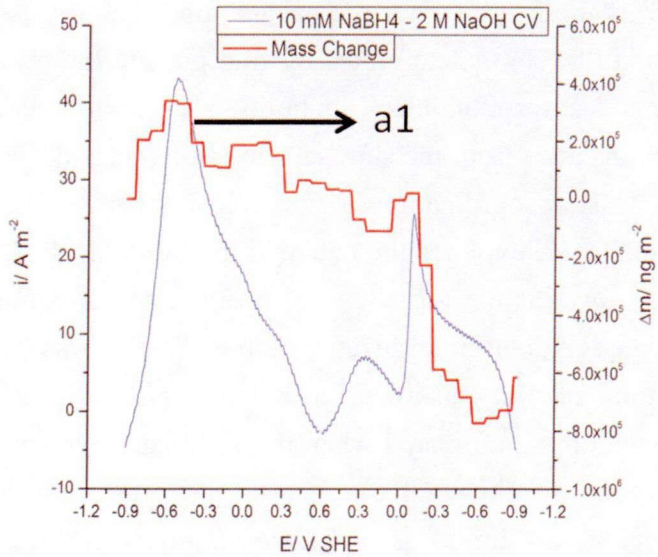

Figure 25: Cyclic voltammetry and surface mass changes of the Pt electrode in 10mM $NaBH_4$. [79]

The presence of high coverage of H_{ad} on surface predicts the tendency for H_2 evolution owing to the second- order rate of the reaction: $H_{ad} + H_{ad} \rightarrow H_{2,gas} + 2(sites)$ or to some extent, to the first order H_{ad} oxidation: $H_{ad} + OH^- \rightarrow H_2O + 1e^-$. In this research, we determine the interaction of BH_{4ad} with Pt to give insights on the chemical step (2). These insights should involve: (1) the stable structure of BH_{4ad} and (2) B-H bond breaking in Pt and (3) the Pt electronic structure effect. Below are the computational modeling methods and parameters used.

3.1.1 Computational modeling

The fundamentals of the BH_{4ad} interaction with Pt are studied using DFT [45-47]. GGA-PBE [50,51] is used for the exchange-correlation functional and the PAW method [48,49] is employed to describe the ion-valence electron interactions. A supercell with a 4-layer fcc(111) metal slab and ~15Å of vacuum is used to simulate the metal surface. The slab is optimized by relaxing the two top-most layers. A 3x3 surface unit cell is employed corresponding to an adsorbate coverage of ~1/9ML with respect to the number of surface atoms. Typical concentrations of borohydride are low [79]. Brillouin-zone integrations are performed on a grid of (4x4x1) Monkhorst-Pack k points with a smearing of Methfessel-Paxton method [52]. A plane-wave expansion with a cutoff of 400 eV is used throughout the calculations. The most stable configuration of BH_{4ad} on Pt(111) is determined by first placing the center of mass (boron) on four major adsorption sites (fcc-hollow, hcp-hollow, bridge and top) at 1.80Å vertical distance from the surface. This is denoted as "down" configuration – a trigonal BH_{4ad} coordination as shown in Figure 26. Then, an in-plane rotation of the molecule explores the potential minimum. If the BH is on bridge and the H spans towards the top site, the configuration is denoted as bridge-top. The conjugate gradient minimization method [53] was used for the structural relaxation of the adsorbate and the top-two layers of the metal slab. Optimization is terminated when the Hellman-Feynman forces acting on each atom dropped below 0.01eV $Å^{-3}$. We used the same calculated equilibrium lattice constants for Pt as in Chapter 2, in agreement with experiments and other DFT calculation [54-56]. The B-H bond length of the molecule is 1.25Å and the H-B-H angle is 109° in agreement with experiment {1.255 $\pm$ 0.02Å, 109°} [80]. The surface relaxation calculated for the 4-layer fcc Pt(111) is

~1.0%, which is in excellent agreement with experiments (<2%) [81] , (1.3 ± 0.4%) [82]. The binding energy, E_b of the adsorbate on the metal surface is defined as:

(3.1) $E_b = E_T - (E_M + E_g)$

where E_T is the total energy of the adsorbate/metal system, E_M is the total energy of the bare metal slab and E_g is the energy of the gas phase adsorbate.

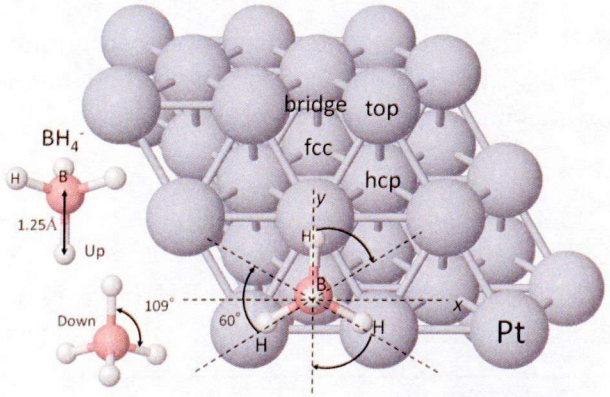

Figure 26: BH_{4ad} configuration on Pt surface. The major adsorption sites are indicated as fcc, hcp, bridge and top sites. In-plane rotation of the molecule is depicted on hcp-hollow site. The same rotation is employed on the other three adsorption sites. The B-H bond length and bond angle for gas-phase BH_4^- are shown.

3.1.2 BH_{4ad} structure on Pt

In Figure 27, we show the dissociated structure in the form of BH_{ad} +$3H_{ad}$ as the most stable structure of the molecule on Pt. BH_{ad} is in the hcp site and the H_{ad} is on the next neighboring top site. The B-H bond distance is 3.27Å. It appears that there is a diffusion of H_{ad} on the surface via the fcc hollow site. This easy diffusion of H is the same as those proposed on pure Pt (in the absence of borohydride species) [83]. Thus, the chemical step (2) has been confirmed. The binding energies for the other configurations are shown in Table 7.

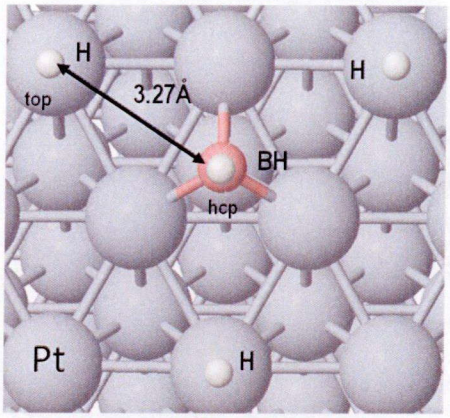

$BH_{ad} + 3H_{ad}$

Figure 27: The most stable adsorption configuration of borohydride on Pt: $BH_{ad} + 3H_{ad}$. The B-H distance is shown. This large distance implies diffusion of H towards next neighboring top site.

Table 7: Chemisorption data for BH_{4ad} on Pt(111) on six most stable configurations. The initial state is used to label the configurations.

Configuration	E_b(eV)	FS structure
bridge-hollow	-4.31	BH(fcc)+3H(top)
bridge top	-4.32	BH(fcc)+3H(top)
fcc-bridge	-2.38	BH(fcc)+3H(bridge)
fcc-top	-4.33	BH(fcc)+3H(top)
hcp-bridge	-4.56	BH(hcp)+3H(top)
hcp-top	-3.23	BH(hcp)+3H(top)*

*neighboring top site where BH is also bonded.

3.1.2 The B-H breaking on Pt

The initial configuration for this reaction is a hcp-bridge configuration as shown on the right panel of Figure 28. The PE curve on the left indicates that there is no barrier in the B-H breaking process. These reaction energies are obtained by scanning the PE along the path shown on the right. This curve suggests that if there is any observable on the electrode surface, it has to be BH and H, or BH- and H-derived species. And this leads to saturation of such species such that the mass change (increase) as observed in the quartz

microbalance results (recall Figure 25).

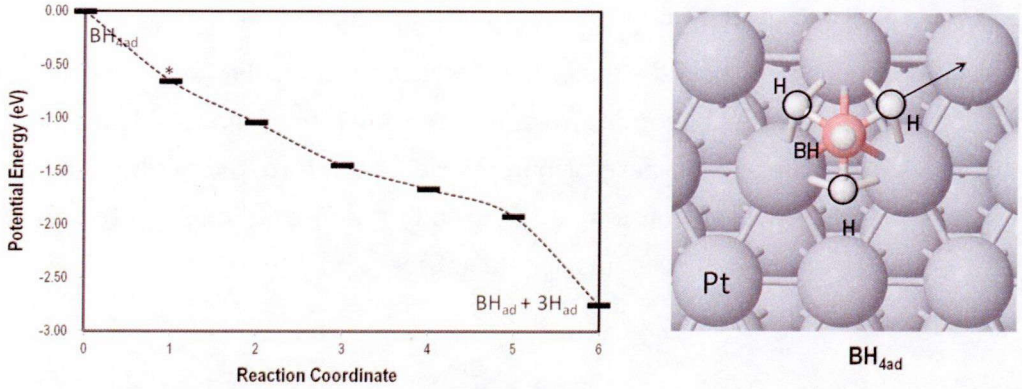

Figure 28: (Left) Reaction energy corresponding to B-H bond breaking on Pt. (Right) The initial state configuration and reaction pathway is shown by the arrow.

3.1.3 BH_{4ad} structure on Os

The same reaction as above is tested on the metals on the same period (5d). The same computational modeling used for reaction on Pt is adopted. The lattice parameter of Os, Ir, and Au are 3.85Å, 3.88 Å, 4.18 Å, consistent with previous DFT calculation (3.86 Å, 3.88 Å, 4.18 Å) [84,85]. The dissociated (D) or molecular (M) structures and the binding energies are shown in Figure 29.

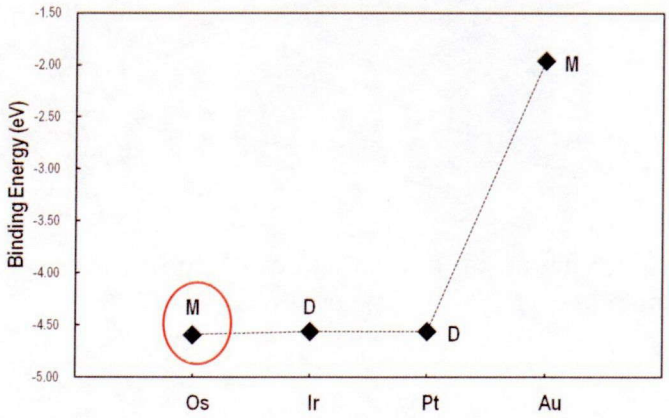

Figure 29: Binding energies of borohydride on 5d metals. The dash line is just a guide to the eye. The final adsorption structure is indicated as M (molecular) and D (dissociated).

We note that even for almost the same binding energies of the BH_{4ad} on Os, Ir and Pt, the borohydride adsorbs molecularly on Os. On Au, the molecule is much less bound, thus, the resulting molecular structure is not entirely surprising. The atomic structures are shown in Figure 30. The gas phase radical is not the stable phase of borohydride, therefore, the binding energies here are large, however, for comparative study purposes, the use of the same gas phase reference for all systems should suffice.

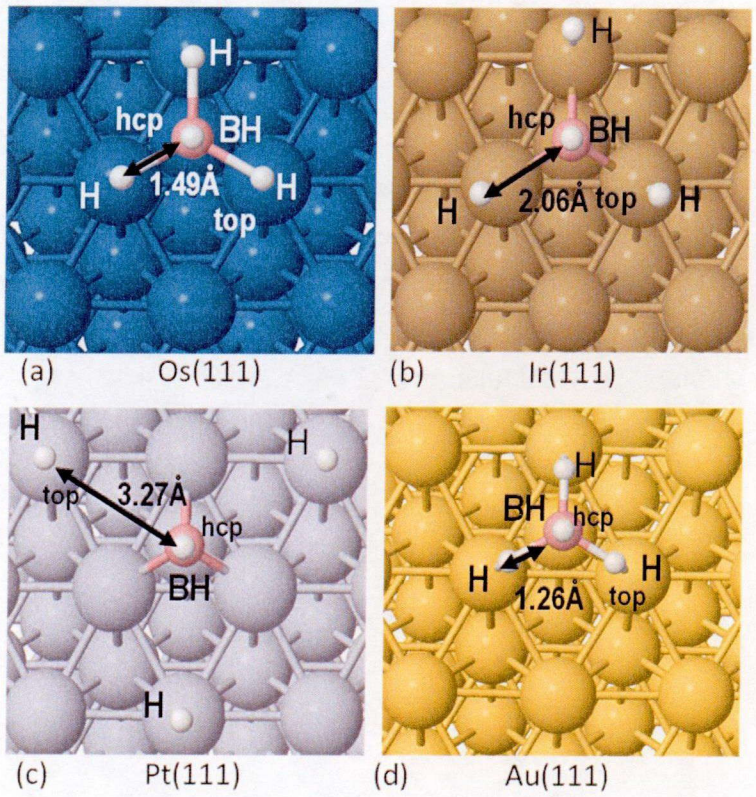

Figure 30: Final adsorption structures of borohydride on 5d metals. The B-H bond length in each system is shown.

3.1.4 B-H breaking on Os

The reason for the dissociative and molecular adsorption on Pt and Os, respectively, should be drawn. There's a clear indication in Figure 29 that the

final adsorption structure does not rely on the binding energy or in other words, on the strength of the interaction. Thus, an orbital-specific analysis is sought to distinguish the two different reaction types. First, we show the PE curve for the B-H breaking on Os in Figure 31. We note that the barrier is ~0.04eV. This is quite small owing to the already stretched molecule on the surface (19% with respect to gas phase). The final dissociated structure is endothermic.

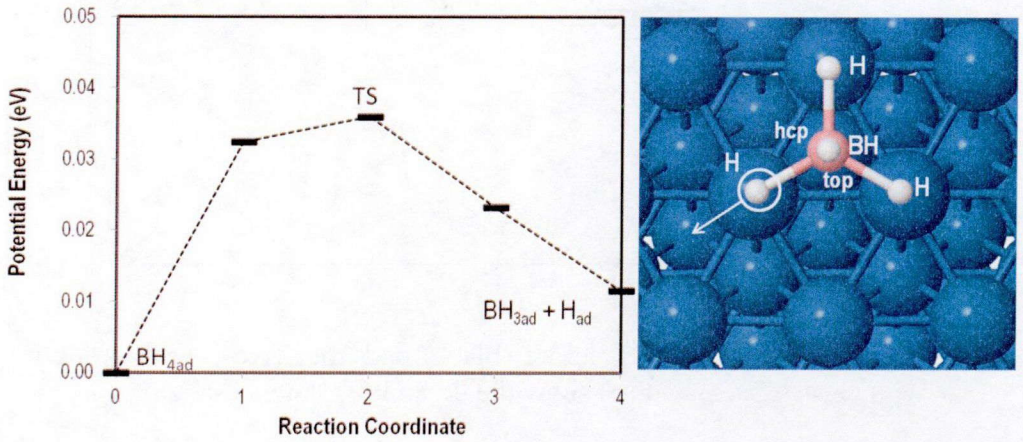

Figure 31: Potential energy curve for the dissociation of B-H1 bond on Os

Figure 32 shows the LDOS plots before and after borohydride interaction with Os at TS. These are the density of d-states projected on the surface atoms. Meanwhile, the LDOS plot for Pt is shown in Figure 33. This LDOS is derived from the configuration at reaction coordinate 1 in Figure 28. First, for the Os, we note that the d_{zz} state mainly contributes to the BH_{4ad}-Os interaction. There is basically no change in the d_{yz} state. This explains why the hcp(BH)-top(H) configuration is preferred. The d_{zz} state can easily overlap with H-s state (see Figure 31 right panel). The LDOS for the gas phase molecule is given in Figure 34. Here, we see that the lowest unoccupied orbital is a spin-down state arising from H-s, B-p_z and B-p_x contributions. The highest occupied molecular orbital which is very close to the E_F is a spin-up state also originating from H-s, B-p_z and B-p_x states. Significant contribution originates from the B-p_z and B-p_x states. Thus interaction between Os-d_{zz} and H-s renders minimal change in this

metal d-band. The binding energy of the other configurations of BH_{4ad} on Os are given in Table 8.

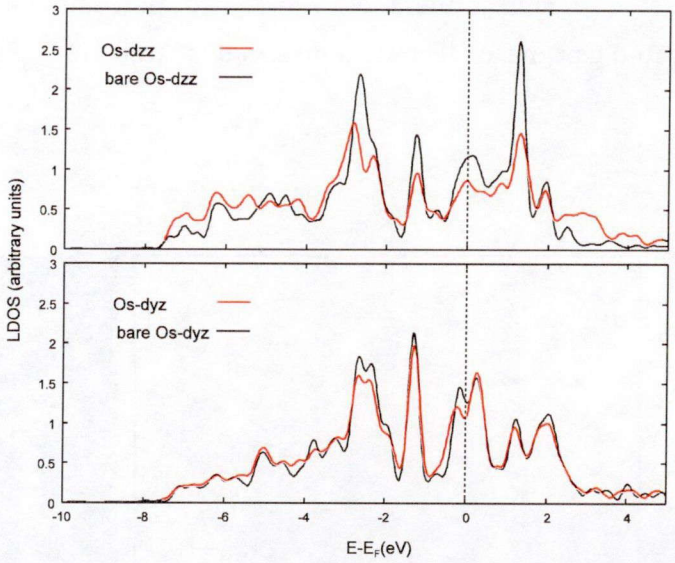

Figure 32: LDOS plots before (black) and after (red) borohydride interaction with Os at TS. (a) and (b) show the d_{zz} and d_{yz} states respectively.

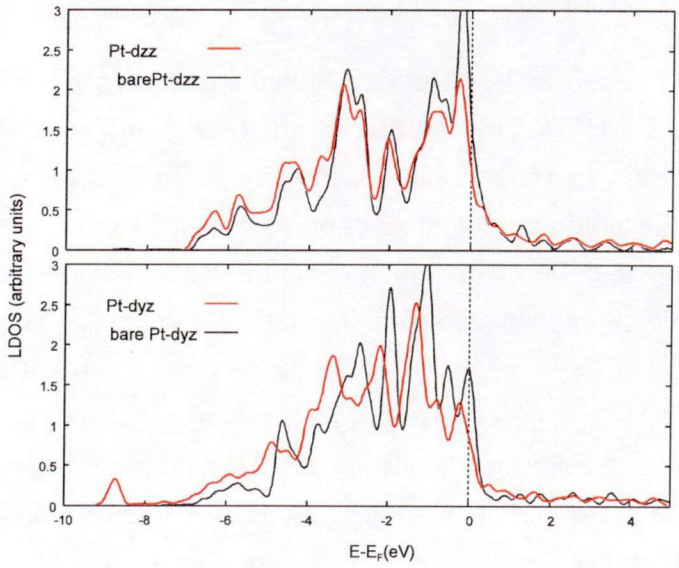

Figure 33: LDOS plots before (black) and after (red) borohydride interaction with Pt. (a) and (b) show the d_{zz} and d_{yz} states respectively.

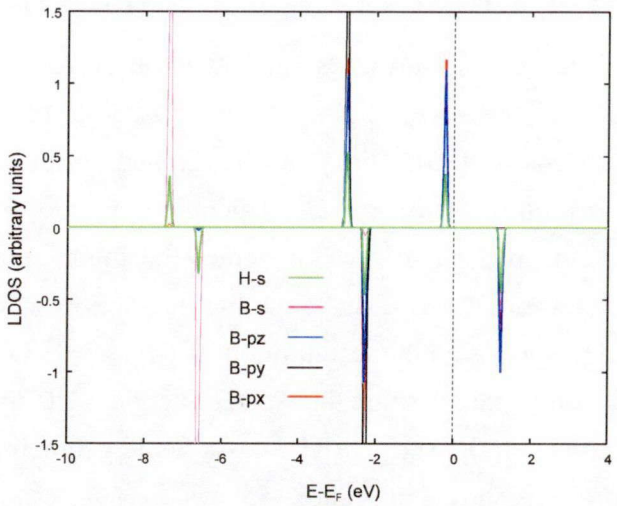

Figure 34: LDOS of isolated borohydride molecule. Contributions from H-s and B-s,p states are shown in colored lines.

Table 8: Chemisorption data for BH_{4ad} on Os(111) on six most stable configurations. The initial state is used to label the configurations.

Configuration	E_b(eV)	FS structure
bridge-hollow	-4.33	BH(hcp)+2H(b)+H(fcc)
bridge-top	-4.35	BH(hcp)+2H(b)+H(t)
fcc-bridge	-3.38	BH(fcc)+3H(hcp)
fcc-top	-4.47	BH(fcc)+3H(top)
hcp-bridge	-3.54	BH(hcp)+H(fcc)
hcp-top	-4.59	BH(hcp)+3H(top)

On the other hand, for Pt(111), in Figure 33, the d_{zz} exhibits drastic change of DOS at E_F. The shifting of this band is not prominent as in the Os. However, the d_{yz}-states are shifted. This state can very well interact with B-p_x The breaking of B-H on Pt can then be enhanced by Pt d_{yz} – B p_x interaction. The characteristics of the d_{zz} and the d_{yz} –states of bare Pt both contribute to the final dissociated structure of the molecule.

3.2 BH_{4ad} and H_2O_{ad} co-adsorption on Os

The hydrogen evolution on Os catalyst is observed to be minimal if an ionic liquid is used, however, when water is used as the solvent the hydrolysis reaction speeds up [86]. These are then indication of vulnerability of the final structure of borohydride on Os depending on the environment or external factors. Also, in the hydrolysis reaction the interaction of the molecule with water is relevant. We discuss below the interaction with H_2O monomer on the surface. The most stable configuration of BH_{4ad} + H_2O_{ad} adlayer on Os(111) is obtained after calculating the total energies of the possible symmetric configurations on the surface. The most stable geometry for the BH_{4ad} + H_2O_{ad} adlayer on Os is shown in Figure 35.

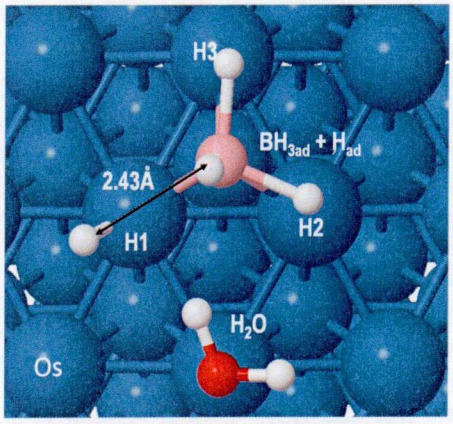

Figure 35: The most stable BH_{4ad} + H_2O_{ad} adlayer structure on Os. The dissociated H atom distance from B is shown.

Here, we clearly see the change in the BH_{4ad} structure as a consequence of the interaction: BH_{4ad} → BH_{3ad} + H_{ad}. The H1 is dissociated from the B atom. This breaking of B-H1 bond is considered to be due to the adsorbate's electrostatic interaction with H_2O_{ad}. We verify this conjecture in the following. First, we show in Figure 36, the LDOS before and after H_2O monomer adsorption (without BH_{4ad}). We note that the d-states of Os are not modified upon H_2O adsorption. Therefore, there is no contribution from the electronic structure change of the surface due to water monomer adsorption.

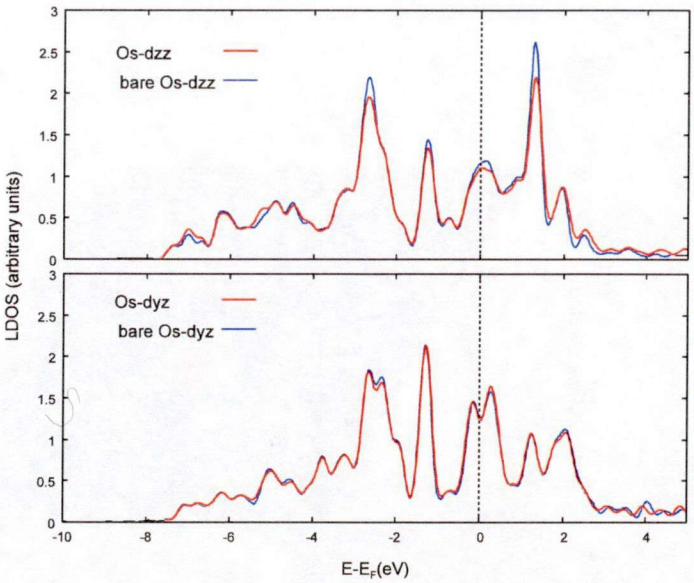

Figure 36: LDOS plot showing the (a) d_{yz} and (b) d_{zz} orbitals of Os, before (blue) and after (red) water adsorption.

Next, we show the polarity of the BH_{4ad} on Os using electron localization function plot (ELF), Figure 37. ELF provides a faithful visualization of valence shell electron pair repulsion theory [87] which gives better information of the nature of binding than the total charge density. This is done via the topology of electron localization (pair probability) [88]. The charge topology derived in this work suggests that there is significant charge polarity along the B-H bonds. In fact, there has been speculation on the charge polarity of BH_{4ad} on metals [89]. Here, we verify the nature of BH_{4ad} on metal surface. Because of the high charge polarity in these bonds, then an electrostatic nature of the interaction of the BH_{4ad} + H_2O_{ad} adlayer, which involves repulsion of H1 of BH_{4ad} and H of H_2O_{ad}, is highly likely. However, a question arises whether this suffices to break the B-H1 bond. Previously in Figure 31, we showed the dissociation barrier on Os with no water co-adsorption. This small barrier can be understood by the already significantly elongated B-H1 bond (initial state) upon interaction with Os. The electrostatic nature of the interaction of the adlayer which involves repulsion of H1 and H of H_2O_{ad} should be sufficient to break the B-H bond. In Figure 38(b), we show the PE curve for B-H breaking on Os with H_2O_{ad} co-adsorption. We note that the dissociation barrier disappears upon H_2O_{ad} interaction. Therefore, we clarify the promotion of B-H

bond dissociation due to water co-adsorption effects.

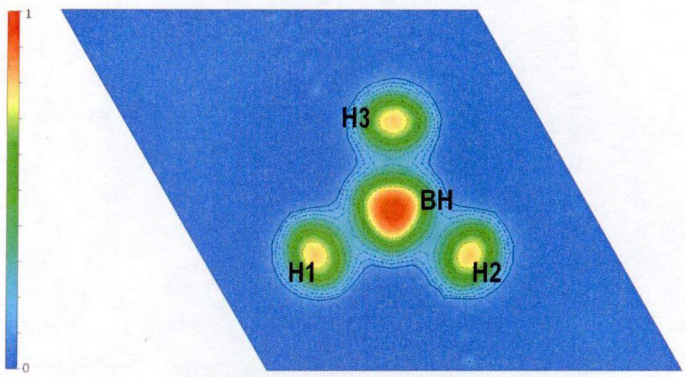

Figure 37: Electron localization plot showing the charge polarity of BH_{4ad}.

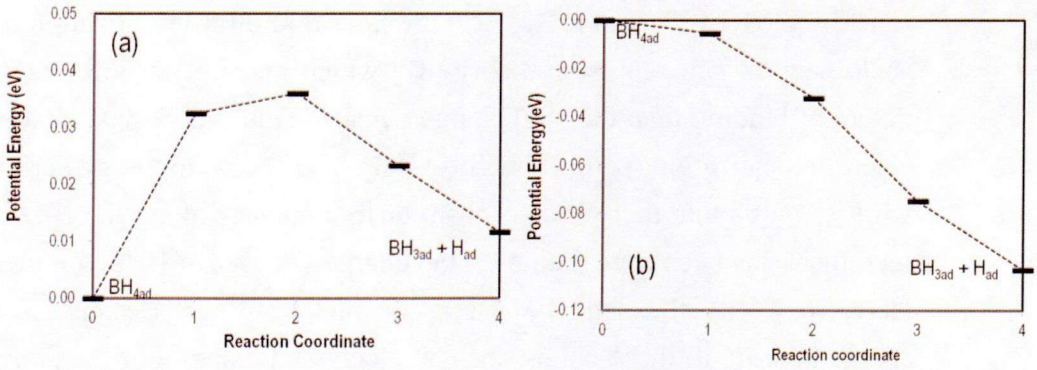

Figure 38: Potential energy curve for the dissociation of B-H1 bond without (a) and with (b) water co-adsorption. (a) is included for easier comparison.

When another H_2O monomer is added to the system (Figure 39), the same enhancement of the B-H bond dissociation in the other two B-H bonds is observed. Therefore, the BH_{4ad} + H_2O_{ad} overlayer, can still capture the interaction of adsorbed borohydride and water in the inner Helmholtz layer within a double layer [90,91]. Basically, the general idea is that the presence of water molecules promote B-H breaking on Os.

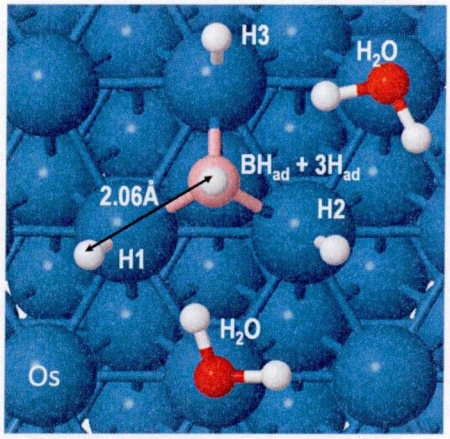

Figure 39: The most stable BH_{4ad} + $2H_2O_{ad}$ adlayer structure on Os. The dissociated H atom distance from B is shown.

3.3 Electric field effects on Os

The uniform electric field is applied to BH_{4ad}/Os as well as to BH_{4ad} + H_2O_{ad} adlayer on Os by introducing a dipole sheet in the middle of the vacuum region. This dipole sheet is responsible for polarizing the slab [92,93]. In this model (or in fact any other models used to impose electric field [94-96]), the electric potential distribution in the vacuum region can be derived from classical electrostatics and is governed by Poisson's equation:

$$(3.2)\quad \nabla^2\phi = -\frac{\rho}{\varepsilon_0}$$

where the ρ is the charge density and ε_0 is the permittivity of free space. The electric field F is related to the potential by:

$$(3.3)\quad F = -\nabla\phi$$

The boundary conditions for the Poisson's equation over the vacuum region are provided by the electric fields at the surface of the slab:

$$(3.4)\quad F_{surface} = \frac{\sigma}{\varepsilon_0}$$

where σ is the surface charge density.

Figure 40 shows the schematic representation of the potential distribution in a supercell with and without the applied external field. We see that because ρ is zero in the vacuum then a linear variation of the potential is obtained, which means a uniform electric field is imposed. The plane-averaged potential in the unit cell of our system at different intensities of the electric field is shown Figure 41.

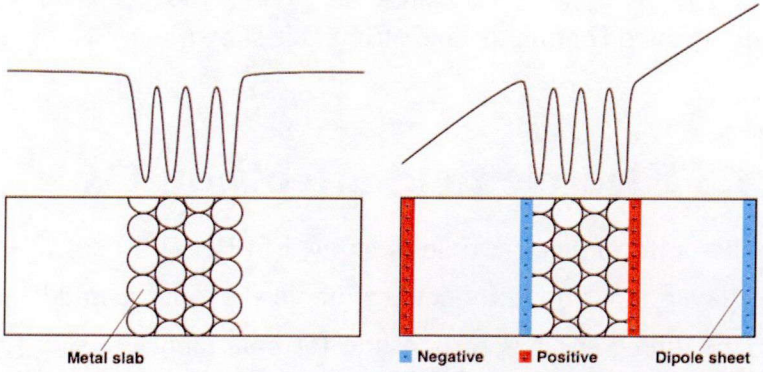

Figure 40: (Right panel) Potential distribution in the unit cell corresponding to the polarization of the slab. (Left) Potential distribution in the unit cell with no external field.

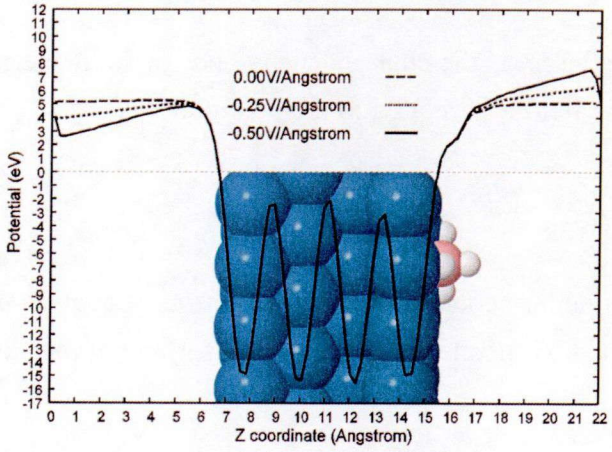

Figure 41: Plane-average potential in the unit cell for various intensities of the electric fields.

We note potential drop in the vacuum region but none in the bulk region. This indicates that the polarization does not affect charge distribution in the bulk. The values of the potential drop are shown in Figure 42. A -0.50V/Å field (the sign only indicates the direction of the field with reference to Figure 40) leads to a potential drop of ~2.5eV on both sides of the slab.

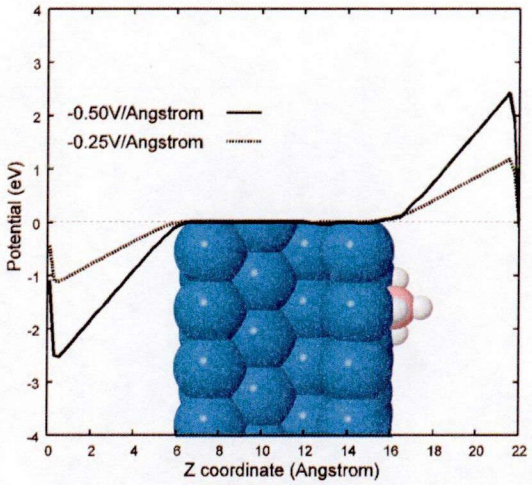

Figure 42: Plot of the potential drop in both sides of the slab due to induced electric fields.

Next, we checked the change in the stability of the adsorbate as a function of the applied electric field. The binding energy of the adsorbate in the electric field is defined as:

(3.5) $E_{bf} = E_{Tf} - (E_{Mf} + E_g)$

where E_{Tf} and E_{Mf} are the total energies of the adsorbate/slab and bare slab in electric field, respectively.

The change in energy is :

(3.6) $\Delta E = E_{bf} - E_b$

which is the binding energy shift due to the electric field. The energy shift

dependence on electric field as shown in Figure 43. This is not linear, hence, indicating contribution from first and second order Stark effect:

(3.7) $\Delta E = -\mu_0 F - 1/2\ \alpha F^2$,

where μ_0 is the adsorbate's dipole moment and α is the adsorbate polarizability ($d\mu = \alpha dF$).

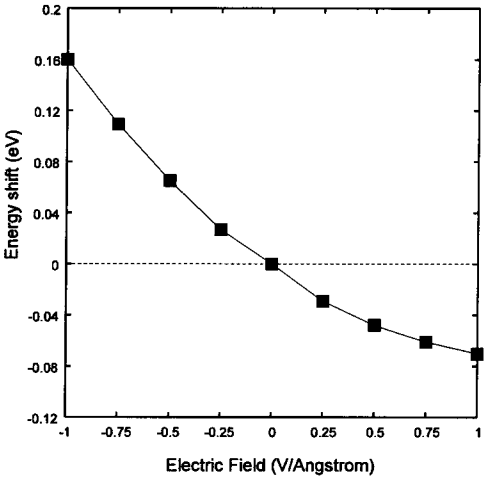

Figure 43: Dependence of the binding energy shift on the intensity and direction of the electric field.

Using least squares fitting to the curve in Figure 43, we obtained the values μ_0 = 0.12eÅ and α = 0.05 $eÅ^2V^{-1}$. Based on these values we can suggest that the (de)stabilization of the adsorbate is mainly due to dipole moment interaction with the field and minimally due to its polarizability. Because of the change in the stability of the molecule, then we can expect changes in the final geometry. The changes in the structure of BH_{4ad} (focusing on B-H1 bond length) due to these energy shifts are shown in Figure 44. We see a minimal change in the B-H bond length (0.01-0.02Å per 0.25V/Å increase in electric field) due to the fact that the energy shifts are also very minimal (0.02-0.06eV) (see Figure 43). For practical reasons, we focused only on the negative fields which correspond to the anode side.

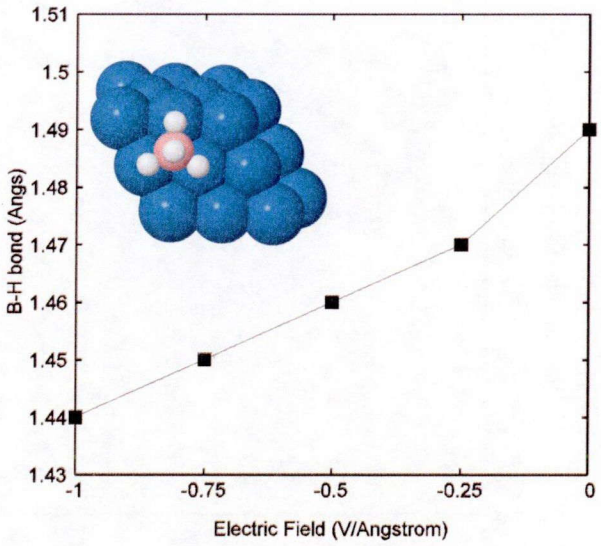

Figure 44: The change in the atomic structure, specifically B-H bond lengths, of borohydride due to the electric field.

More interestingly, in Figure 45, we note that the effect of the water in the promotion of elongation in the "no-electric field" case is significantly reduced in the presence of electric field. We see that that the change in the B-H1 bond length (changes are also observed in B-H2 and B-H3 bonds, however, very minimal as verified in Figure 44) due to interaction with H_2O_{ad} decreases when the intensity of the field increases. The explanation for this is depicted in the plot described by the circle data series showing the H_2O_{ad} – metal distance. When the electric field is applied and increased, the distance of the water from the surface is decreased. The water is stabilized. As a consequence, the interaction energy between the two adsorbates is reduced. The origin of this can be seen in the reduced electrostatic interaction due to the orientation of H (deviation from planar) in the applied electric field.

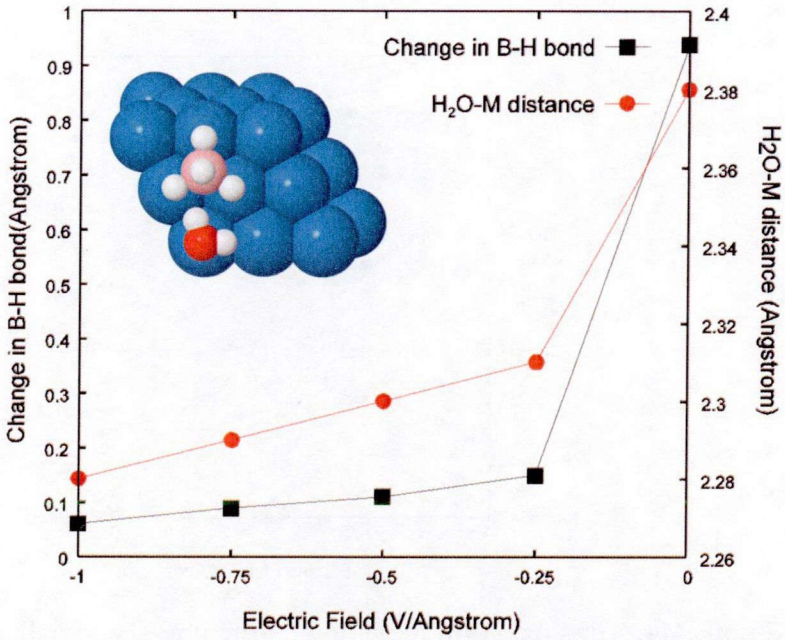

Figure 45: Changes in the atomic structure (B-H1 bond) of BH_{4ad} due to water co-adsorption and applied electric field. The H_2O-M distance is plotted to account for the effect of electric field in the BH_{4ad}-H_2O_{ad} interaction.

Chapter 4
Conclusions and Outlook

4.1 Summary and Findings

DFT calculations are conducted to study the reaction of simple molecules, such as oxygen and borohydride, on metals, focusing on the energetics, geometric and electronic properties, to provide understanding of O_2 activation on Pt and Pt/M surfaces and explanations on dehydrogenation of BH_{4ad} on Pt and Os metal surfaces.

Below are the findings in relation to:

1 Magnetic effects on O_2 reaction on Pt:

1.1 Decrease in both the oxygen dissociative adsorption barrier and the dissociated oxygen atom binding energy on ferromagnetic Pt/M where M:Fe,Co with respect to that of the reference system, Pt(100)-(1x1). An emergence of non-activated dissociative adsorption on Pt/Fe.

1.2 The effective O-O bond elongation on Pt/M is due to π^* -d_{zz} hybridization with the significant occupation of the $\pi^*_\perp$-state. The spin-down component of $\pi^*_\perp$ is filled in Pt/Fe, partially filled in Pt/Co and empty in Pt. The enhanced π^* -d_{zz} hybridization is due to shifting of the spin-down component of d_{zz} towards E_F, which now becomes higher in energy as compared to the filled d_{zz} state of pure Pt. The shifting of the d_{zz} state is attributed to the spin-polarization of Pt as a result of interaction with the substrate, M.

1.3 The transition temperature of the ferromagnetic Pt/M is found to be higher than room temperature (403K on Fe and 354K on Co), indicating that the reactivity of ferromagnetic Pt/M is retained at a wide temperature range. The relatively high transition temperature is due to strong Pt-M interlayer exchange interaction.

2 Changes in borohydride structures with respect to catalyst (Pt vs Os), water co-adsorption, and applied electric field:

2.1 Borohydride adsorption is dissociative on Pt(111) but molecular on Os(111). This difference in the adsorption leads to difference in the adsorption structures: (a) BH_{ad} +$3H_{ad}$ on Pt(111) and (b) BH_{4ad} on Os(111). The B-H breaking process is non-activated on Pt and is activated on Os.

2.2 The difference in the B-H bond breaking on Os and Pt arises from the nature of the d_{yz} and d_{zz} states at the E_F and not on the strength of the adsorbate's binding on the surfaces. These states are highly "peaked" at the E_F in Pt, contrary to that of Os. The BH_{4ad} interaction with Os only involves d_{zz} states, while in Pt, it involves the interaction with both the d_{zz} and d_{yz} states, which result to easier breaking of bond over the bridge site.

2.3 However, the B-H breaking on Os is promoted upon H_2O_{ad} co-adsorption. The efficient B-H breaking in Os is due to electrostatic interactions with H_2O_{ad}. There is no change in the surface electronic structure due to adsorption of water monomer but based on the electron localization plot, a significant charge polarization in B-H bond is observed.

2.4 In the presence of electric field, the binding energy of the BH_{4ad} shifts due to first and second order Stark effect. This (de)stabilization, in turn, minimally changes the B-H bond lengths. For the case of BH_{4ad}+H_2O_{ad} adlayer on Os, the promotional effect on B-H bond elongation discussed in (2.3) above is reduced. This is due to stabilization of water monomer with a deviation of H from the planar configuration on metal surface due to the electric field.

4.2 Future prospects

4.2.1 Oxidation reaction:

The easy dissociation of O_2 on Pt/M has been observed in half-cell experiments. A direct comparison with the results is not evident. UHV experiments are more suitable and are being sought.

However, recent paper of Watanabe group [97] has discussed several viable structures including Pt/M in half-cell experiments. Therefore, theoretical studies involving the use of Pt/M simulated employing liquid/solid interface

model (e.g. inner Helmholtz layer of the cathode), can be conducted in parallel to these.

4.2.2 Dehydrogenation reaction:

There is a good agreement between the dissociative adsorption of borohydride on Pt and the increase in mass of surface species after borohydride electrosorption, which is the chemical step: $BH_{4ad} \rightarrow BH_{ad} + 3H_{ad}$. This agreement can be strengthened if spectroscopic studies are done, to confirm BH_{ad} and H_{ad}-derived species are the main observables on the surface. The effect of water on the final adsorption structure of borohydride on Os has been experimentally confirmed. The verification on the electric field effects, however, is still yet to be done. Over all, the phenomena (1) and (2), studied and the accompanying mechanistic and electronic explanations have benefitted several experimentalists to further their research, specifically in alternative power generation systems such as fuel cell.

Such surface science studies are still very important in determining nature of "local" interactions within complex systems or environment. Bringing the surface science studies to more complex systems is just a matter of well-defining a "purpose" and in such comes knowledge of the appropriate "scale" (nano, mesoscopic, macroscopic) to use. Future theoretical studies beyond the atomic scale can be built upon the results of the surface science approach used in this work.

4.3 Outlook

The surface reaction and surface magnetism has always been taken as separate fields. The findings of the research on magnetic effects on oxidation of Pt (part 1 of the thesis) serve as the demonstration on how the two can be merged. Of course, the link between these two areas does not solely rely on changing the d-orbitals of the metal surface. There are many more possibilities that can arise from this study. For instance, different magnetic configurations of metal oxides surfaces like MnO_2 which is also used as anode catalyst, can lead to different stable structure at a particular temperature. Structure-function relationship is the key to device design and structure-reaction relationship is central to

chemical reactions. Also, CeO_2, which is used in diesel oxidation catalyst can exhibit intrinsic FM behavior with oxygen vacancy formation. Probably most metal oxide surfaces do, but no one has explored into this so far since FM or other surface magnetic configurations or behaviors and catalytic reactions have not found a common ground. Therefore, this future research direction is very important to take into account.

On the other hand, the understanding of the interaction of borohydride with metal catalysts, water monomer and electric field from a theoretical study is important whether in its electro-oxidation (anodic fuel) or in hydrogen generation (hydrogen source – in-situ or ex-situ). Different interactions with metal catalysts and with external parameter lead to different borohydride structures, which has not been probed before. Therefore, considering the fact that the structures, which are basically B-H bond lengths, can be changed by knowledge of these interactions, then, it is possible to control the structure by a combination of these factors. The further use of borohydride for the technological applications pointed above can be advanced at some point by such theoretical studies. However, the future research on borohydride would most probably focus on its recyclability (borate as by-product back to borohydride), especially when used as an anodic fuel. Even then, the basic understanding of borohydride interaction with catalyst and the external parameters (water and electric field) remains a strong starting point.

Appendix: DFT and Its implementation

Below is the background of the density functional theory (DFT) calculations conducted in this study. The concepts and methods are presented and their use in the computational modeling of the systems is integrated (italicized portions):

A.1 Theory of structure of matter

We can describe the system {i.e. ensemble of particles which can be in the gas phase (molecules,clusters) or in condensed phase (bulk, surfaces)} as a set of atomic nuclei and electrons interacting via coulombic, electrostatic forces. The Hamiltonian of the system is :

(A.1)

$$\hat{H} = \sum_{I=1}^{P} \frac{\hbar^2}{2M_I} \nabla_I^2 - \sum_{i=1}^{N} \frac{\hbar^2}{2m} \nabla_i^2 + \frac{e^2}{2} \sum_{I=1}^{P} \sum_{J \neq I}^{P} \frac{Z_I Z_J}{|\mathbf{R}_I - \mathbf{R}_J|} + \frac{e^2}{2} \sum_{i=1}^{N} \sum_{j \neq i}^{N} \frac{1}{|\mathbf{r}_i - \mathbf{r}_j|} - e^2 \sum_{I=1}^{P} \sum_{i=1}^{N} \frac{Z_I}{|\mathbf{R}_I - \mathbf{r}_i|}$$

where $\mathbf{R} = \{\mathbf{R}_I, I=1,\ldots,P\}$ is a set of P nuclear coordinates, and $\mathbf{r} = (\mathbf{r}_i, i=1,\ldots,N\}$ is a set of N electronic coordinates. Z_I and M_I are the nuclear charges and masses, respectively. In principle, all the properties can be derived by solving the time-independent Schrödinger equation:

(A.2) $\hat{H}\Psi_n(\mathbf{R},\mathbf{r}) = \varepsilon_n \Psi_n(\mathbf{R},\mathbf{r})$

where ε_n, are the energy eigenvalues and $\Psi_n(\mathbf{r},\mathbf{R})$ are the corresponding wave functions which must be antisymmetric with respect to exchange of electronic coordinates in **r**, and symmetric or antisymmetric with respect to nuclear variables in **R**. Mostly, there is no exact numerical solution to this equation due to: (1) it is a multi-component many-body system; (2) the two-body nature of the Coulomb interaction makes the equation not separable.

A.1.1 Adiabatic approximation

The time scale associated with the motion of the nuclei is usually much smaller than that associated with electrons. Born and Oppenheimer [98] proposed that the motion of nuclei can be separated from that of electrons. This is done by

solving the time-independent Hamiltonian "perturbatively" using mass ratio $k = (m/M)^{1/4}$, where m is the mass of electron and M is the mass of proton. In the following, we present the quantum mechanical derivation from time-dependent perturbation theory, which allow one to inspect the limits of the validity of the adiabatic approximation: The electrons can be thought of as instantaneously following the motion of the nuclei, while remaining always in the same stationary state of the electronic Hamiltonian. This can be cast in a mathematical framework by proposing a solution to Eq. (A.2):

(A.3) $\Psi(\mathbf{R}, \mathbf{r}, t) = \sum_n \Theta_n(\mathbf{R}, t)\Phi_n(\mathbf{R}, \mathbf{r})$

where $\Theta_n(\mathbf{R}, t)$, are the wave functions describing the evolution of the nuclear system in each one of the adiabatic electronic eigenstates, $\Phi_n(\mathbf{R}, \mathbf{r})$. These satisfy the time-independent Schrödinger equation:

(A.4) $\hat{h}_e \Phi_n(\mathbf{R}, \mathbf{r}) = E_n(\mathbf{R})\Phi_n(\mathbf{R}, \mathbf{r})$

where the electronic Hamiltonian is

(A.5) $\hat{h}_e = \hat{T} + \hat{U}_{ee} + \hat{V}_{ne} = \hat{H} - \hat{T}_n - \hat{V}_{nn}$

Here, $\hat{T}$ is the electronic kinetic operator, $\hat{U}_{ee}$ is the electron-electron interaction, $\hat{V}_{ne}$ is the electron-nuclear interaction, $\hat{T}_n$ is the nuclear kinetic operator, and $\hat{V}_{nn}$ is the inter-nuclear interaction. This is a partial differential equation in $\mathbf{r}$ variables, so the 3P nuclear coordinates $\mathbf{R}$ enter as parameters. This expansion, which is mathematically possible, is called expansion in the adiabatic basis, because $\Phi_n(\mathbf{R},\mathbf{r})$ are solutions of the time-independent electronic Schrödinger equation, corresponding to a particular nuclear configuration. Equation (A.4) has to be solved for all nuclear configurations $\mathbf{R}$ where the nuclear wave function is non-vanishing. By replacing the above ansatz into full Schrödinger equation, we obtain:

$$\left[i\hbar\frac{\partial}{\partial t} + \sum_{I=1}^{P}\frac{\hbar^2}{2M_I}\nabla_I^2 - V_{nn} - E_q(\mathbf{R})\right]\Theta_q(\mathbf{R},t)$$

$$= -\sum_n \sum_{I=1}^{P}\frac{\hbar^2}{2M_I}\left\langle \Phi_q \middle| \nabla_I^2 \middle| \Phi_n \right\rangle \Theta_n(\mathbf{R},t) \qquad \text{(A.6)}$$

$$-2\sum_n \sum_{I=1}^{P}\frac{\hbar^2}{2M_I}\vec{\nabla}_I\Theta_n(\mathbf{R},t)\cdot\left\langle \Phi_q \middle| \vec{\nabla}_I \middle| \Phi_n \right\rangle$$

which constitutes a set of coupled partial differential equations containing off-diagonal terms. Here, the Dirac's bra-ket notation is used to indicate matrix of the type:

$$\left\langle \Phi_q \middle| \vec{\nabla}_I \middle| \Phi_n \right\rangle = \int \Phi_q^*(\mathbf{R},r)\vec{\nabla}_I\Phi_n(\mathbf{R},\mathbf{r})d\mathbf{r} \qquad \text{(A.7)}$$

So, the reduction of the full wave function to an expression of the type:

$$\Psi(\mathbf{R},\mathbf{r},t) = \sum_n \Theta_n(\mathbf{R},t)\Phi_n(\mathbf{R},r) \qquad \text{(A.8)}$$

is not completely correct, because even if the system is initially prepared in a pure state like the one above, the off-diagonal terms will mix (excite) the different electronic eigenstates along the temporal evolution. If this is the case, then the dynamics is said to be non-adiabatic. However, if the off-diagonal terms can be neglected, then an expression like (A.8) is valid because the nuclear dynamics has no means to cause electronic transitions. In this case, the dynamics is said to be adiabatic. Therefore, the necessary condition for neglecting the non-adiabatic couplings is that:

$$\left| \sum_{I=1}^{P}\frac{\hbar^2}{M_I}\left\langle \Theta_q \middle| \vec{\nabla}_I \middle| \Theta_n \right\rangle \cdot \left\langle \Phi_q \middle| \vec{\nabla}_I \middle| \Phi_n \right\rangle \right| << \left| E_q(\mathbf{R}) - E_n(\mathbf{R}) \right| \qquad \text{(A.9)}$$

or equivalently,

$$\text{(A.10)} \quad \frac{m}{M}\left|\frac{\hbar\Omega_v}{E_q(\mathbf{R})-E_n(\mathbf{R})}\right| << 1$$

where Ω_v is the maximum frequency of rotation of the electronic wave function to the nuclear motion and the energies in the denominator are the electronic adiabatic eigenstates (the energy gap if q=1 and n=0) . The mass ratio is always smaller than $5x10^{-4}$, thus satisfying the adiabatic approximation unless a very small gap occurs. ***For the case of metal, since the typical temperatures (between room temperature and few thousand degrees) are usually much lower than the electronic Fermi temperature, excitations are confined to a narrow region around the Fermi surface, and most properties are very little affected by neglecting non-adiabatic contributions due to these few electrons. In terms of energy scales, the relevant excitations in metals are at small wave numbers and are not electron hole pairs. Therefore, adiabatic approximation is still appropriate for metals despite the zero energy gap.***

A.1.2 Classical nuclei approximation

According to the adiabatic approximation, the total wave function can be written in the form of (A.8) where $\Theta_n(\mathbf{R},t)$ is the nuclear wave function. At room temperature, the thermal wavelength is $\lambda_T = (\hbar^2/2Mk_BT)^{1/2}$. Regions of space separated by more than λ_T do not exhibit quantum phase coherence. Since interatomic distances are normally of the order of 1Å, thus the total nuclear wave function can be considered as incoherent superposition of individual nuclear wave packets:

$$\text{(A.11)} \quad \Theta_n(\mathbf{R},t) = \prod_{I=1}^{P}\Theta_n^{(I)}(\mathbf{R},\mathbf{R}^I(t),t)$$

where, $\mathbf{R}^{(I)}(t)$ are the centers of the individual wave packets (the time-dependent Hartree approximation), which does not include correlations between nuclei. Exchange effects are also not included, although they could be recovered by proposing a total wave function in a form of Slater determinant leading to Hartree-Fock approximation. Also, nuclear masses are large enough that the individual nuclear wave packets are quite localized provided that the

curvature of the potential by which they move is sufficiently large. With the above, we can therefore treat atomic nuclei as classical particles. The time-dependent adiabatic equation for the nuclear wave function is:

$$\text{(A.12)}\quad i\hbar\frac{\partial\Theta_m(\mathbf{R},t)}{\partial t}=(-\sum_{I=1}^{P}\frac{\hbar^2}{2M_I}\nabla_I^2+\tilde{\varepsilon}_n(\mathbf{R}))\Theta_m(\mathbf{R},t)$$

$$\text{(A.13)}\quad \tilde{\varepsilon}_n(\mathbf{R})=\varepsilon_n(\mathbf{R})+\sum_{I=1}^{P}\frac{\hbar^2}{2M_I}\left\langle\Phi_q\left|\nabla_I^2\right|\Phi_q\right\rangle$$

The second term in this expression is a diagonal correction to the electronic energy levels due to the dependence of the electronic wavefunction on the nuclear coordinates as described previously. And when this term is neglected, the dynamics of the mean values of the position and momentum operators as obtained by Ehrenfest's theorem are :

$$\text{(A.14)}\quad i\hbar\frac{d\langle\mathbf{R}\rangle}{dt}=\left\langle[\hat{H},\mathbf{R}]\right\rangle=i\hbar\frac{\langle P\rangle}{M}\Rightarrow M\frac{d\langle\mathbf{R}\rangle}{dt}=\langle P\rangle$$

$$\text{(A.15)}\quad i\hbar\frac{d\langle P\rangle}{dt}=\left\langle[\hat{H},P]\right\rangle=-i\hbar\left\langle\nabla\varepsilon_n(\mathbf{R})\right\rangle$$

which when combined gives the following Newtonian equation of motion:

$$\text{(A.16)}\quad M\frac{d^2\langle\mathbf{R}\rangle}{dt^2}=-\left\langle\nabla\varepsilon_n(\mathbf{R})\right\rangle$$

This is valid only for mean value of the position operator. The classical nuclei approximation can identify this mean value with the Cartesian coordinates of the classical particle. This can be easily understood if the nuclear wave functions are represented as a product of Dirac's delta function whose centers are located at the classical positions. So, $\langle\mathbf{R}\rangle = \mathbf{R}_{cl}(t)$ and $\langle\nabla\varepsilon_n(\mathbf{R})\rangle = \varepsilon_n(\mathbf{R}_{cl})$. Expanding the potential to third order, the difference between the correct expression and the classical approximation is:

$$\Delta F = -[\langle \nabla \varepsilon_n(\mathbf{R}) \rangle - \nabla \varepsilon_n(\langle \mathbf{R} \rangle)]$$

$$= -\frac{1}{2}\sum_{JK}\left[\nabla\left(\frac{\partial^2 \varepsilon_n(\mathbf{R})}{\partial \mathbf{R}_J \partial \mathbf{R}_K}\right)\right]_{\mathbf{R}_{eq}} [\langle \mathbf{R}_J \mathbf{R}_K \rangle - \langle \mathbf{R}_J \rangle \langle \mathbf{R}_K \rangle] \quad \text{(A.17)}$$

The factor on the right represents the dispersion of the wave function which is small for narrow distributions and becomes strictly zero for δ-functions. Therefore, within the classical nuclei approximation, the equations of motion become:

$$M\frac{d^2\mathbf{R}_{cl}(t)}{dt^2} = -\nabla \varepsilon_n(\mathbf{R}_{cl}) \quad \text{(A.18)}$$

where $\varepsilon_n(R_{cl})$ is the nth adiabatic potential energy surface (PES), and there is one equation of motion for each different PES. The final expression for the equation of motion is achieved by using Hellman-Feynman theorem. This theorem indicates that the variation of the electronic energy with respect to an external parameter (λ) coupled to the electronic variables can be calculated as the expectation value of the variation of the Hamiltonian:

$$\frac{\partial \varepsilon_n(\lambda)}{\partial \lambda} = \left\langle \Phi_n(\mathbf{R}) \left| \frac{\partial \hat{h}_e}{\partial \lambda} \right| \Phi_n(\mathbf{R}) \right\rangle \quad \text{(A.19)}$$

and therefore for $\lambda = \mathbf{R}_I$,

$$M_I \frac{d^2\mathbf{R}_I(t)}{dt^2} = -\left\langle \Phi_n(\mathbf{R}) \left| \frac{\partial \hat{h}_e(\mathbf{R})}{\partial \mathbf{R}_I} \right| \Phi_n(\mathbf{R}) \right\rangle - \frac{\partial V_{nn}(\mathbf{R})}{\partial \mathbf{R}_I} \quad \text{(A.20)}$$

where **R** represents the classical nuclear configuration with

$$\hat{h}_e(\mathbf{R},\mathbf{r}) = -\frac{\hbar^2}{2m}\sum_{i=1}^{N}\nabla_i^2 - e^2\sum_{I=1}^{P}\sum_{i=1}^{N}\frac{Z_I}{|\mathbf{R}_I - \mathbf{r}_i|} + \frac{e^2}{2}\sum_{i=1}^{N}\sum_{j\neq i}^{N}\frac{1}{|\mathbf{r}_i - \mathbf{r}_j|} \quad \text{(A.21)}$$

and

(A.22) $$V_{nn}(\mathbf{R}) = \frac{e^2}{2}\sum_{I=1}^{P}\sum_{I\neq J}^{P}\frac{Z_I Z_J}{|\mathbf{R}_I - \mathbf{R}_J|}$$

The numerical integration of the above Newtonian equation of motion corresponds to the first principles or ab-initio molecular dynamics and $\varepsilon_n(R)$ is the first principles potential. The solution to the stationary problem $\nabla\varepsilon_n(R) = 0$ corresponds to geometry optimization. In either case, in order to obtain the $\nabla\varepsilon_n(R)$, it is necessary to solve (A.4). In this study, the $\varepsilon_n(R)$ gives the potential energy at a given nuclear coordinates, R.

A.1.3 The electronic problem

The key issue for studying and analyzing structure of matter is to solve the electronic Schrödinger equation:

(A.23) $$\hat{h}_e = -\frac{\hbar^2}{2m}\sum_{i=1}^{N}\nabla_i^2 - e^2\sum_{I=1}^{P}\sum_{i=1}^{N}\frac{Z_I}{|\mathbf{R}_I - \mathbf{r}_i|} + \frac{e}{2}\sum_{i=1}^{N}\sum_{j\neq i}^{N}\frac{1}{|\mathbf{r}_i - \mathbf{r}_j|}$$

where the first term is the kinetic energy, the second term is the electron-nuclear interaction and the third is the electronic repulsion. Because of quantum many-body problem, the wave function of many-electron system can not be treated as product of the wave functions of individual electrons. This fact results to solving equation of 3N degrees of freedom to get exact solution. These exact solutions are always numerical and the scaling of the calculations with the number of electrons prohibits treatment of most systems no matter how fast computers may become. The only way to move forward is to resort to approximations.

A.1.4 Density functional theory

Important theories prior to the modern density functional theory such as: (a) Thomas-Fermi, functional derivation (or concept of partial derivation of a function of several variables to the case of a continuum variables) and Thomas-Fermi-Dirac equations will not be tackled. Here, it would suffice to begin with knowing that the Thomas-Fermi approach is developed in the hopes

that the energy can be expressed in terms of the electronic density. This idea has the proof existed through Hohenberg and Kohn (1964) – the Hohenberg-Kohn theorems [45].

Theorem 1: The external potential is univocally determined by the electronic density, besides a trivial additive constant.

Proof: We first suppose the opposite hold holds – the external potential is not univocally determined by the density. In this case we should be able to find two potentials υ and υ' such that their ground state density ρ is the same. Let Φ and $E_0 = \langle \Phi | \hat{H} | \Phi \rangle$ be the ground state wave function and ground state energy corresponding to the Hamiltonian, $\hat{H} = \hat{T} + \hat{V}_{ext} + \hat{U}_{ee}$. Let also Φ' and $E_0' = \langle \Phi' | \hat{H'} | \Phi' \rangle$ be the ground state wave function and ground state energy of $\hat{H'} = \hat{T'} + \hat{V'}_{ext} + \hat{U'}_{ee}$. According to Rayleigh-Ritz variational principle we have:

$$(A.24)\ E_0 < \langle \Phi' | \hat{H} | \Phi' \rangle = \langle \Phi' | \hat{H}' | \Phi' \rangle + \langle \Phi' | \hat{H} - \hat{H}' | \Phi' \rangle$$
$$= E'_0 + \int \rho(\mathbf{r})[\upsilon_{ext}(\mathbf{r}) - \upsilon'_{ext}(\mathbf{r})]d\mathbf{r}$$

where we have used the fact that different Hamiltonians necessarily corresponds to different ground states Φ ≠ Φ'. This is straightforward to prove since the potential is multiplicative operator. Now we can simply exchange the roles of the Φ and Φ' ($\hat{H}$ and $\hat{H}'$), and readily obtain:

$$(A.25)\ E'_0 < \langle \Phi | \hat{H}' | \Phi \rangle = \langle \Phi | \hat{H} | \Phi \rangle + \langle \Phi | \hat{H}' - \hat{H} | \Phi \rangle$$
$$= E_0 - \int \rho(\mathbf{r})[\upsilon_{ext}(\mathbf{r}) - \upsilon'_{ext}(\mathbf{r})]d\mathbf{r}$$

and these two inequalities when added becomes $E_0 + E_0' < E_0' + E_0$, therefore there can not be $\upsilon_{ext}(\mathbf{r}) \neq \upsilon'_{ext}(\mathbf{r})$ that correspond to the same electronic density for the ground state, unless they differ from trivial additive constant.

Corollary: Since, $\rho(\mathbf{r})$ univocally determines $\upsilon_{ext}(\mathbf{r})$, it also determines the ground state wavefunction Φ, which should be obtained by solving the full many-body Schrödinger equation.

Theorem 2: Let $\tilde{\rho}(\mathbf{r})$be non-negative density normalized to N. We define the variational energy E_v, which is a functional of the density because of the previous theorem in the following way:

$$(A.26)\ E_v[\tilde{\rho}] = F[\tilde{\rho}] + \int \tilde{\rho}(\mathbf{r})\upsilon_{ext}(\mathbf{r})d\mathbf{r}$$

with

$$(A.27)\ F[\tilde{\rho}] = \left\langle \Phi[\tilde{\rho}] \middle| \hat{T} + \hat{U}_{ee} \middle| \Phi[\tilde{\rho}] \right\rangle$$

Here, $\Phi[\tilde{\rho}]$ is the ground state of a potential which has $[\tilde{\rho}]$ as its ground state density, so that $E_0 = E_v[\rho]$ verifies

$$(A.28)\ E_0 < E_v[\tilde{\rho}]$$

for any $\tilde{\rho} \neq \rho$, and is thus the ground state energy.

Proof:

$$(A.29)\ \left\langle \Phi[\tilde{\rho}] \middle| \hat{H} \middle| \Phi[\tilde{\rho}] \right\rangle = F[\tilde{\rho}] + \int \tilde{\rho}(\mathbf{r})\upsilon_{ext}(\mathbf{r})d\mathbf{r}$$

$$= E_v[\tilde{\rho}] \geq E_v[\rho] = E_0 = \left\langle \Phi[\rho] \middle| \hat{H} \middle| \Phi[\rho] \right\rangle$$

The inequality follows from Rayleigh-Ritz's variational principle for the wavefunction, but applied to electronic density. Therefore, the variational principle states that:

$$(A.30)\ \delta\left\{ E_v[\rho] - \mu\left(\int \rho(\mathbf{r})d\mathbf{r} - N\right)\right\} = 0$$

which leads to generalization of the Thomas-Fermi equation:

$$\text{(A.31)}\quad \mu = \frac{\delta E_v[\rho]}{\delta \rho} = \upsilon_{ext}(\mathbf{r}) + \frac{\delta F[\rho]}{\delta \rho}$$

The knowledge of $F[\rho]$ implies the knowledge of solution of the full many-body Schrödinger equation. $F[\rho]$ is a universal functional, which does not depend explicitly on the external potential but on the electronic density. In the Hohenberg-Kohn formulation, $F[\rho] = \langle \Phi | \hat{T} + \widehat{U_{ee}} | \Phi \rangle$ where Φ is the ground state many-body wave function. These two theorems form the basis of density functional theory (DFT).

In the Hohenberg-Kohn theorem, the electronic density determines the external potential. However, it is also required that the density corresponds to some ground state antisymmetric wave function, which may not be the case for some trial densities, $\tilde{\rho}$. In fact, unacceptable densities can be obtained from variational principle if not done carefully. Levy (1982) [46] reformulated DFT in such a way that the antisymmetric origin of the density is guaranteed. Levy used the constrained search method by redefining the $F[\rho]$ in the following:

$$\text{(A.32)}\quad F[\rho] = \min_{\Phi \to \rho} \left\langle \Phi \middle| \hat{T} + \hat{U}_{ee} \middle| \Phi \right\rangle$$

where the ρ is any non-negative density such that:

$$\text{(A.33)}\quad \int \rho(\mathbf{r}) d\mathbf{r} = N \text{ and } \int \left| \nabla \rho^{1/2}(\mathbf{r}) \right|^2 d\mathbf{r} < \infty$$

with the additional constraint that the density should arise from an antisymmetric wave function. The search is thus constrained to the subspace of all the antisymmetric Φ that gives rise to the same density ρ, avoiding unphysical densities.

A.1.5 The Kohn-Sham equations

It was argued previously that a good strategy is to separate the classical electrostatic energy (Hartree term) from the exchange correlation contributions.

This strategy is useful since it divides the generally unknown electron-electron interaction energy into pieces of decreasing importance from energetic point of view: Hartree, exchange, correlation. More importantly, the Hartree term, which is by far the largest contribution, is just the classical electrostatic energy, which is known exactly. The second largest, exchange term, is also well-known and in principle can be calculated exactly as in Hartree-Fock theory. For practical reasons (computational expense) this term is most often approximated. Consequently, all the ignorance about the electronic many body problem is displaced to the smallest contribution, correlation term. Here, it would suffice to mention that reasonably good approximations already exist for large class of systems. So the main problem at this stage is with the kinetic energy $T = \langle \Phi | \hat{T} | \Phi \rangle$ since its explicit expression from the electron density is not known. In fact, the exact calculation requires the knowledge of Laplacian of the one-body density matrix, which is not related to the density in an obvious manner. The Thomas-Fermi expression is local in the density, which is a severe limitation because this model does not hold bound states and also the atomic shell structure is absent. The main problem here is that the kinetic energy operator is inherently non-local. This can be easily seen by considering the first order finite difference expression of the Laplacian of a function f in a discrete one –dimensional grid.

$$\text{(A.34)} \quad \left(\nabla^2 f\right)_{x_i} = \frac{f(x_{i+1}) + (fx_{i-1}) - 2f(x_i)}{\Delta^2}$$

Where $\{x_i\}$ and Δ are the grid points and spacing between them, respectively. Expressions that extend beyond nearest neighbors are available and show that contributions from distant neighbors becomes increasingly smaller which tells us that kinetic energy operator, although non-local, is quite "near-sighted". Hence, semi-local gradient expansions work reasonably well. A general approach is suggested by Kohn and Sham (1965) [47]. It starts from the observation that a system of non-interacting electrons is exactly described by an anti-symmetric wave function of the Slater determinant type, made of one-electron orbitals. As in Hartree-Fock theory, for such a wave function, the kinetic energy can be obtained in terms of the one-electron orbitals. In this case, the ground state density matrix $\rho_1(\mathbf{r}, \mathbf{r}')$ is expressed by:

(A.35) $\rho_1(\mathbf{r},\mathbf{r}') = \sum_{i=1}^{\infty} f_i \varphi_i(\mathbf{r}) \varphi_i^*(\mathbf{r}')$

where $\varphi_i(\mathbf{r})$ are the one electron orbitals and f_i are the occupation numbers corresponding to these orbitals. Then, the expression for the kinetic energy of non-interacting electrons is

(A.36) $T = \frac{\hbar^2}{2m} \sum_{i=1}^{\infty} f_i \left\langle \varphi_i \middle| \nabla^2 \middle| \varphi_i \right\rangle$

The Kohn and Sham's idea was that, if one can find a system of non-interacting electrons that produces the same electronic density of the interacting systems, then the kinetic energy of the non-interacting system can be calculated from the above expression (of course – not the exact kinetic energy of interacting system). There is then a correlation contribution to the kinetic energy that is not taken into account, which must be included in the correlation energy term. In the following, the non-interacting electrons whose groundstate density coincides with that of the interacting system, which is termed as non-interacting reference system of density $\rho(\mathbf{r})$, is described by the Hamiltonian

(A.37) $\hat{H}_R = \sum_{i=1}^{N} \left[-\frac{\hbar^2}{2m} \nabla_i^2 + \upsilon_R(\mathbf{r}_i) \right],$

with N, the number of electrons and the $\upsilon_R(\boldsymbol{r}_i)$ is the reference potential where the ground state density of $\hat{H}_R$ equals the $\rho(\mathbf{r})$. This ensures that the ground state energy equals the energy of the interacting system. The Hamiltonian above has no electron-electron interactions. Therefore, the eigenstates can be expressed in the form of Slater determinants

(A.38) $\Phi(\boldsymbol{r}) = \frac{1}{\sqrt{N_s!}} SD[\varphi_1(\boldsymbol{r})\varphi_2(\boldsymbol{r}_2) \ldots \varphi_{N_s}(\boldsymbol{r}_{N_s})]$

where the closed shell situation is chosen (i.e. occupation numbers are 2 for $i \leq N_s$ and 0 for $i \geq N_s$ with $N_s = N/2$ the number of doubly occupied orbitals. For the meantime, the spin dependence is ignored. Therefore, the density is:

(A.39) $\rho(\mathbf{r}) = 2\sum_{i=1}^{N_s} |\varphi_i(\mathbf{r})|^2$

and the kinetic term is:

(A.40) $T_R[\rho] = -\frac{\hbar^2}{m}\sum_{i=1}^{N_s} \langle \varphi_i | \nabla^2 | \varphi_i \rangle$

The single particle orbitals φ_i are the N_s lowest-energy eigenfunctions of the one-electron Hamiltonian

(A.41) $\hat{H}_{KS} = -\frac{\hbar^2}{2m}\nabla^2 + \upsilon_R(\mathbf{r}),$

which are obtained by solving the one-electron Schrödinger equation:

(A.42) $\hat{H}_{KS}\varphi_i(\mathbf{r}) = \varepsilon_i\varphi_i(\mathbf{r})$

Using the $T_R[\rho]$, the universal density functional can be re-written in the following form:

(A.43) $F[\rho] = T_R[\rho] + \frac{1}{2}\iint \frac{\rho(\mathbf{r})\rho(\mathbf{r}')}{|\mathbf{r}-\mathbf{r}'|} d\mathbf{r}\, d\mathbf{r}' + \tilde{E}_{xc}[\rho]$

This defines the modified exchange and correlation energy $\tilde{E}_{xc}[\rho]$, that it accounts also for the kinetic correlation ignored in $T_R[\rho]$. By substituting this expression into the total energy functional:$E_v[\rho] = F[\rho] + \int \rho(\boldsymbol{r})\upsilon_{ext}(\boldsymbol{r})d\boldsymbol{r}$, we can obtain the KS functional:

(A.44) $E_{KS}[\rho] = T_R[\rho] + \int \rho(\mathbf{r})\upsilon_{ext}(\mathbf{r})d\mathbf{r} + \frac{1}{2}\iint \frac{\rho(\mathbf{r})\rho(\mathbf{r}')}{|\mathbf{r}-\mathbf{r}'|} d\mathbf{r}\, d\mathbf{r}' + \tilde{E}_{XC}[\rho]$

Here, the energy functional is expressed in terms of the N_S orbitals that minimize the non-interacting electronic kinetic energy under the fixed density constraint. The one-electron orbitals are usually called Kohn-Sham orbitals.

The Kohn-Sham orbitals are actually the result of mathematical construction devised in order to simplify the problem. In principle, they do not have obvious meaning by themselves, but they are used to construct the density according to (A.39). In practice, however, it is customary to think of them as single particle physical eigenstates. The Kohn-Sham orbitals satisfy the one-electron KS equations (A.42), but so far, the reference potential, υ_R (or also called Kohn-Sham potential, υ_{KS}) is not known. What is, however, known is that υ_R is the potential that ensures that the density of the non-interacting reference system is the same as the true density of the interacting system. This is possible to determine by minimizing the KS functional (A.44) with respect to the density, under the constraint that this density integrates to N particles. The variational principle applied to Kohn-Sham's functional is:

$$\text{(A.45)}\quad \frac{\delta}{\delta\rho(\mathbf{r})}\left(E_{KS}[\rho]-\mu\int\rho(\mathbf{r})d\mathbf{r}\right)=0$$

Using the rules of functional derivation, the following equation for minimizing ground state density can be obtained:

$$\text{(A.46)}\quad \frac{\delta T_R[\rho]}{\delta\rho(\mathbf{r})}+\upsilon_{ext}(\mathbf{r})+\int\frac{\rho(\mathbf{r}')}{|\mathbf{r}-\mathbf{r}'|}d\mathbf{r}'+\frac{\delta\tilde{E}_{XC}[\rho]}{\delta\rho(\mathbf{r})}=\mu$$

The first functional derivative can be obtained by considering the non-interacting Hamiltonian in (A.37). Since the particles in the reference system only interact with the reference potential, and not between themselves, this Hamiltonian corresponds to:

$$\text{(A.47)}\quad E_{\upsilon_R}[\tilde{\rho}]=T_R[\tilde{\rho}]+\int\tilde{\rho}(\mathbf{r})\upsilon_R(\mathbf{r})d\mathbf{r}$$

whose ground state energy is the same as that of the interacting system because they share the same electronic density. Therefore, in general, $E_{\upsilon_R}[\tilde{\rho}]\geq E_0$ and the equality is verified only for the ground state density, ρ. This means that the functional derivative of $E_{\upsilon_R}[\tilde{\rho}]$ must vanish for the ground state density. Applying the variational principle (A.45) to $E_{\upsilon_R}[\tilde{\rho}]$, we obtain:

(A.48) $$\frac{\delta T_R[\rho]}{\delta\rho(\mathbf{r})}+\upsilon_R(\mathbf{r})=\mu_R$$

where μ_R is the chemical potential of the non-interacting system, which should coincide with that of the interacting system, μ. Using (A.46) and (A.48), we get:

(A.49) $$\upsilon_R(\mathbf{r})=\upsilon_{ext}(\mathbf{r})+\int\frac{\rho(\mathbf{r}')}{|\mathbf{r}-\mathbf{r}'|}d\mathbf{r}'+\mu_{XC}[\rho](\mathbf{r}),$$

where $$\mu_{XC}[\rho](\mathbf{r})=\frac{\delta\tilde{E}_{XC}[\rho]}{\delta\rho(\mathbf{r})}$$

As in Hartree and Hartree-Fock theories, the reference potential depends on the solutions of the one-electron Schrödinger equation (the KS orbitals) through the electronic density. Therefore, this equation must be solved self-consistently, making sure that the density used to construct the reference potential coincides with that obtained from the solutions of the equation via (A.39).

The computation of the approximate solution to the many-body Schrödinger equation within DFT by solving the Kohn-Sham equations, are implemented in Vienna ab initio Simulation Package (VASP) [99-102]. VASP performs an excellent minimization scheme - an iterative solution of the generalized Kohn-Sham equations via unconstrained minimization of the norm of the residual vector to each eigenstate. It optimizes routines for charge and spin-density mixing. The rest of the robust and fast algorithms used in VASP can be found in www.vasp.at [103]. Moreover, in the VASP implementation, one should invoke either pseudopotentials or projector augmented wave method for electron-ion interaction; plane wave basis sets; and LDA or GGA-level of exchange and correlation. These methods and parameters are discussed in latter sections.

A.1.6 Spin density functional theory

Because in the present study, the target systems have partially filled outer shell then the integration of spin component in DFT is worth-mentioning. This section also serves the basis of the constrained DFT which is introduced

appropriately in section 2.3.1. Extending the Kohn-Sham theory to spin-polarized systems requires two independent spin densities, $\rho = \rho_\uparrow + \rho_\downarrow$. Kohn-Sham spin orbitals are constructed to satisfy the self-consistent Kohn-Sham equations:

$$\text{(A.50)} \quad \left\{-\frac{\hbar^2}{2m}\nabla^2 + \upsilon_{R,s}(\mathbf{r})\right\}\varphi_{i,s}(\mathbf{r}) = \varepsilon_{i,s}\varphi_{i,s}(\mathbf{r})$$

where the subindex s indicates the spin component. The reference potentials $\upsilon_{R,s}(\mathbf{r})$ are obtained as an extension to (A.49) to the spin-dependent case:

$$\text{(A.51)} \quad \upsilon_{R,s}(\mathbf{r}) = \upsilon_{ext}(\mathbf{r}) + \int \frac{\rho(\mathbf{r}')}{|\mathbf{r}-\mathbf{r}'|}d\mathbf{r}' + \mu_{XC,s}[\rho_\uparrow, \rho_\downarrow](\mathbf{r}),$$

with

$$\text{(A.52)} \quad \mu_{XC,s}[\rho_\uparrow, \rho_\downarrow](\mathbf{r}) = \frac{\delta \tilde{E}_{XC}[\rho_\uparrow, \rho_\downarrow]}{\delta \rho_s(\mathbf{r})}$$

where

$$\text{(A.53)} \quad \rho_s(\mathbf{r}) = \sum_{i=1}^{N_s} |\varphi_{i,s}(\mathbf{r})|^2$$

Generally, the exchange-correlation functionals are given in terms of the total electronic density, ρ and the magnetization density ς, where $\rho = \rho_\uparrow + \rho_\downarrow$ and $(\boldsymbol{r}) = \rho_\uparrow + \rho_\downarrow$. The density given by the $\rho(\mathbf{r})$ and $\rho_s(\mathbf{r})$ involves two different number of electrons, $N_\uparrow$ and $N_\downarrow$ such that the sum, $N = N_\uparrow + N_\downarrow$ is the total number of electrons in the system. Also, it is not necessary that $N_\uparrow = N_\downarrow$. The values of N_s have to be determined according to single-particle eigenvalues by asking for the lowest N to be occupied. This defines the Fermi energy ε_F such that the occupied states have $\varepsilon_{i,s} < \varepsilon_F$. This approach is known as spin density functional theory (SDFT). In the case of non-spinpolarized systems $\rho_\downarrow(\boldsymbol{r}) = \rho_\uparrow(\boldsymbol{r})$, SDFT reduces to the double occupancy of single particle orbitals. In SDFT, the total energy is

(A.54)

$$E_{KS}[\rho_\downarrow, \rho_\uparrow] = T_R[\rho_\downarrow, \rho_\uparrow] + \int \rho(\mathbf{r})\upsilon_{ext}(\mathbf{r})d\mathbf{r} + \frac{1}{2}\iint \frac{\rho(\mathbf{r})\rho(\mathbf{r}')}{|\mathbf{r}-\mathbf{r}'|}d\mathbf{r}\,d\mathbf{r}' + \tilde{E}_{XC}[\rho_\downarrow, \rho_\uparrow]$$

with

$$T_R[\rho_\downarrow,\rho_\uparrow]=-\frac{\hbar^2}{2m}\sum_{s=1}^{2}\sum_{i=1}^{N_s}\left\langle\varphi_{i,s}\left|\nabla^2\right|\varphi_{i,s}\right\rangle \quad \text{(A.55)}$$

In fact, the solution of the KS equations must be obtained by an iterative procedure in the same way as for the Hartree and Hartree-Fock equations. In these latter methods, the total energy can not be simply written as the sum of the eigenvalues, $\varepsilon_{i,s}$. Double counting has to be subtracted:

(A.56)

$$E_{KS}[\rho_\downarrow,\rho_\uparrow]=\sum_{s=1}^{2}\sum_{i=1}^{N_s}\varepsilon_{i,s}-\frac{1}{2}\iint\frac{\rho(\mathbf{r})\rho(\mathbf{r}')}{|\mathbf{r}-\mathbf{r}'|}d\mathbf{r}\,d\mathbf{r}'+\{\tilde{E}_{XC}[\rho_\downarrow,\rho_\uparrow]-\int\rho(\mathbf{r})\mu_{XC}[\rho_\downarrow,\rho_\uparrow](\mathbf{r})d\mathbf{r}\}$$

and a similar expression for the unpolarized case, where the sum over spin components is replaced by a factor of 2, and the spin-polarized expression for the exchange-correlation potential are replaced by the unpolarized one. SDFT assumes that the projection of the total spin of the system is a good quantum number. There are cases, however, when this is not the case. Non-collinear magnetism can appear in disordered or low-symmetry structures, and also in the form of spiral phases such as Fe clusters. The theory of non-collinear magnetism developed by Von Barth and Hedin (1972) [104], is based on a 2x2 spinor of the spin density:

$$\rho_{\alpha\beta}(\mathbf{r})=\frac{1}{2}\rho(\mathbf{r})\delta_{\alpha\beta}+\frac{1}{2}\sum_{i=1}^{3}\zeta_i(\mathbf{r})\sigma^i_{\alpha\beta} \quad \text{(A.57)}$$

where $\sigma^i_{\alpha\beta}$ are the Pauli Spin matrices and $\zeta_i(\boldsymbol{r})$ are the Cartesian components of the spin polarization vectors. The recent method of treating non-collinear magnetism is developed by Dederich et. al. [67] based on DFT and will be discussed in the next chapter.

A.1.7 Exchange-correlation in DFT

The idea here is to look for approximation to exchange and correlation where

both terms are treated in similar manner. One starting point is to consider homogenous electron gas – a simplified model for the metallic system. The exchange energy is given by Dirac's expression:

$$\text{(A.58)}\quad \varepsilon_X^D[\rho] = -\frac{3}{4}\left(\frac{3}{\pi}\right)^{1/3}\rho^{1/3} = -\frac{3}{4}\left(\frac{9}{4\pi^2}\right)^{1/3}\frac{1}{r_s} = -\frac{0.458}{r_s}a.u.$$

where $r_s = (3/4\pi\rho)^{1/3}$ is the mean inter-electronic distance expressed in atomic units (1 bohr=0.529177 Angstrom). But eventually, using homogenous electron gas as a reference is not entirely a good idea for molecular systems as their electronic densities are far from uniform. The first idea to address this issue is to consider a general inhomogenous electronic system as locally homogenous, and then to use the exchange correlation hole corresponding to the homogenous electron gas, which is known to some good accuracy. This is the local density approximation (LDA). Here, we discuss the exchange-correlation correction, which is also strongly based on LDA. This exchange-correlation treatment is what is used in this study.

To address the issue of inhomogeneity in the electronic density, the natural way is to carry out an expansion of the density in terms of the gradient and higher order derivatives. In general, the exchange-correlation energy can be written in the following form:

$$\text{(A.59)}\quad E_{XC}[\rho] = \int \rho(\mathbf{r})\varepsilon_{XC}[\rho(\mathbf{r})]F_{XC}[\rho(\mathbf{r}),\nabla\rho(\mathbf{r}),\nabla^2\rho(\mathbf{r}),...]d\mathbf{r}$$

where F_{XC} is an enhancement factor that modifies the LDA expression according to the variation of the density in the vicinity of the considered point. The second order gradient expansion of the exchange energy introduces a term proportional to the squared gradient of the density. If the expansion is further carried on to the fourth order, the term also appears proportional to the square of the Laplacian of the density. The fourth order gradient expansion of the exchange enhancement factor F_X is

(A.60) $$F_X(p,q) = 1 + \frac{10}{81}p + \frac{146}{2025}q^2 - \frac{73}{405}qp + Dp^2 + O(\nabla p^6)$$

where

(A.61) $p = \dfrac{|\nabla\rho|^2}{4(3\pi^2)^{2/3}\rho^{8/3}}$ is the square of the density gradient and ,

(A.62) $q = \dfrac{\nabla^2\rho}{4(3\pi^2)^{2/3}\rho^{5/3}}$ is the Laplacian of the density.

The first two coefficients of the expansion are exactly known. The third one is the result of a many-body calculation and has only been estimated numerically by Svendsen and von Barth, 1996 [105], to an accuracy of the order of 20%. The fourth coefficient D has not been explicitly calculated to date but the best numerical estimate is zero.

The second order gradient expansion corresponds to an expression of the type:

(A.63) $$E_{XC}[\rho] = \int A_{XC}[\rho]\rho(\mathbf{r})^{4/3}d\mathbf{r} + \int C_{XC}[\rho]|\nabla\rho(\mathbf{r})|^2/\rho(\mathbf{r})^{4/3}d\mathbf{r}$$

which is asymptotically valid for densities that vary slowly in space. The LDA retains only the leading term. It is well-known that a straightforward evaluation of the above is ill-behaved. Other issues are violations of one or more exact conditions required for the exchange and correlation holes, such as normalization conditions , negativity of exchange density and self-interaction cancellation. Perdew showed that imposing these conditions to functionals that originally do not verify them, results in remarkable improvement of the quality of the exchange energies (Perdew, 1985) [50]. On the basis of this type of reasoning, a number of modified gradient expansions have been proposed mainly between 1986 to 1996 which are named generalized gradient approximations (GGA). ***GGA is then obtained using two major approaches: deriving appropriate expressions by theoretical methods and then requesting that the coefficients are such that a number of the formal conditions are met. Most conditions for the XC hole described above are met by***

Perdew-Burke-Ernzerhof functional [51] in addition to absence of fitting parameters, therefore, this GGA-functional is used in the DFT calculations.

A.2 Electronic structure calculation

The main issue in electronic structure theory at the single particle approximation level is to self-consistently solve a set of N coupled, partial differential equations. Below summarizes the treatment of electron-nuclear interaction and the mathematical representation of single-particle orbitals.

A.2.1 KS and HF equations

In the KS formulation we have to solve the following eigenvalue equation:

$$\text{(A.64)}\quad \left\{-\frac{\hbar^2}{2m}\nabla^2+\upsilon_{ext}(\mathbf{r})+\int\frac{\rho(\mathbf{r}')}{|\mathbf{r}-\mathbf{r}'|}d\mathbf{r}'+\mu_{XC}[\rho]\right\}\varphi_i(\mathbf{r})=\varepsilon_i\varphi_i(\mathbf{r})$$

where the electron density ρ is :

$$\text{(A.65)}\quad \rho(\mathbf{r})=\sum_{i=1}^{N}f_i|\varphi_i(\mathbf{r})|^2$$

where N is the number of electrons and f_i are the occupation numbers corresponding to the one-electron eigenstates. In the case of spin-unpolarized insulators or closed shell molecules, $f_i=2$ for the $N/2$ lowest eigenstates and $f_i=0$, otherwise. For spin-polarized systems or open-shell molecules, the exchange correlation potential and the external potential, when there are external magnetic fields, depends on the spin projection. So there are two sets of occupation numbers, one for each spin-component. The occupation numbers are $f_{i\sigma}=1$ for the N lowest eigenstates, but considering both sets of eigenvalues, $\varepsilon_{i\uparrow}$ and $\varepsilon_{i\downarrow}$. It may well happen that the number of occupied states is unbalanced. The external potential $\upsilon_{ext}(\mathbf{r})$ represents the interaction between the electrons and the nuclei and is given by:

(A.66) $$\upsilon_{ext}(\mathbf{r}) = -e^2 \sum_{I=1}^{P} \frac{Z_I}{|\mathbf{r} - \mathbf{R}_I|}$$

and the exchange-correlation potential μ_{XC} are given by any of the expressions described previously. At this point, the solution of KS equation requires:

(1) finding mathematical way to represent the single particle orbitals

(2) treating electron-nuclear interactions

A.2.2 Basis set

The basis set is a mathematical representation for the one-electron orbitals. A possibility is certainly to represent them on a three-dimensional grid in real space, and to solve the partial differential equations using finite differences. The one-electron wave function can be expanded in a generic basis set described by the orbitals $|\varphi_\alpha\rangle$. In real-space representation these orbitals become $\langle \boldsymbol{r}|\varphi_\alpha\rangle = \varphi_\alpha(\boldsymbol{r})$. The KS or HF orbitals are then written as linear combination of these basis orbitals:

(A.67) $$\varphi_j(\mathbf{r}) = \sum_{\alpha=1}^{M} c_{j\alpha}\phi_\alpha(\mathbf{r})$$

where j labels the wave function or band, the sum runs over all the basis functions up to the dimension of the basis set M, and $c_{j\alpha}$ are the expansion coefficients of wave function j. The wave functions are solutions of the time-independent Schrödinger equation. We note that atomic systems have spherical symmetry, and the wave functions are usually obtained by integrating the radial Schrödinger equation numerically using finite differences, forward from the origin and backward from infinity, and requesting that the two solutions match in amplitude and derivative at a pre-fixed radius. Those energies that allow for a smooth matching of inward and outward solutions are precisely the eigenvalues. If this procedure is to be generalized to a polyatomic system, continuity conditions have to be imposed at the surface of the spheres centered on each one of the atoms. There are two additional complications arising from this, first since the geometry is not any more spherical, the

continuity conditions have to be secured at every point in the surface of the sphere, and they will in general depend on the polar and azimuthal angles. Therefore this problem requires an expansion in partial waves {in components of the wave functions for each angular momentum (l,m)}. This can be done by expanding in spherical harmonics around each atom site. Second the continuity conditions have to be verified simultaneously on the surface of all the spheres, and not just a single one. This procedure has been implemented in some programs: Slater's APW approach (Slater, 1937) [106] and LCMTO method (Andersen, 1971) [107]. Another possibility is to represent the one-electron wave functions in an energy-dependent basis set, where the basis functions are chosen according either to simplicity, to flexibility or to efficiency. In this case, the Schrödinger equation becomes a generalized linear eigenvalue problem:

$$\text{(A.68)}\quad \sum_{\beta=1}^{M}(H_{\alpha\beta}-\varepsilon_j S_{\alpha\beta})c_{j\beta}=0$$

or in condensed notation,

$$\text{(A.69)}\quad \mathbf{Hc}=\Lambda\mathbf{Sc}$$

where Λ is the diagonal matrix of the eigenvalues, matrix **c** has the eigenvectors (the expansion coefficients of the wave functions) as columns, and **H** and **S** are the energy-independent Hamiltonian and overlap matrices, respectively. The Hamiltonian matrix elements between two basis orbitals are:

$$\text{(A.70)}\quad H_{\alpha\beta}=\left\langle\phi_\alpha\middle|\hat{H}\middle|\phi_\beta\right\rangle=\int\phi_\alpha^*(\mathbf{r})H\phi_\beta(\mathbf{r})d\mathbf{r}$$

while the overlap matrix elements:

$$\text{(A.71)}\quad S_{\alpha\beta}=\left\langle\phi_\alpha\middle|\phi_\beta\right\rangle=\int\phi_\alpha^*(\mathbf{r})\phi_\beta(\mathbf{r})d\mathbf{r}$$

A.2.3 Periodic system

When studying periodic systems such as solids (bulk, surfaces) it has to be ensured that Bloch's theorem is verified, in the sense that the combination of

basis orbitals that represents a solution of the Schrödinger equation verifies the translational periodicity of the supercell. In that case, the previous expression (A.67) has to be modified the following way:

$$\text{(A.72)}\quad \varphi_j^{(k)}(\mathbf{r}) = e^{i\mathbf{k}\cdot\mathbf{r}} \sum_{\alpha=1}^{M} c_{j\alpha}^{(\mathbf{k})} \phi_\alpha(\mathbf{r}) = \sum_{\alpha=1}^{M} c_{j\alpha}^{(\mathbf{k})} \phi_\alpha^{(\mathbf{k})}(\mathbf{r})$$

where **k** indicates the wave vector in the Brillouin zone, and the modified basis functions are

$$\text{(A.73)}\quad \phi_\alpha^{(\mathbf{k})}(\mathbf{r}) = e^{i\mathbf{k}\cdot\mathbf{r}} \phi_\alpha(\mathbf{r})$$

For basis functions that respect the periodicity of the crystal, the Hamiltonian and overlap matrix elements between two basis orbitals are given by:

$$\text{(A.74)}\quad \hat{H}_{\alpha\beta}^{(k)} = \left\langle \phi_\alpha^{(\mathbf{k})} \middle| \hat{H} \middle| \phi_\beta^{(\mathbf{k})} \right\rangle = \int \phi_\alpha^{*k}(\mathbf{r}) \hat{H} \phi_\beta^{(\mathbf{k})}(\mathbf{r}) d\mathbf{r}$$

and

$$\text{(A.75)}\quad S_{\alpha\beta} = \left\langle \phi_\alpha \middle| \phi_\beta \right\rangle = \int \phi_\alpha^{*(\mathbf{k})}(\mathbf{r}) \phi_\beta^{(\mathbf{k})}(\mathbf{r}) d\mathbf{r} = \int \phi_\alpha^{*}(\mathbf{r}) \phi_\beta(\mathbf{r}) d\mathbf{r}$$

respectively. Notice that in this case the overlap matrix elements do not depend on the wave vector **k.**

For solids and in general condensed phases, Bloch's theorem prescribes that the wave functions must be composed of a phase factor and a periodic part that verifies $\mu_k(r) = \mu_k(r + \mathbf{a}_i)$ with $\mathbf{a}_i$ any lattice vector. This can be used to introduce naturally (for solid state applications) the basis set of plane waves (PW). PWs are solutions of the Schrödinger equation in the presence of constant external potential, as is approximately verified in interstitial regions in condensed phases. Closer to the atomic nuclei however, the external potential is far from constant and, hence, the solution is no longer single PW but a linear combination of PWs. In general, any function in real space can be written as

the Fourier transform of a function in reciprocal space:

$$\text{(A.76)}\quad \mu_k(r) = \int e^{i\mathbf{g}\cdot\mathbf{r}} \tilde{\mu}_k(\mathbf{g}) d\mathbf{g}$$

but due to the periodicity of $\mu_k(r)$, the only allowed values of $\mathbf{g}$ are those that verify $e^{i\boldsymbol{g}\cdot\boldsymbol{a}_j} = 1$, $\boldsymbol{g}\cdot\boldsymbol{a}_j = 2n\pi$ for $j = 1,2,3$. This implies that $\mathbf{g} = n_1\mathbf{b}_1 + n_2\mathbf{b}_2 + n_3\mathbf{b}_3$ where:

$$\text{(A.77)}\quad \mathbf{b}_i = 2\pi \frac{\mathbf{a}_j x \mathbf{a}_k}{\Omega}$$

and $\mathbf{n} = (n_1, n_2, n_3)$ is a vector of integer numbers. Therefore, the $\mathbf{g}$ vectors in the Fourier transform (A.76) are restricted precisely to the reciprocal lattice vectors $\mathbf{G}$ and the general expression for the wave function is:

$$\text{(A.78)}\quad \varphi^k(\mathbf{r}) = \frac{e^{i\mathbf{k}\cdot\mathbf{r}}}{\sqrt{\Omega}} \sum_{G=0}^{\infty} C_{\mathbf{k}}(\mathbf{G}) e^{i\mathbf{G}\cdot\mathbf{r}}$$

Hence, due to periodicity, the Fourier transform (A.76) becomes Fourier series, where the Fourier coefficients are $C_{\mathbf{k}}(\mathbf{G})$. This restriction of the possible values of $\mathbf{g}$ to the reciprocal lattice vectors ensures that periodic boundary condition (PBC) are automatically verified. We now define the PW basis functions:

$$\text{(A.79)}\quad \phi_{\mathbf{G}}(\mathbf{r}) = \frac{1}{\sqrt{\Omega}} e^{i\mathbf{G}\cdot\mathbf{r}}$$

which are suitably normalized in the supercell

$$\text{(A.80)}\quad \langle \phi_{\mathbf{G}} | \phi'_{\mathbf{G}} \rangle = \frac{1}{\Omega} \int_{\Omega} e^{i(\mathbf{G}-\mathbf{G}')\cdot\mathbf{r}} d\mathbf{r} = \frac{1}{\Omega}(\Omega \delta_{\mathbf{G},\mathbf{G}'}) = \delta_{\mathbf{G},\mathbf{G}'}$$

so that PWs corresponding to different wave vectors, $\mathbf{G} \neq \mathbf{G}'$ are orthogonal. With this definition, the wave functions for different eigenstates, j can be written as

$$\text{(A.81)}\quad \varphi_j^{(\mathbf{k})}(\mathbf{r}) = e^{i\mathbf{k}\cdot\mathbf{r}} \sum_{G=0}^{\infty} C_{j\mathbf{k}}(\mathbf{G}) \phi_{\mathbf{G}}(\mathbf{r})$$

Notice that the phase factor, $e^{i\mathbf{k}\cdot\mathbf{r}}$ involves a wave vector **k** in the first BZ, while the recripocal lattice vectors **G** entering the PW expansion, except for **G**=0, lie always outside the BZ. Wave functions corresponding to different **k** vectors obey separate Schrödinger equations. In the case of non-interacting electrons these are completely independent, but in the case of DFT (or any other many-body theory), the equations couple in the sense of self-consistency through the one-electron orbitals and the electronic density. The phase factor can be incorporated into the definition of the basis functions which will become dependent on the particular point in the BZ:

$$\text{(A.82)}\quad \phi_G^k(\mathbf{r}) = \frac{1}{\sqrt{\Omega}} e^{i(\mathbf{k}+\mathbf{G})\cdot\mathbf{r}}$$

so that

$$\text{(A.83)}\quad \varphi_j^{\mathbf{k}}(\mathbf{r}) = \sum_{G=0}^{\infty} C_{j\mathbf{k}}(\mathbf{G}) \phi_{\mathbf{G}}^{\mathbf{k}}(\mathbf{r})$$

assumes the usual form of a basis set expansion (67). Conversely, the PW coefficients assume the following form in terms of the real-space wave function:

$$\text{(A.84)}\quad C_{j\mathbf{k}}(\mathbf{G}) = \int_{\Omega} \phi_{\mathbf{G}}^{\mathbf{k}*}(\mathbf{r}) \varphi_j^{(\mathbf{k})}(\mathbf{r}) d\mathbf{r} = \frac{1}{\sqrt{\Omega}} \int_{\Omega} e^{-i(\mathbf{k}+\mathbf{G})\cdot\mathbf{r}} \varphi_j^{(\mathbf{k})}(\mathbf{r}) d\mathbf{r}$$

The kinetic and potential contributions to the Hamiltonian matrix elements $H_{G,G'}^k = T_{G,G'}^k + V_{G,G'}^k$ are then given by:

$$\text{(A.85)}\quad T_{\mathbf{G},\mathbf{G}'}^k = -\frac{\hbar^2}{2m} \left\langle \phi_{\mathbf{G}}^k \middle| \nabla^2 \middle| \phi_{\mathbf{G}'}^k \right\rangle = \frac{\hbar^2}{2m} |\mathbf{k}+\mathbf{G}|^2 \delta_{\mathbf{G},\mathbf{G}'}$$

and

(A.86) $V_{\mathbf{G},\mathbf{G}'} = \left\langle \phi_{\mathbf{G}}^{k} \middle| \hat{V} \middle| \phi_{\mathbf{G}'}^{k} \right\rangle = \frac{1}{\Omega} \int V(\mathbf{r}) e^{-i(\mathbf{G}-\mathbf{G}')\cdot\mathbf{r}} \, d\mathbf{r} = \tilde{V}(\mathbf{G}-\mathbf{G}')$

where $\tilde{V}(\boldsymbol{G}-\boldsymbol{G}')$ is the Fourier transform of the potential and, if $\hat{V}$ is a local potential, the matrix elements are independent of the wave vector **k** in the BZ. The kinetic term is, quite conveniently, diagonal in reciprocal space. Therefore in the PW basis set the time independent Schrödinger equation (68) becomes the eigenvalue equation.

(A.87) $\sum_{\mathbf{G}'} \left(\frac{\hbar^2}{2m} |\mathbf{k}+\mathbf{G}|^2 \delta_{\mathbf{G},\mathbf{G}'} + \tilde{V}(\mathbf{G}-\mathbf{G}') \right) C_{j\mathbf{k}}(\mathbf{G}') = \varepsilon_{j\mathbf{k}} C_{j\mathbf{k}}(\mathbf{G})$

Next, the Bloch's theorem implies that the wave function of an electron in a periodic potential can be naturally expanded in a plane-wave basis set. The **G** vectors allowed in the PW expansion are the reciprocal lattice vectors and in principle, an infinite number of such vectors is required to represent the wave functions with infinite accuracy. ***In practice, however, the Fourier coefficients*** $C_{\mathbf{k}}(\mathbf{G})$ ***of the wave functions decrease with increasing*** $|k+G|$***, so that the PW expansion can be effectively truncated at a finite number of terms (limited to all waves with kinetic energy lower than some energy cutoff,*** E_{cut}***):***

(A.88) $\frac{\hbar^2}{2m} |\mathbf{k}+\mathbf{G}|^2 < E_{cut}$

The starting energy cut-off used in VASP is proportional to the square of the highest expansion coefficient based on Rappe, Rabe, Kaxiras and Joannopolous scheme [108,109].

A.2.4 The electron-nuclear interaction

This interaction is given by the bare Coulomb potential. However, a distinction has to be made between electrons that participate directly in chemical bonding (valence) and those that are tightly bound to the nuclei (core), which do not participate in the bonding and can be treated as frozen orbitals. In some cases, there are third classes of electrons called semi-core, which do not participate in

the bonding but are sufficiently close in energy to the valence to feel the presence of the environment. These terms are widely used to denote single-particle electronic states rather than just electrons.

A.2.4.1 Atomic pseudopotentials

The wave functions for free electrons in a periodic crystal can be expanded in PWs. If the potential due to the atoms is neglected, then PWs are the exact solution. If the potential is smooth, then it can be treated as perturbation, leading to the nearly free electron model. The potential originating from the atomic nuclei, however, is far from smooth. ***For heavy atoms, for instance, the wave functions associated with the core states are steeper. The number of PW components required for such steep wave functions are huge. Slater (1937) [106] suggested a possible solution to this problem, where the PW solution is augmented with the solutions of atomic problem in spherical regions around the atoms, and the potential is assumed to be spherically symmetric inside the spheres, and zero outside (APW method). To be discussed deeper later in the hope of building up projected augmented wave (PAW) method, which is used in this study.*** In order to overcome this shape approximation of the potential, Herring (1940) [110] proposed an alternative method consisting of constructing the valence wave functions as a linear combination of PW and core wave functions. By choosing appropriately the coefficients of the expansion, this wave function turns out to be orthogonal to the core states (orthogonalized plane wave method – OPW). Since the troublesome region is taken cared of by the core orbitals, the part that must be represented by the PWs is smooth. When one goes beyond the OPW method and eliminate the core states altogether by replacing it with effective potential or pseudopotential. As inspired by the OPW method, the origin of pseudopotential approach can be traced back to Philips and Kleinman (1959) [111], who showed that one can construct a smooth valence wave function, $\tilde{\varphi}_v$, that is not orthogonalized to the core states $\tilde{\varphi}_c$, by combining the core and the true valence wave functions in the following way:

$$|\tilde{\varphi}_v\rangle = |\varphi_v\rangle + \sum_c \alpha_{cv} |\varphi_c\rangle \quad \text{(A.89)}$$

where $\alpha_{cv} = \langle \varphi_c | \tilde{\varphi}_v \rangle$. This pseudo-wave function satisfies the modified Schrödinger equation:

(A.90) $$\left[\hat{\mathrm{H}}+\sum_{c}(\varepsilon_{\upsilon}-\varepsilon_{c})|\varphi_{c}\rangle\langle\varphi_{c}|\right]|\tilde{\varphi}_{\upsilon}\rangle=\varepsilon_{\upsilon}|\tilde{\varphi}_{\upsilon}\rangle$$

where $\tilde{H}=\tilde{T}+\tilde{V},\tilde{V}=(Z_c/r)\hat{I}$ is the bare nuclear potential and the $\hat{I}$ is the identity operator. This shows that it is possible to construct a pseudo-Hamiltonian:

(A.91) $$\hat{\mathrm{H}}_{PS}=\hat{\mathrm{H}}+\sum_{c}(\varepsilon_{\upsilon}-\varepsilon_{c})|\varphi_{c}\rangle\langle\varphi_{c}|$$

with the same eigenvalues as the original but a smoother, nodeless wave function. The associate potential is:

(A.92) $$\hat{V}_{PS}=\frac{Z_c}{r}\hat{I}+\sum_{c}(\varepsilon_{\upsilon}-\varepsilon_{c})|\varphi_{c}\rangle\langle\varphi_{c}|$$

is the pseudopotential. The most general form is:

(A.93) $$\hat{V}_{PS}(\mathbf{r})=\sum_{l=0}^{\infty}\sum_{m=-l}^{l}\upsilon_{PS}^{l}(r)|lm\rangle\langle lm|=\sum_{l=0}^{\infty}\upsilon_{PS}^{l}(r)\hat{P}_{l}$$

where $\langle\boldsymbol{r}|lm\rangle=Y_{lm}(\theta,\phi)$ are spherical harmonics, and $\upsilon_{PS}^{l}(r)$ is the pseudopotential corresponding to the angular component l, and the operator:

(A.94) $$\hat{P}_{l}=\sum_{m=-l}^{l}|lm\rangle\langle lm|$$

A.2.4.2 Augmented plane waves

Similar to OPW, the augmented basis sets divide the space into muffin-tin (MT) spheres and interstitial regions (we know that spherical approximation can not really cover all regions of target system – in fact, it should be polyhedral but this requires complicated treatment, therefore MT and interstitial regions are conceptualized). A basis set is selected for the interstitial region, and the basis functions are augmented with solutions of the spherically symmetric atomic problem within MT spheres. This separation into spherically-symmetric and non-muffin-tin contributions is very useful, because

the matrix elements involving the spherical components of the potential can be reduced to simple one-dimensional integrals. In augmented PW methods, the calculation of the interstitial potential and density is quite straightforward. The potential in the interstitials, which corresponds to bonding regions, tend to be rather flat [112]. Therefore it makes sense as first suggested by Slater to approximate the non-muffin-tin potential by a constant potential. Moreover the potential reference can be shifted so that this constant is zero, v_{nmt}^{MTA} (muffin-tin approximation – MTA), and in this case the only contribution of the potential to the Hamiltonian matrix elements arises from the integrals within the spheres. A variant of MTA is the atomic sphere approximation (ASA. In the ASA, the spheres are inflated by choosing the MT radius equal to the Wigner-Seitz radius, so that they become space-filling and slightly overlapping (around 10%), thus eliminating the interstitial regions.

In the original APW method the basis functions are plane waves matched to the solutions of the atomic problem inside the MT spheres. An alternative approach is to expand the wave functions of the target system in plane waves, and to augment this directly instead of each individual PW component [113]. The first approach requires a large number of angular momenta, of the order of $l_{\max} \approx 10$ of more, to achieve convergence [114]. The original APW method is based on the MTA (neglecting any non-spherical contributions to the potential). The wave functions are written as linear combinations of the augmented PWs basis functions, and the energies are obtained by solving a generalized eigenvalue equation with non-unity overlap matrix, due to the non-orthogonality of the basis functions for different values of **G**. Since the PWs are orthonormal, when integrating over the entire cell, it is more convenient to calculate the matrix elements by first assuming that the PW part extends to all space, and then discount the contribution from the spheres together with the augmentation part. The overlap matrix is:

$$\left\langle \phi_{\mathbf{G}}^{\mathbf{k}} \middle| \phi_{\mathbf{G}'}^{\mathbf{k}} \right\rangle = \delta_{\mathbf{G},\mathbf{G}'} - \frac{4\pi}{\Omega} \sum_{I=1}^{P} R_{MT}^{I3} e^{i(\mathbf{G}-\mathbf{G}')\cdot\mathbf{R}_I} \frac{j_1\left(\left|\mathbf{G}-\mathbf{G}'\right| R_{MT}^{I}\right)}{\left|\mathbf{G}-\mathbf{G}'\right| R_{MT}^{I}} \tag{A.95}$$

where the first term is the usual orthogonality relation for PW, and the second term is the subtraction of the integrals inside the spheres.

In the LAPW method these logarithmic derivatives (the one that contains the information inside the sphere) are linearized with respect to energy [115,116], thus resulting in the modified basis functions. To take into account the linearization of the atomic basis functions, the only requirement is to modify the (A.95) :

(A.96) $h_{\mathbf{G},\mathbf{G}'}^{l,I,\mathbf{k}} = E_l^I s_{\mathbf{G},\mathbf{G}'}^{l,I,\mathbf{k}} + a_l^{\mathbf{k},I}(\mathbf{G}) b_l^{\mathbf{k},I}(\mathbf{G}')$

where E_l^I is the linearization energy for angular momentum l and atom I. ***Recently, an approach that lies half-way between the LAPW and the pseudo-potential PW methods and is reminiscent of the orthogonalized plane wave (OPW) method has been introduced by Blöchl (1994) [48] under the name projected augmented waves (PAW). This approach retains the all-electron character but it uses a decomposition of the all-electron wave function in terms of a smooth pseudo-wave function, and a rapidly varying contribution localized with the core region (like the muffin-tin spheres in augmentation language). The true and pseudo-wave function are related by a linear transformation:***

(A.97) $\left|\varphi_{AE}^{n}(\mathbf{r})\right\rangle = \left|\varphi_{PS}^{n}\right\rangle + \sum_{I=1}^{P}\sum_{l,m}\sum\left(\left|\varphi_{AE}^{iIlm}(\mathbf{r})\right\rangle - \left|\varphi_{PS}^{iIlm}(\mathbf{r})\right\rangle\right)\left\langle p_i^{Ilm}\middle|\varphi_{PS}^{n}\right\rangle$

Where φ_{AE}^{iIlm} are the all-electron partial waves centered on atom I obtained for a reference atom, and φ_{PS}^{iIlm} are pseudo atomic partial waves that coincide with the all-electron one outside a cutoff radius. The projector functions are used to obey the relation $\langle p_i^{Ilm}|\varphi_{PS}^{n}\rangle$. The sums run over all the atomic sites I, angular momenta (l,m) and projector functions i. For a single projector, it just leads to the OPW method discussed above. The orthogonality relation and the pseudo-atomic partial waves splits the electronic density into three disjoint contributions: a soft pseudo-charge from φ_{PS}^{n}, and two localized charge densities from φ_{AE}^{iIlm} and φ_{PS}^{iIlm}. The expressions involving the pseudized quantities are evaluated in a Cartesian grid using plane waves and the expressions involving localized quantities are evaluated using radial grids. ***Furthermore, the PAW method can freeze the core orbitals to those of***

reference configuration and works only with the valence wave functions (like pseudo-potential). Hence, all the pseudo-potential machinery is available in PAW method, which just has to be supplemented with contributions from the spherical regions. For systems where the charge density distribution closely resembles that of the reference system of the isolated atom within the core region, pseudopotential and PAW will yield almost the same numerical accuracy. However, for systems with large magnetic moments and high electronegativities like those used in this study : iron, cobalt, oxygen and boron atoms, the PAW approach was proved to be more precise [117].

References

[1] A. Eichler, F. Mittendorfer, J. Hafner. Phys. Rev. B 62 (2000) 4744.

[2] J.M. Bradley, X.C. Guo, A. Hopkinson, D.A. King, J. Chem. Phys. 104 (1996) 4283.

[3] E. Janin, H. Schenck, M. Göthelid, U.O. Karlsson. Phys. Rev. B, 61 (2000) 13144.

[4] C. T. Rettner, C. B. Mullins. J. Chem. Phys. 94 (1991)1626.

[5] P.R. Norton, P.E. Binder, and K. Griffiths. J. Vac. Sci. Technol. A 2 (1983) 1028.

[6] N. Freyer, M. Kiskinova, G. Pirug, H.P. Bonzel. Surf. Sci. 166 (1986) 206.

[7]V. Stamenkovic, B. S. Mun, K. Mayhofer, P. Ross, N. Markovic, J. Rossmeisl, J. Greeley, J. K. Nørskov. Angew. Chem. Int. Ed. 45 (2006) 2897.

[8] R. Kitchin, J. K. Nørskov, M. A. Barteau, J. G. Chen. J. Chem Phys. 120 (2004) 21.

[9] J.G. Chen, C.A. Menning, M.B. Zellner. Surf. Sci. Rep. 63 (2008) 201.

[10] A. U. Nilekar, M. Mavrikakis. Surf. Sci. Lett. 602 (2008) L89.

[11] A. Gross. Topics Catalysis 37 (2006) 29.

[12] A. Gross. J. Phys.:Condens. Matter 21 (2009) 084205.

[13] J. Zeng, S. Liao, J. Y. Lee, Z. Liang. Int. J. of Hydrogen Energ. 35 (2010) 942.

[14] M. Wakisaka, H. Suzuki, S. Mitsui, H. Uchida, M. Watanabe. J. Phys. Chem. C 112 (2008) 2750.

[15] Y. Kunisada, M.C. Escaño, H. Kasai. J. Phys.: Condens. Matt. 23 (2011) 394207.

[16] H. Suematsu, Y. Murakami. J. of Magn. Magn. Mater. 90 (1990) 749.

[17] M. Otani, H. Miyagi, N. Suzuki. Physica B 265 (1999) 60.

[18] S. C. Amendola, P. Onnerud, M.T. Kelly, P.J. Petillo, S.L. Sharp-Goldman, M.A. Binder. J. Power Sources 84 (1999)130.

[19] B.F. Minaev, H. Agren. Int. J. Quan. Chem. 57 (1996) 519.

[20] A. L. Buchachenko, V.L. Berdinsky. Chem. Rev. 102 (2002) 603.

[21] Z.P. Li, B.H. Liu, K. Arai, S. Suda. J. Power Sources 126 (2004) 126.

[22] H. Dai, Y. Liang, L. Ma, P. Wang. J. Phys. Chem. C 112 (2008) 15886.

[23] B.H. Liu, S. Suda. J. Alloy Compd., 454 (2008) 280.

[24] E. Gyenge. Electrochim. Acta 49 (2004) 965.

[25] J. Ma, N. A. Choudhury, Y. Sahai Renew. Sust. Energ. Rev. 14 (2010) 183.

[26] S. C. Amendola, S. L.Sharp-Goldman, M. S. Janjua, M. T. Kelly, P. J. Petillo. J. Binder Power Sources 85 (2000)186.
[27] J. S. Zhang, T. S. Fisher, J. P. Gore, D. Hazra, P. V. Ramachandran. Int. J. Hydrogen Energy 31 (2006) 2292.
[28] Y. Kojima, K. Suzuki, K. Fukumoto, M. Sasaki, T. Yamamoto, Y. Kawai, H. Hayashi. Int. J. Hydrogen Energy 27 (2002) 1029.
[29] U. B. Demirci, F. Garin. J. Alloys Compd. 463 (2008) 107.
[30] P. Krishnan, T. H. Yang, W. Y. Lee, C. S. Kim. J. Power Sources 143 (2005) 17.
[31] R. Peña-Alonso, A. Sicurelli, E. Callone, G. Carturan, R. Raj. J. Power Sources 165 (2007) 315.
[32] Ö. Sahin, H. Dolas, M. Özdemir. Int. J. Hydrogen Energy, 32 (2007) 2330.
[33] Ö. Sahin, H. Dolas, M. Kaya, M. S. Izgi, H. Demir. Int. J. Hydrogen Energy, 34 (2010)557.
[34] M.C. Escaño, E. Gyenge, R. Arevalo, H. Kasai. J. Phys. Chem. C, 115 (2011) 19883.
[35] M. Simoes, S. Baranton, C. Coutanceau. J. Phys. Chem. C. 113 (2009) 13369.
[36] V. Kiran, T. Ravikumar, N.T. Kalyanasundaram, S. Khrishnamurty, A.K. Shukla, S. Sampath. J. Electrochem. Soc. 157 (2010) B1201.
[37]H. Dong, R. Feng, X. Ai, Y. Cao, H. Yang, C. Cha. J. Phys. Chem. B. 109 (2005) 10896.
[38] V.W.S. Lam, E.L. Gyenge. J. Electrochem. Soc. 155 (2008) B1155.
[39] M. Finazzi, L. Braicovich. Phys. Rev. B 50 (1994) 14671.
[40] R. Bertacco, F. Ciccacci. Phys. Rev. B 57 (1998) 96.
[41] W. J. Antel, M. M. Schwickert, T. Lin. Phys. Rev. B 60 (1999) 12933.
[42] M. Tsujikawa, A. Hosokawa, T. Oda. Phys. Rev. B 77 (2008) 054413.
[43] G. Schütz, R. Wienke, W. Wilhelm, W.B. Zeper, H. Ebert, K. Spörl. J. Appl. Phys. 67 (1990) 4456.
[44] S.M. Valvidares, T. Schroeder, O. Robach, C. Quiros, T.L. Lee, S. Ferrer. Phys. Rev. B 70 (2004) 224413.
[45] P. Hohenberg, W. Kohn. Phys. Rev. 136 (1964) B864.
[46] M. Levy. Phys. Rev. A 26 (1982) 1200.
[47] W. Kohn, L. Sham. Phys. Rev. 14 (1965) Al133.
[48] P. Blochl. Phys. Rev. B 50 (1994)17953.
[49] G. Kresse, J. Joubert. Phys Rev. B 59 (1999) 1758.

[50] J. P. Perdew. Phys. Rev. Lett. 55 (1985) 1665.
[51] P. Perdew, K. Burke, M. Ernzerhof. Phys. Rev. Lett. 78 (1997) 1396.
[52] M. Methfessel, A. Paxton. Phys. Rev. B 40 (1989) 3616.
[53] M.P. Teter , M.C. Payne, D.C. Allan. Phys. Rev. B 40 (1989) 12255.
[54] G.W.R Leibbrant, R. van Wijk, F.H.P.M. Habraken. Phys. Rev. B 47 (1993) 6630.
[55] C. Kittel.1996. Introduction to Solid State Physics. New York: Wiley.
[56] G.A. Prinz. Phys. Rev. Lett. 54 (1995) 1052.
[57] J. Davies, T.E. Jackman, D.P. Jackson, P.R. Norton. Surf. Sci 109 (1981) 20.
[58] A. Wachter, K.P. Bohnen, K.M. Ho. Ann. Physik 6 (1996) 215.
[59] F. Seitz, H. Ehrenreich, D. Turnbull, F. Spaepen. 1955-1974. Solid states physics: advances in research and applications. Vol. 40. Orlando: Academic Press.
[60] A. Gross. 2002. Theoretical Surface Science: A Microscopic Perspective. USA: Springer.
[61] CRC Handbook of Chemistry and Physics. 86th ed. 2005. CRC Press: Boca Raton, FL.
[62] Q. Ge, P. Hu, D.A. King, M.H. Lee, J.A. White, M.C. Payne. J. Chem. Phys. 106, (1997) 1210.
[63] Y. Xu, M. Mavrikakis. J. Chem. Phys. 166 (2002) 10846.
[64] N. A. Deskins, Jochen Lauterbach, K.T. Thomson. J. Chem. Phys. **122,** (2005) 184709.
[65] D.J. Liu, J. W. Evans. Chem. Phys. Chem. 11 (2010) 2174.
[66] A. Gross, A. Eichler, J. Hafner, M.J. Mehl, D.L. Papaconstantopolous. J. Chem. Phys 124 (2007) 174713.
[67] P.H. Dederichs, S. Blügel, R. Zeller, H. Akai. Phys. Rev. Lett. 53 (1984) 2512.
[68] U. von Barth, L. Hedin. J. Phys. C 5 (1972) 1629.
[69] V.P. Antropov, M.I. Katsnelson, M. van Schilfgaarde, B.N. Harmon. Phys. Rev. Lett. 75 (1995) 729.
[70] V.P. Antropov, M.I. Katsnelson, B.N. Harmon, M. van Schilfgaarde, D. Kusnezov. Phys. Rev. B 54 (1996) 1019.
[71] K. Binder, D. W. Heerman. 2010. Monte Carlo Simulation in Statistical Physics. Berlin: Springer.

[72] J. M. Thijssen. (1999). Computational Physics. Cambridge: Cambridge University Press.
[73] N. Metropolis, A.W. Rosenbluth, M.N. Rosenbluth, A.H. Teller, E. Teller. J. Chem. Phys. 21 (1953) 1087.
[74] M.H. Kalos, P.A. Whitlock. 1986. Monte Carlo Methods. New York: John Wiley.
[75] W. Durr, M. Taborelli, O. Paul, R. Germar, W. Gudat, D. Precia, M. Landolt. Phys. Rev. Lett. 62 (1989) 206.
[76] C. Liu, S.D. Bader. J. Appl. Phys. 67 (1990) 5758.
[77] J.A.C. Bland, C. Daboo, B. Heinrich, Z. Celinski, R.D. Bateson. Phys. Rev. B 51 (1995) 258.
[78] D. I Bardos. J. Appl. Phys. 40 (1969) 1371.
[79] V.W.S. Lam, D.C.W Kannangara, A. Alfantazi, E.L. Gyenge. J. Phys. Chem C 115 (2011) 2727.
[80] P.T. Fort, R. E. Richards. Discuss. Faraday Soc. 19 (1975) 230.
[81] E. Bogh, I. Stensgaard. Physics Lett. 65A (1978) 357.
[82] J.A. Davies, D.P. Jackson, N. Matsunami, P.R. Norton, J.U. Andersen. Surf. Sci. 78 (1978) 274.
[83] S.C. Badescu, P. Salo, T. Ala-Nissila, S.C. Ying, K. Jacobi, Y. Wang, K. Bedurftig, G. Ertl.Phys. Rev. Lett 88 (2002) 136101.
[84] K. Liu, D.W. He, X.L. Zhou, H.H. Chen. Physica B. 406 (2011) 3065.
[85] G. S. Karlberg. Phys. Rev. B 74 (2006) 153414.
[86] V.W.S. Lam, E.L. Gyenge personal communication.
[87] R. J. Gillespie. 1972. Molecular Geometry. London: Van Nostrand Reinhold.
[88] A. D. Becke, K.E. Edgecombe. J. Chem. Phys. 92 (1990) 5397.
[89] G. Rostamikia, M. Janik. J. Electrochem. Soc. 156 (2009) B86.
[90] J.O.M. Bockris, A. K.N. Reddy, M.G. Aldeco. (2000). Modern electrochemistry 2A Fundamentals of electrodics. 2nd ed. New York: Kluwer Academic Publishers.
[91] C.D. Taylor, S. A. Wasileski, J.B. Filhol, M. Neurock. Phys. Rev. B 73 (2006) 165402.
[92] P. Deshlahra, E.E. Wolf, W.F. Schneider. J. Phys. Chem A 113 (2009) 4125.
[93] P. J Feibelman. Phys. Rev. B 12 (2001) 6412.

[94] A.Y. Lozovoi, A. Alavi, J. Kohanoff, R.M. Lynden-Bell. J. Chem. Phys. 115 (2001) 1661.
[95] J. Kohanoff. 2006. Electronic Stucture Calculations for Solids and Molecules. Cambridge: Cambridge University Press.
[96] J. Neugebauer, M. Scheffler. Phys. Rev. B 46 (1992) 16067.
[97] M. Watanabe, D. A. Tryk, M. Wakisaka, H. Yano, H. Uchida. Electrochim Acta DOI:/10.1016/j.electacta.2012.04.035.
[98] M. Born, J. R. Oppenheimer. Ann. d. Physik 84 (1927) 457.
[99] G. Kresse, J. Furthmüller. Comput. Mater. Sci. 6 (1996) 15.
[100] G. Kresse, J. Furthmüller. Phys. Rev. B 54 (1996) 11169.
[101] G. Kresse, J. Hafner. Phys. Rev. B 47 (1993) 558.
[102] G. Kresse, J. Hafner. Phys. Rev. B 49 (1994) 14251.
[103] G. Kresse, M. Marsman, J. Furthmüller (n.d.) Citing Website. VASP. Retrieved April 23, 2012, from www.vasp.at.
[104] U. von Barth, L. Hedin. J. Phys. C 5 (1972) 1629.
[105] P. S. Svendsen, U. von Barth. Phys. Rev. B 54 (1996) 17402.
[106] J. C. Slater. Phys. Rev. 51 (1937) 846.
[107] O.K. Andersen, R. V. Kasowski. Phys. Rev. B (1971) 1064.
[108] A.M. Rappe, M, Rabe, E. Kaxiras, D. Joannopoulos. Phys. Rev. B 41 (1990) 1227.
[109] G. Kresse, J. Hafner. J. Phys. Condens. Matter 6 (1994) 8245.
[110] C. Herring. Phys.Rev. 57 (1940) 1169.
[111] J.C. Phillips, L. Kleinman. Phys. Rev. 116 (1959) 287.
[112] O. Jepsen, J. Madsen, O.K. Andersen. Phys. Rev. B 26 (1982) 2790.
[113] J. M. Soler, A. R. Williams. Phys. Rev. B 42 (1990) 9728.
[114] T. L. Loucks. Phys. Rev. 139 (1965) A81.
[115] O.K. Andersen. Phys. Rev. B 12 (1975) 3060.
[116] O.K.Andersen. Solid State Comm. 13 (1973) 133-136.
[117] G. Kresse, D. Joubert. Phys. Rev. B. 59 (1999) 1758.

Acknowledgments

The accomplishment of the QEDC program would not be realized without the acceptance and financial support of **SATO-YO International Scholarship Foundation (SISF)** for masters and **Japan Society for Promotion of Science (JSPS) Young Scientists Fellowship** for doctor course scholarship and research funds.

Part of the works is supported by the Special Coordination Funds for the **Global Center of Excellence (COE) program (H08)** "Center of Excellence for Atomically Controlled Fabrication Technology. Some of the calculations were done using computer facilities of the Cyber Media Center (Osaka University), the ISSP Super Computer Center (University of Tokyo).

Deep gratitude is extended to the PhD candidate's supervisor, **Prof. Hideaki Kasai** for weekly seminars and support for any financial troubles that the candidate faced.

The doctoral candidate also would like to extend gratitude to **Prof. Hiroshi Nakanishi** for casual discussions, corrections and technical advice; **Prof. Wilson Diño**, for further support on the candidate's conduct of study as a private student.

The staff of Kasai lab, **Ms. Tanaka, Ms. Aihara, Ms. Nojiri, Ms. Furuyama and Yuji**, have been very helpful to the candidate's issues on Japanese language, scholarship interviews and tuition exemption applications, tax payment matters and Sato/JSPS Reports and other never-ending paperworks. The candidate hopes that service is given back to Kasai lab staff in return for such assistance. It is also hoped that the friendship established will continue even after the candidate leaves Japan.

Deepest gratitude is also due to the candidates's mentor in Canada, **Prof. Gyenge,** who has rigorously check manuscripts and give ideas on how to proceed. For the books and journals that he advised the candidate to read and for all the collaborative discussions and experimental experiences the

researcher enjoyed.

To **Prof. Richard Ernst** for his powerful advise during the HOPE meeting: "If you want to combine fields, make sure you know one and explore the other!" that the candidate has kept in mind.

To all the **Kasai Lab Japanese and Foreign students**, then and now, whom the researchers have met and interacted with – many thanks.

To the PhD candidate's friends in Japan who have supported her during "no-scholarship" months, "part-time job" in library and personal trips: **Ms. Tanaka, Yuki, Maria, Hans, Tanglaw, Quang, Ya-juan, Yun-peng, Jen2** – many thanks.

Utmost gratitude is due to **Escaño-Sison-Aquino clan** for researcher's beneficial summer breaks, international calls and all kinds of support possible.

To those who the candidate's failed to mentioned - sorry and thank you.

To the candidate's brain - you are useless sometimes but thanks.

Most of all to the Master from whom all Matter or Energy emanate. Thank you!

List of Publications

1. Mary Clare Sison Escaño, Hiroshi Nakanishi, Hideaki Kasai, First Principles Investigation on Atomic Structure and Stability of Pt_{ML}/Fe(001), Journal of Physics Condensed Matter 19, 482002 (2007).

2. Yoshiyuki Kubota, Mary Clare Sison Escaño, Eben Dy Sy, Hiroshi Nakanishi, Hideaki Kasai, A Study on the Stability of O_2 on Oxometalloporphyrins by the First Principles Calculations, The Journal of Chemical Physics 126, 1 (2007).

3. Yoshiyuki Kubota, Mary Clare Sison Escaño, Hiroshi Nakanishi, Hideaki Kasai, Crystal and Electronic Structure of $Li_{15}Si_4$, The Journal of Applied Physics 102, 053704 (2007).

4. Mary Clare Sison Escaño, Tomoya Kishi, Shinichi Kunikata, Hiroshi Nakanishi, Hideaki Kasai, Pt_{ML}/Fe(001) Alternative Cathode Catalyst: A First Principles Study, Surface and Interface Analysis 40, 1085 (2008).

5. Mary Clare Sison Escaño, Hiroshi Nakanishi and Hideaki Kasai, Bonding at Pt-Fe overlayer and its effects on atomic oxygen chemisorption: a density functional theory study, Surface Science 602, 3415 (2008).

6. Nguyen Tien Quang, Mary Clare Sison Escaño, Nobuaki Shimoji, Hiroshi Nakanishi, Hideaki Kasai, DFT Study on the Adsorption of NO, CO and O_2 on Iron Tape-porphyrin, Physical Review B 77, 19 (2008).

7. Nguyen Tien Quang, Mary Clare Sison Escaño, Nobuaki Shimoji, Hiroshi Nakanishi, Hideaki Kasai, DFT Study on the Adsorption of NO on Iron Tape-porphyrin, Surface and Interface Analysis 40, 1082 (2008).

8. Yoshiyuki Kubota, Mary Clare Sison Escaño, Hiroshi Nakanishi, Hideaki Kasai, Electronic Structure of LiSi, Journal of Alloys and Compounds 458, 151-157 (2008).

9. Mary Clare Sison Escaño and Hideaki Kasai, Spin-polarized density functional theory calculations on adsorption and dissociation of O_2 on Pt/Fe(001), Journal Physical Chemistry 113, 14302 (2009).

10. Mary Clare Sison Escaño, Hiroshi Nakanishi and Hideaki Kasai, The role of ferromagnetic substrate in the reactivity of Pt/Fe overlayer: a density functional theory study, Journal of Physical Society Japan 78, 064603 (2009).

11. Mary Clare Sison Escaño, Hiroshi Nakanishi and Hideaki Kasai, Another way of looking at bonding on bimetallic surfaces: the role of spin-polarization of surface metal d-states, Journal of Physics: Condensed Matter 41, 492201 (2009).

12. Nguyen Tien Quang, Mary Clare Sison Escaño, Rieko Tanaka, Hiroshi Nakanishi, Hideaki Kasai, Adsorption of NO on various metal tape-porphyrins, Journal of Physical Society Japan 78, 014706 (2009).

13. Mary Clare Sison Escaño, Elod Gyenge, Hiroshi Nakanishi and Hideaki Kasai, Pt/Cr and Pt/Ni catalyst for oxygen reduction: To alloy or not to alloy?, Journal of Nanoscience and Nanotechnology 11, 2944 (2011).

14. Mary Clare Sison Escaño, Tien Quang Nguyen and Hideaki Kasai, Molecular and electronic tuning of Si/CNT Hybrid Systems, Japanese Journal of Applied Physics 50, 45101 (2011).

15. Mary Clare Sison Escaño, Nguyen Tien Quang, Hideaki Kasai, Analysis of band gap formation in graphene by Si impurities: local bonding interaction rules, Chemical Physics Letters 515, 85 (2011).

16. Mary Clare Sison Escaño, Elod Gyenge, Ryan Arevalo, Hideaki Kasai.Reactivity descriptors of borohydride interaction on metal surfaces, Journal of Physical Chemistry C 115, 19883 (2011).

17. Yuji Kunisada, Mary Clare Sison Escaño, Hideaki Kasai, Surface magnetism in O_2 dissociation, Journal of Physics: Condensed Matter 23, 394207 (2011).

18. Ferensa Oemry, Mary Clare Sison Escaño, Hirofumi Kishi, Shinichi Kunikata, Hiroshi Nakanishi, Hideaki Kasai, Hiroyoshi Maekawa, Kazuo Osumi, Yoshihisa Tashiro. Nitrogen Monoxide Adsorption on Platinum Tetramer Clusters Coated on Gamma-Alumina (111) Surface, Journal of Nanoscience and Nanotechnology 11, 2844 (2011).

Scientific Meetings:

Outside Japan:

1. Mary Clare Sison Escaño, Hiroshi Nakanishi, Hideaki Kasai. Pt monolayer on Fe substrate as alternative cathode catalyst. Computational Materials Design and 9th De La Salle University-Osaka University Academic Research Workshop and Symposium. De La Salle University, Philippines. August 7-9, 2007.

2. Mary Clare Sison Escaño, Hiroshi Nakanishi, Hideaki Kasai. Alternative PEFC cathode catalyst design by first principles. Computational Materials Design and De La Salle University-Osaka University Workshop. De La Salle University, Philippines. September 1-3, 2008.

3. Mary Clare Sison Escaño, Hiroshi Nakanishi, Hideaki Kasai. "Reactivity of diatomic molecule on bimetallic surface: the case of O_2 adsorption and dissociation on Pt/Fe. AVS 55th International Symposium and Exhibition. Hynes Convention Center, Boston, Massachusetts, USA. October 19-24, 2008.

4. Mary Clare Sison Escaño, Hiroshi Nakanishi, Hideaki Kasai. Tuning Pt surface reactivity using strain and ligand effects in Pt/Cr and Pt/Ni Systems: applications to cathode catalyst design". 11th Science and Technology Congress. De La Salle University, Philippines. September 20-23, 2009.

5. Mary Clare Sison Escaño, Hideaki Kasai. "Enhancing gas bimetallic surface reaction via spin manipulation". 27th European Conference on Surface Science. Martini Plaza, Groningen, Netherlands. August 29-September 5, 2010.

6. Mary Clare Sison Escaño, Hideaki Kasai. "DFT Study of Si/CNT nanostructures for lithium battery potential applications". 15th De LaSalle University-Osaka University Academic Workshop Manila Philippines. September 27-30, 2010.

7. Mary Clare Sison Escaño, Tien Quang Nguyen, Hiroshi Nakanishi and Hideaki Kasai. Spin effects in metal surface reactions: O_2 on ferromagnetic Pt. Japan-Croatia Workshop. Institute of Physics, Zagreb, Croatia. October 4-9, 2011.

8. Mary Clare Sison Escaño, Tien Quang Nguyen, Hiroshi Nakanishi and Hideaki Kasai. Spin effects in metal surface reaction: O_2 on ferromagnetic Pt. AVS 58th International Symposium and Exhibition, Nashville Convention Center, Tennessee USA. October 30-November 4, 2011.

9. Mary Clare Sison Escaño, Elod Gyenge, Ryan Arevalo and Hideaki Kasai. Theoretical and electrochemical approaches to borohydride oxidation. Japan-CanadaWorkshop. University of British Columbia, Biological and Chemical Engineering Department. November 14, 2011.

10. Mary Clare Sison Escaño, Tien Quang Nguyen, Hiroshi Nakanishi and Hideaki Kasai. Controlling oxidation on Pt by spin manipulation. Nanotech 2012. Santa Clara, California, USA. June 18-23, 2012.

Inside Japan

1. Mary Clare Sison Escaño, Hiroshi Nakanishi, Hideaki Kasai.Alternative cathode catalyst design by first principles. International Conference on Quantum Simulators and Design 2008. Miraikan Tokyo, Japan. May 31-June 3, 2008.

2. Mary Clare Sison Escaño, Hiroshi Nakanishi, Hideaki Kasai. First principles investigation on atomic and electronic structure of Pt monolayer on Fe(001). The Physical Society of Japan 63rd Annual Meeting. Kinki University, Osaka, Japan. March 22-26, 2008.

3. Mary Clare Sison Escaño, Tomoya Kishi, Hiroshi Nakanish, Hideaki Kasai. Pt_{ML}/Fe(001) as alternative cathode catalyst: a first principles study. International 21st Century COE Symposium on Atomistic Fabrication Technology 2007. Icho-Kaikan, Osaka University, Japan. October 15-17,

2007.

4. Mary Clare Sison Escaño, Hiroshi Nakanishi, Hideaki Kasai. First principles investigation on the atomic structure and stability of Pt monolayer on Fe(001). 2nd International Workshop on "Materials Science and Nano-Engineering". Awaji Island, Japan. December 1-5, 2007.

5. Mary Clare Sison Escaño. Alternative PEFC cathode catalyst design: current results and future investigations. International Workshop on Surfaces and Interfaces in Applied Solid State Physics/Chemistry and Materials Science: Structures, Physical Properties and Reactivity. P2 Suita Campus, Osaka University. November 9, 2007.

6. Mary Clare Sison Escaño, Tomoya Kishi, Hiroshi Nakanish, Hideaki Kasai. Pt_{ML}/Fe(001) as alternative cathode catalyst: a first principles study. 10^{th} OU-DLSU Academic and Research Workshop. P2 Suita Campus, Osaka University. November 29, 2007.

7. Mary Clare Sison Escaño, Hiroshi Nakanishi, Hideaki Kasai. Alternative PEFC cathode catalyst design by first principles. Quantum Simulation and Design 2008. National Museum of Emerging Science and Innovation (Miraikan), Tokyo, Japan. May 31-June 3, 2008.

8. Mary Clare Sison Escaño, Hiroshi Nakanishi, Hideaki Kasai. Alternative PEFC cathode catalyst design by first principles. OU-ITB Academic Research Workshop. Osaka University, P2 Suita Campus. June 30, 2008.

9. Mary Clare Sison Escaño, Hiroshi Nakanishi, Hideaki Kasai. The role of ligand effects in the modification of reactivity of bimetallic surfaces: Pt monolayer on various substrates. International Symposium on Surface Science and Nanotechnology. International Conference Center Waseda University. November 9-13, 2008.

10. Mary Clare Sison Escaño. Alternative PEFC cathode catalyst design by first principles". Osaka University– De La Salle University Mini-Workshop. P2 Suita Campus, Osaka University. January 30, 2009.

11. Mary Clare Sison Escaño. O_2 dissociative adsorption on Pt overlayers on 3d-transition metal (Fe) based on first principles calculations Osaka University – De La Salle University-University of British Columbia Mini-Workshop, P2 Suita Campus, Osaka University. February 17, 2009.

12. Mary Clare Sison Escaño, Hideaki Kasai "Another way of looking at O_2 reactivity on bimetallic surfaces: the role of spin-polarization of surface metal d-states". Osaka University-University of East Anglia Joint Collaboration Initiative. Science and Engineering Library Multipurpose Room, 2nd Floor, Osaka University, Japan. July 2, 2009.

13. Mary Clare Sison Escaño. Reactivity of O_2 on supported Pt monolayer by first principles calculations. GCOE International Workshop on Quantum Simulations for Atomically Controlled Fabrication Technology. M2 Suita Campus Osaka University, Japan. November 27, 2008.

18. Mary Clare Sison Escaño, Elod Gyenge, Hiroshi Nakanishi and Hideaki Kasai. Tuning Pt surface reactivity using ligand effects and strain on Pt /Cr and Pt/Ni systems: applications to fuel cell cathode catalyst design. Second International Symposium on Atomically Controlled Fabrication Technology. Osaka University Nakanoshima Center, Osaka Japan. November 26, 2009.

19. Mary Clare Sison Escaño, Elod Gyenge, Hiroshi Nakanishi and Hideaki Kasai. Enhancing gas-bimetallic surface reaction via spin manipulation. 3rd International conference on Nanospintronics Design and Realization and International Conference on Core Research and Engineering Science of Advanced Materials. Osaka Japan. June 2, 2010.

20. Mary Clare Sison Escaño, and Hideaki Kasai. The origin of evolution of Si clusters on SWCNT. 13th OU-DLSU Academic Workshop, Osaka Japan. May 28, 2010.

21. Mary Clare Sison Escaño, and Hideaki Kasai. Electronic factors governing reactivity of bimetallic surface to oxygen. 13th International Conference on Theoretical Aspects of Catalysis. Matsushima, Ichinobo Hotel, Japan. June

21-25, 2010.

22. Mary Clare Sison Escaño, and Hideaki Kasai. Enhancing gas-bimetallic surface reaction via spin manipulation. 51th Annual Symposium of Vacuum Society of Japan. Osaka University, Japan. November 4-6, 2010.

23. Mary Clare Sison Escaño, and Hideaki Kasai. Enhancing O_2 activation on metal surfaces by spin manipulation. 3rd International Symposium Atomically Controlled Fabrication Technology. Osaka University, Nakanoshima Center, Osaka, Japan. November 24-26, 2010.

24. Mary Clare Sison Escaño, Elod Gyenge, Ryan Arevalo, Hideaki Kasai. BH_4^- adsorption on Noble Metals. International Workshop on Applied Surface Science/Nanostructures and Fuel Cell Engineering. Suita Campus, Osaka University, Japan. April 27, 2011.

25. Mary Clare Sison Escaño, Elod Gyenge, Ryan Arevalo, Hideaki Kasai. BH_4^- adsorption on noble netals. International NanoScience (INSD) Seminar. Toyonaka Campus, Osaka University, Japan. May 12, 2011.

26. Mary Clare Sison Escano, Tien Quang Nguyen, Hideaki Kasai. Molecular and electronic tuning of Si/Carbon hybrid systems. First JSMS (Japan Society of Mechanical Engineer) Symposium on Multi-scale Materials Modeling. Suita Campus, Osaka University, Japan. May 23-24, 2011.

27. Tien Quang Nguyen, Mary Clare Sison Escaño, Hideaki Kasai. Oxygen dissociation on metal-oxide supported Pt cluster. 4th International Symposium on Atomically Controlled Fabrication Technology, Osaka University Nakanoshima Center, Osaka, Japan. October 31-November 2, 2011.

MONTE CARLO CODE

```
PROGRAM ising3d
    ! ISING MODEL For BIMETALLIC SYSTEMS
    ! A Monte Carlo simulation
    ! Version:
    !       - Calculate energy And magnetization per site For body center cubic
    !       - Calculate specific heat And susceptibility
    !       - Re-Format data In ouput file (Temp, En, Ma, Mb, M)
    !       - Improve interactive information of Log file (status.Log)
    !
    !          04.08.2011: Initial release
    !
    ! Usage:
    !       - The Input parameters are Set In "input.dat"
    !       - The Output data Is written To "ouput.dat"
    !       - Simulation state Is written To "status.log"
    !
    ! Developed
    ! CLARE ESCANO
    ! Dept. of Applied Physics, Osaka University
    ! Contact: clare@dyn.ap.eng.osaka-u.ac.jp
    !
    ! Notice:
    !          For better initializing spin configuration,
    !          please Set nrows, ncols As even numbers.
    !
    !          For GENERAL BIMETALLIC SYSTEMS contact Me
    !          Or make your own
    !
    !

    implicit none

    ! Variable declarations
    Integer,allocatable :: S(:,:,:)          ! spin state of system
    Integer :: i,j,k                         ! some dummy integers
```

```
      Integer :: ii,jj,kk                    ! trial spin indexes
      Integer :: latt                        ! crystal structure (cubic, bcc,...)
      Integer :: nrows,ncols                 ! number of rows And columns
      Integer :: na,nb,nlays                 ! number of layers (bottom/top/All)
      Integer :: initype                     ! initial spin state of system
      Integer :: nsteps,nsweep,istep         ! MC loops: total, sweep, current
      Integer :: trial                       ! value of changed spin
      Integer :: ntemps,itemp                ! number of scans: total, current
      Integer :: counter                     ! update times For energy,
                                             magnetization
      Integer :: mem_check                   ! check If allocation Is alright
      real :: Sa,Sb                          ! atomic spins of Type A And Type B
      real :: Jaa,Jbb,Jab                    ! spin coupling interaction
                                              (AA,BB,AB)
      real :: low_temp,high_temp             ! initial And final temperatures
      real :: inter_temp,temp                ! interval And current temperatures
      real :: beta                           ! inverse of current temperature
      real :: Ma,Mb,Mn                       ! cumulative average magnetization
(A/B/All)
      real :: Ma2,Mb2,Mn2                    ! cumulative average magnetization^2
(A/B/All)
      real :: En,En2                         ! cumulative average energy, energy^2
      real :: dE                             ! change In energy between 2 configs
      real :: prob_trans                     ! transition probability
      real :: Cv,Xa,Xb,X                     ! specific heat And susceptibility
      real :: t_begin,t_end                  ! total CPU Time of the simulation

      Call cpu_time(t_begin)

      ! Writing To Log file
      Open(unit=10,file='status.log',status='replace',action='write')
      Write(10,*) "3D ISING MODEL - BIMETALLIC SURFACE"
      Write(10,*) "A Monte Carlo simulation"
      Write(10,*) "Developed by"
      Write(10,*) "CLARE ESCANO"
      Write(10,*)
```

```
      Write(10,*)
      Write(10,*) "NOTE* For general type of systems contact me"
      Write(10,*) "or better yet make your own     (@__@)  "
      Write(10,*) "-----------------------------------"
      Write(10,*)

      ! Reading Input parameters
      Open(unit=11,file='input.dat',status='old',action='read',err=1)
      GoTo 2
1     Write(10,*) "ERROR: Input file not found"
      Stop
2     Read(11,*) latt
      Read(11,*) Sa,Sb
      Read(11,*) Jaa,Jbb,Jab
      Read(11,*) nrows,ncols,na,nb
      Read(11,*) initype
      Read(11,*) nsteps,nsweep
      Read(11,*) low_temp,high_temp,inter_temp
      Close(11)
      Write(10,*) "Successfully read input file"

      ! Checking Input parameters
      If (latt/=2) Then
         Write(10,*) "ERROR: Structure is not supported.Check input file!"
         Stop
      End If
      If (nrows<=0 .or. ncols<=0 .or. (na+nb)<=0) Then
         Write(10,*) "ERROR: Lattice should be positive"
         Stop
      Else If (na==0 .or. nb==0) Then
         Write(10,*) "NOTICE: Single metallic surface found"
      Else
         Write(10,*) "NOTICE: Bimetallic surface found"
      End If
      If (nsteps<0 .or. nsweep<0) Then
         Write(10,*) "ERROR: Monte Carlo loops negative"
```

```
        Stop
    Else If (nsteps<nsweep) Then
        Write(10,*) "ERROR: Sweeping loops too large"
        Stop
    End If
    If (inter_temp<=0) Then
        Write(10,*) "ERROR: Temperature interval is wrong"
        Stop
    Else If (high_temp<=0 .or. low_temp<=0) Then
        Write(10,*) "ERROR: Temperature should be positive"
        Stop
    Else If (high_temp<low_temp) Then
        Write(10,*) "ERROR: Problem found in temperatures"
        Stop
    End If

    ! Allocating spin matrix
    nlays=na+nb
    allocate(S(nrows+2,ncols+2,nlays),stat=mem_check)
    If (mem_check/=0) Then
        Write(10,*) "ERROR: Not enough memory. Reduce size!"
        Stop
    End If

    ! Opening Output file
    Open(unit=12,file='output.dat',status='replace',action='write')
    Write(12,*) " Temp          En      M_a     M_b   M_tot      C_v      X_a
X_b    X_tot"

    ! Running temperature loops
    ntemps=Int((high_temp-low_temp)/inter_temp)+1
    Temp_loops: Do itemp=1,ntemps
        ! Resetting variables
        counter=0
        Ma=0.0
        Ma2=0.0
```

```
Mb=0.0
Mb2=0.0
Mn=0.0
Mn2=0.0
En=0.0
En2=0.0

! Setting up spin configuration
Call InSpin(S,nrows,ncols,nlays,initype)

! Calculating current temperature
temp=low_temp+inter_temp*(itemp-1)
beta=1.0/temp

! Showing status In Log file
Write(10,*)
Write(10,*) "Perform calculation for T=",temp
Write(10,*) "...running Monte Carlo loops"

! Running Monte Carlo loops
MC_loops: Do istep=1,nsteps
    ! Finding energy & magnetization
    If (istep>nsweep) Then
        counter=counter+1
        Call TotMn(Ma,Ma2,Mb,Mb2,Mn,Mn2,Sa,Sb,nrows,ncols,na,nb,S)
        Call TotEn(En,En2,Jaa,Jbb,Jab,nrows,ncols,na,nb,latt)
    End If

    ! Flipping a spin randomly
    ii=nint((nrows-1)*Random()+2)
    jj=nint((ncols-1)*Random()+2)
    kk=nint((nlays-1)*Random()+1)
    trial=-S(ii,jj,kk)

    ! Calculating energy change
    Call deltaE(dE,ii,jj,kk,trial,S,Jaa,Jbb,Jab,nrows,ncols,na,nb,latt)
```

```
            ! Performing the transition
            prob_trans=Exp(-beta*dE)
            If (Random()<prob_trans) Then
                S(ii,jj,kk)=trial
                If (ii==2) S(nrows+2,jj,kk)=trial
                If (ii==nrows+1) S(1,jj,kk)=trial
                If (jj==2) S(ii,ncols+2,kk)=trial
                If (jj==ncols+1) S(ii,1,kk)=trial
            End If
        End Do MC_loops

        ! Calculating specific heat
        Cv=(beta**2)*(En2/counter-(En/counter)**2)

        ! Calculating susceptibility
        Xa=beta*(Ma2/counter-(Ma/counter)**2)
        Xb=beta*(Mb2/counter-(Mb/counter)**2)
        X=beta*(Mn2/counter-(Mn/counter)**2)

        ! Writing To Output file
        Ma=Abs(Ma)/counter
        Mb=Abs(Mb)/counter
        Mn=Abs(Mn)/counter
        En=En/counter
        Write(12,'(F6.1,F10.4,3F7.3,4E10.2)') temp,En,Ma,Mb,Mn,Cv,Xa,Xb,X
        Write(10,*) "...done"
    End Do Temp_loops

    ! Finishing All calculations
    deallocate(S)
    Close(12)
    Call cpu_time(t_end)
    Write(10,*)
    Write(10,*) "PROGRAM COMPLETED SUCCESSFULLY!"
    Write(10,*) "CPU time used (s): ",t_end-t_begin
```

```
    Close(10)

!-------------------------------------------------------------------------------
CONTAINS
    SUBROUTINE InSpin(S,nrows,ncols,nlays,initype)
        ! Setting up initial spin state
        implicit none
        Integer :: i,j,k
        Integer :: nrows,ncols,nlays,initype
        Integer :: S(:,:,:)
        If (initype==1) Then    ! Uniform Type
            S(:,:,:)=1
        Else If (initype==2) Then    ! Sandwich Type
            Do k=1,nlays
                S(:,:,k)=-(-1)**k
            End Do
        Else If (initype==3) Then    ! Checkerboard Type
            Do k=1,nlays
                Do i=1,nrows+2
                    Do j=1,ncols+2
                        S(i,j,k)=-(-1)**(i+j+k)
                    End Do
                End Do
            End Do
        Else If (initype==4) Then    ! Random Type
            Do k=1,nlays
                Do i=2,nrows+1
                    Do j=2,ncols+1
                        S(i,j,k)=nint(Random())*2-1
                    End Do
                End Do
            End Do
            S(1,1,:)=S(nrows+1,ncols+1,:)
            S(nrows+2,1,:)=S(2,ncols+1,:)
            S(1,ncols+2,:)=S(nrows+1,2,:)
            S(nrows+2,ncols+2,:)=S(2,2,:)
```

```
        S(2:nrows+1,1,:)=S(2:nrows+1,ncols+1,:)
        S(2:nrows+1,ncols+2,:)=S(2:nrows+1,2,:)
        S(1,2:ncols+1,:)=S(nrows+1,2:ncols+1,:)
        S(nrows+2,2:ncols+1,:)=S(2,2:ncols+1,:)
    Else
        Write(10,*) "ERROR: No initial state is chosen"
        Stop
    End If
End SUBROUTINE InSpin

SUBROUTINE TotMn(Ma,Ma2,Mb,Mb2,Mn,Mn2,Sa,Sb,nrows,ncols,na,nb,S)
    ! Calculating magnetization
    implicit none
    Integer :: nrows,ncols,na,nb,nlays
    Integer :: S(:,:,:)
    real :: Sa,Sb
    real :: Ma_sum,Mb_sum
    real :: Ma_tmp,Mb_tmp,M_tmp
    real :: Ma,Mb,Mn
    real :: Ma2,Mb2,Mn2
    nlays=na+nb
    Ma_sum=sum(Sa*S(2:nrows+1,2:ncols+1,1:na))
    Mb_sum=sum(Sb*S(2:nrows+1,2:ncols+1,na+1:nlays))
    If (na==0) Then
        Ma_tmp=0.0
        Mb_tmp=Mb_sum/(1.0*nrows*ncols*nb)
    Else If (nb==0) Then
        Ma_tmp=Ma_sum/(1.0*nrows*ncols*na)
        Mb_tmp=0.0
    Else
        Ma_tmp=Ma_sum/(1.0*nrows*ncols*na)
        Mb_tmp=Mb_sum/(1.0*nrows*ncols*nb)
    End If
    M_tmp=(Ma_sum+Mb_sum)/(1.0*nrows*ncols*nlays)
    Ma=Ma+Ma_tmp
    Ma2=Ma2+Ma_tmp**2
```

```
        Mb=Mb+Mb_tmp
        Mb2=Mb2+Mb_tmp**2
        Mn=Mn+M_tmp
        Mn2=Mn2+M_tmp**2
    End SUBROUTINE TotMn

    SUBROUTINE TotEn(En,En2,Jaa,Jbb,Jab,nrows,ncols,na,nb,lt)
        ! Calculating total energy
        implicit none
        Integer :: i,j,k,lt
        Integer :: nrows,ncols,na,nb,nlays
        real :: Jaa,Jbb,Jab
        real :: E_tmp,En,En2
        E_tmp=0.0
        nlays=na+nb
        Do i=2,nrows+1
            Do j=2,ncols+1
                If (nb==0) Then
                    If (nlays==1) Then
                        E_tmp=E_tmp+E1(Jaa,i,j,nlays,lt)
                    Else
                        Do k=1,nlays-1
                            E_tmp=E_tmp+E1(Jaa,i,j,k,lt)+E2(Jaa,i,j,k,lt)
                        End Do
                        E_tmp=E_tmp+E1(Jaa,i,j,nlays,lt)
                    End If
                Else If (na==0) Then
                    If (nlays==1) Then
                        E_tmp=E_tmp+E1(Jbb,i,j,nlays,lt)
                    Else
                        Do k=1,nlays-1
                            E_tmp=E_tmp+E1(Jbb,i,j,k,lt)+E2(Jbb,i,j,k,lt)
                        End Do
                        E_tmp=E_tmp+E1(Jbb,i,j,nlays,lt)
                    End If
                Else
```

```
                    If (na==1 .and. nb==1) Then
                        E_tmp=E_tmp+E1(Jaa,i,j,1,lt)+E1(Jbb,i,j,2,lt)+E2(Jab,i,j,1,lt)
                    Else If (na==1 .and. nb>1) Then
                        Do k=2,nlays-1
                            E_tmp=E_tmp+E1(Jbb,i,j,k,lt)+E2(Jbb,i,j,k,lt)
                        End Do

E_tmp=E_tmp+E1(Jaa,i,j,1,lt)+E1(Jbb,i,j,nlays,lt)+E2(Jab,i,j,1,lt)
                    Else If (na>1 .and. nb==1) Then
                        Do k=1,na-1
                            E_tmp=E_tmp+E1(Jaa,i,j,k,lt)+E2(Jaa,i,j,k,lt)
                        End Do

E_tmp=E_tmp+E1(Jaa,i,j,na,lt)+E1(Jbb,i,j,nlays,lt)+E2(Jab,i,j,na,lt)
                    Else
                        Do k=1,na-1
                            E_tmp=E_tmp+E1(Jaa,i,j,k,lt)+E2(Jaa,i,j,k,lt)
                        End Do
                        E_tmp=E_tmp+E1(Jaa,i,j,na,lt)+E2(Jab,i,j,na,lt)
                        Do k=na+1,nlays-1
                            E_tmp=E_tmp+E1(Jbb,i,j,k,lt)+E2(Jbb,i,j,k,lt)
                        End Do
                        E_tmp=E_tmp+E1(Jbb,i,j,nlays,lt)
                    End If
                End If
            End Do
        End Do
        E_tmp=E_tmp/(2.0*nrows*ncols*nlays)
        En=En+E_tmp
        En2=En2+E_tmp**2
    End SUBROUTINE TotEn

    SUBROUTINE deltaE(dE,ii,jj,kk,trial,S,Jaa,Jbb,Jab,nrows,ncols,na,nb,lt)
        ! Calculating energy change
        implicit none
        Integer :: ii,jj,kk,trial
```

```
Integer :: nrows,ncols,na,nb,nlays,lt
Integer :: sum0,sum1,sum2,sum3,sum4
Integer :: S(:,:,:)
real :: dE,dE1,dE2
real :: Jaa,Jbb,Jab
nlays=na+nb
If (lt==1) Then
    sum0=S(ii-1,jj,kk)+S(ii+1,jj,kk)+S(ii,jj+1,kk)+S(ii,jj-1,kk)
    sum1=S(ii,jj,kk+1)
    sum2=S(ii,jj,kk-1)
    sum3=S(ii,jj,kk+1)
    sum4=S(ii,jj,kk-1)
Else
    sum0=0
    sum1=S(ii-1,jj-1,kk+1)+S(ii,jj-1,kk+1)+S(ii-1,jj,kk+1)+S(ii,jj,kk+1)
    sum2=S(ii-1,jj-1,kk-1)+S(ii,jj-1,kk-1)+S(ii-1,jj,kk-1)+S(ii,jj,kk-1)
    sum3=S(ii,jj,kk+1)+S(ii+1,jj,kk+1)+S(ii,jj+1,kk+1)+S(ii+1,jj+1,kk+1)
    sum4=S(ii,jj,kk-1)+S(ii+1,jj,kk-1)+S(ii,jj+1,kk-1)+S(ii+1,jj+1,kk-1)
End If
! Energy change within a layer
If (kk>=1 .and. kk<=na) Then
    dE1=-2*Jaa*trial*sum0
Else
    dE1=-2*Jbb*trial*sum0
End If
! Energy change between layers
If (nlays==1) Then
    dE2=0.0
Else If (nb==0 .and. na>1) Then
    If (kk==1) Then
        dE2=-2*Jaa*trial*sum1
    Else If (kk==nlays) Then
        If (Mod(kk,2)==0) dE2=-2*Jaa*trial*sum4
        If (Mod(kk,2)/=0) dE2=-2*Jaa*trial*sum2
    Else
        If (Mod(kk,2)==0) dE2=-2*Jaa*trial*(sum4+sum3)
```

```
            If (Mod(kk,2)/=0) dE2=-2*Jaa*trial*(sum2+sum1)
        End If
    Else If (na==0 .and. nb>1) Then
        If (kk==1) Then
            dE2=-2*Jbb*trial*sum1
        Else If (kk==nlays) Then
            If (Mod(kk,2)==0) dE2=-2*Jbb*trial*sum4
            If (Mod(kk,2)/=0) dE2=-2*Jbb*trial*sum2
        Else
            If (Mod(kk,2)==0) dE2=-2*Jbb*trial*(sum4+sum3)
            If (Mod(kk,2)/=0) dE2=-2*Jbb*trial*(sum2+sum1)
        End If
    Else If (na==1 .and. nb==1) Then
        If (kk==1) Then
            dE2=-2*Jab*trial*sum1
        Else
            dE2=-2*Jab*trial*sum4
        End If
    Else If (na==1 .and. nb>1) Then
        If (kk==1) Then
            dE2=-2*Jab*trial*sum1
        Else If (kk==2) Then
            dE2=-2*Jab*trial*sum4-2*Jbb*trial*sum3
        Else If (kk==nlays) Then
            If (Mod(kk,2)==0) dE2=-2*Jbb*trial*sum4
            If (Mod(kk,2)/=0) dE2=-2*Jbb*trial*sum2
        Else
            If (Mod(kk,2)==0) dE2=-2*Jbb*trial*(sum4+sum3)
            If (Mod(kk,2)/=0) dE2=-2*Jbb*trial*(sum2+sum1)
        End If
    Else If (na>1 .and. nb==1) Then
        If (kk==1) Then
            dE2=-2*Jaa*trial*sum1
        Else If (kk==na) Then
            If (Mod(kk,2)==0) dE2=-2*Jaa*trial*sum4-2*Jab*trial*sum3
            If (Mod(kk,2)/=0) dE2=-2*Jaa*trial*sum2-2*Jab*trial*sum1
```

```
        Else If (kk==nlays) Then
            If (Mod(kk,2)==0) dE2=-2*Jab*trial*sum4
            If (Mod(kk,2)/=0) dE2=-2*Jab*trial*sum2
        Else
            If (Mod(kk,2)==0) dE2=-2*Jaa*trial*(sum4+sum3)
            If (Mod(kk,2)/=0) dE2=-2*Jaa*trial*(sum2+sum1)
        End If
    Else
        If (kk==1) Then
            dE2=-2*Jaa*trial*sum1
        Else If (kk>1 .and. kk<na) Then
            If (Mod(kk,2)==0) dE2=-2*Jaa*trial*(sum4+sum3)
            If (Mod(kk,2)/=0) dE2=-2*Jaa*trial*(sum2+sum1)
        Else If (kk==na) Then
            If (Mod(kk,2)==0) dE2=-2*Jaa*trial*sum4-2*Jab*trial*sum3
            If (Mod(kk,2)/=0) dE2=-2*Jaa*trial*sum2-2*Jab*trial*sum1
        Else If (kk==na+1) Then
            If (Mod(kk,2)==0) dE2=-2*Jab*trial*sum4-2*Jbb*trial*sum3
            If (Mod(kk,2)/=0) dE2=-2*Jab*trial*sum2-2*Jbb*trial*sum1
        Else If (kk>na+1 .and. kk<nlays) Then
            If (Mod(kk,2)==0) dE2=-2*Jbb*trial*(sum4+sum3)
            If (Mod(kk,2)/=0) dE2=-2*Jbb*trial*(sum2+sum1)
        Else
            If (Mod(kk,2)==0) dE2=-2*Jbb*trial*sum4
            If (Mod(kk,2)/=0) dE2=-2*Jbb*trial*sum2
        End If
    End If
    ! Energy change In total
    dE=dE1+dE2
End SUBROUTINE deltaE
Function E1(JJ,i,j,k,lt)
    ! Coupling energy within a layer
    ! Double counting Is included
    implicit none
    Integer :: i,j,k,lt
    real :: JJ,E1
```

```
        If (lt==1) Then
            E1=-JJ*S(i,j,k)*(S(i-1,j,k)+S(i+1,j,k)+S(i,j-1,k)+S(i,j+1,k))
        Else
            E1=0.0
        End If
    End Function E1
    Function E2(JJ,i,j,k,lt)
        ! Coupling energy between two layers
        ! Double counting Is included
        implicit none
        Integer :: i,j,k,lt
        real :: JJ,E2
        If (lt==1) Then
            E2=-2*JJ*S(i,j,k)*S(i,j,k+1)
        Else
            If (Mod(k,2)==0) Then
E2=-2*JJ*S(i,j,k)*(S(i,j,k+1)+S(i+1,j,k+1)+S(i,j+1,k+1)+S(i+1,j+1,k+1))
            Else
E2=-2*JJ*S(i,j,k)*(S(i-1,j-1,k+1)+S(i,j-1,k+1)+S(i-1,j,k+1)+S(i,j,k+1))
            End If
        End If
    End Function E2
        Function Random()
        ! Generating a uniform Random number
        ! based On the internal generator In F90
        implicit none
        real :: Random,x(1)
        Call random_number(x(1:1))
        Random = x(1)
    End Function Random
End PROGRAM ising3d
```